A STUDY OF NON-COOL CORE GALAXY CLUSTERS AND THE FEEDBACK FROM THEIR CENTRAL ACTIVE GALACTIC NUCLEI

by

Ayşegül Tümer

B.S., Physics, Boğaziçi University, 2008

M.S., Biomedical Engineering Boğaziçi University, 2014

Submitted to the Institute for Graduate Studies in
Science and Engineering in partial fulfillment of
the requirements for the degree of
Doctor of Philosophy

Graduate Program in Physics

Boğaziçi University

2019

To my country and all Turkish PhD students; may they all reach beyond their dreams. Bizarre difficulties will always be there, but we will always be equipped to face the hardest of battles as long as we do not give up on our goals.

ACKNOWLEDGEMENTS

"It is not down in any map; true places never are." – Herman Melville, *Moby-Dick, or, the Whale*

The journey was tough, but so was I... Here are the people who had my back through it.

My thesis supervisor, Prof. E. Nihal Ercan, who welcomed me to her High Energy Astrophysics Laboratory with open arms, and provided all needed support on everything imaginable. You have worked all of your life to make our laboratory stand tall, giving it all you have got amidst all difficulties, and I hope that I have made you proud. Thank you for believing in me through all of these years, and never giving up on me.

Prof. Metin Arık, whose office door I knocked about 16 years ago when I first enrolled to the university. You listened to me talk about my strange take on the Universe with great interest, ignited my curiosity every time we met by giving me insights that cannot be found in any book. It was an honor to be valued by you. You have spent immense amount of time on my preparation for the PhD qualifier exam, and made sure you had given me every support I needed to achieve my dreams.

My friend and colleague Dr. François Mernier, who has been there to support my endeavors from day one, and most importantly gave me amazing ideas that helped shape my thesis. I cannot wait for our life-long collaboration and friendship.

Dr. Francesco Tombesi, who made it his personal mission that I graduate form PhD with a great publication. You have introduced me to world-class scientists and built this strong collaboration. It has been difficult at times, but you have always been patient and positive. I wish you all the great success in your work.

Dr. Herve Bourdin, who shared his code and spent months teaching me. I deeply appreciate those efforts.

Dr. Roberto Serafinelli, who introduced me to Dr. Francesco Tombesi and opened up a whole new horizon in my career. You are both a colleague and a good friend. Dr. Massimo Gaspari, who has given me motivation and great feedback for our work through our collaboration.

My thesis jury, Prof. M. Naci İnci, Prof. M. Levent Kurnaz, Prof. Yüksel Karataş, and Prof. K. Yavuz Ekşi, who made my thesis defense day a positive and highly motivational day.

Dr. Burçin Ünlü, who convinced me to go back to physics when my spirit was broken, and provided the means for it. Without this, I may have never found the courage to.

Asst. Prof. Daniel R. Wik, my soon-to-be boss and more importantly my mentor, who saw a light in me, a light I have not seen in myself yet, and trusted me with his valuable project. With this amazing support, my motivation got through the roof during the last months of finishing the thesis.

Mehtap Tınaz, our lovely department secretary, who handled the paperwork of all those years like a boss so that we could focus solely on our studies. You went beyond your duties and always provided moral support. Can Güven, who has helped me immensely through the publication process of this thesis.

My friends; Yunus E. Gökdağ, Dr. Emine Ertuğrul, Dr. Furkan S. Dündar, Bengü Aktaş, Öznur Demir, Sinancan Kara, who were always patient while I kept complaining about complications during these strange years.

My curiosity team; Önder Dünya and Arda İnanç, with whom I spent uncountable hours discussing physics over cups of coffee and tea. Those were the precious moments,

which I will always cherish and maybe the best part of becoming a physicist.

My 4-legged friends and kids, Uğur, Tütsü, Füme, Küba, Ömür, JLo, Ginger, Fermat, and late Tesla among many unnamed. I hope you know how much piece of mind you have brought me. Life would be black and white without you. You are nature's most precious gifts.

My Zus, Tuba Özerol Cebeci. You will always have that special place in my heart, which you have not broken for once. You were always there for me through decades; you are the special gift of life to me, next to my family.

My family; Harun, Emine, Ferhat and Ferruh Tümer. I wish I could to share the beautiful thank you paragraph I had previously written in my native language for you to read.

Myself; from the day you knew yourself up to this day, you have shown unbelievable strength, patience, and resilience. Seriously, I cannot believe it, I do not know how you did it. You knew what you wanted even as a kid, and just went for it. Nothing could stand in your way. You have given everything you have got, and then some. Every chapter was filled brand new challenges. You are a maniac. Now that you've got your great white whale, take a breath and evaluate. Only once piece of advice for the future; make sure you know when to use your patience and when to refrain from using it. And now, the sky is the limit.

I would like to thank Boğaziçi University Research Fund Grant Number 13760 for financial support. The research leading to these results has received funding from the European Union's Horizon 2020 Programme under the AHEAD project (grant agreement n. 654215). I acknowledge support by the Study in Italy Grant, Research Under Academic Supervision.

ABSTRACT

A STUDY OF NON-COOL CORE GALAXY CLUSTERS AND THE FEEDBACK FROM THEIR CENTRAL ACTIVE GALACTIC NUCLEI

The study of the brightest cluster galaxy (BCG) coronae of non-cool core (NCC) galaxy clusters and their central active galactic nuclei (AGN) is crucial for the understanding of the BCG's role on galaxy cluster evolution as well as the activation of the cooling and heating mechanism in the central regions of galaxy clusters. In this thesis, the X-ray properties of the intracluster medium (ICM) of a sample of NCC galaxy clusters and their BCG interstellar medium (ISM), along with their central AGN is investigated using archival *XMM-Newton* observations. For this purpose, a joint spectroscopic and imaging method is proposed and applied to the sample. It is found that, AGN plays an important role on the ICM structure and the heating of the central regions of the clusters, although at smaller spatial scales compared to that of cool core clusters. In addition, BCG coronae seem to preserve their structural integrity and are isothermal, despite the disturbed morphology and merger history of the cluster. Furthermore, a chemically rich BCG tail structure is discovered that extends up to 40 kpc even though they are assumed to be rare in galaxy populations.

ÖZET

AĞIR SOĞUYAN MERKEZLİ GALAKSİ KÜMELERİ VE MERKEZİ ETKİN GALAKSİ ÇEKİRDEĞİN GERİBİLDİRİMİ

Ağır soğuyan merkezli galaksi kümelerinin, en parlak küme galaksi koronaları ve merkezi etkin galaktik çekirdeklerinin araştırılması, en parlak küme galaksilerinin küme evriminde oynadığı rolü ve merkezi soğuma-ısıtma mekanizmalarının aktivasyonunu anlamak için büyük önem taşımaktadır. Bu tezde arşiv *XMM-Newton* gözlemleriyle, bir grup ağır soğuyan merkezli galaksi kümelerin küme içi ortamlarının X-ışın özellikleri, en parlak küme galaksilerinin yıldızlararası ortamı, ve bunun yanısıra merkezi etkin galaktik çekirdeklerinin araştırılması hedeflenmiştir. Bu amaçla, birleşik bir tayfsal ve görüntüleme metodu sunulmuş ve küme grubuna uygulanmıştır. Hızlı soğuyan merkezli galaksi kümelerine göre daha kısa mesafede etkili olan ağır soğuyan merkezli galaksi kümelerinin merkezi etkin galaktik çekirdeklerinin, küme içi ortamının yapısında ve merkezdeki ısıtma mekanizması üzerinde önemli bir rol oynadığı bulunmuştur. Buna ek olarak bahsi geçen koronaların, ev sahibi galaksi kümelerinin yapısından ve birleşme tarihinden bağımsız olarak yapısal bütünlüklerini korudukları bulunmuştur. Aynı zamanda literatürde nadir bulunan yapılar olarak tanımlanan, 40 kpc mesafeye kadar yayılmış bir en parlak küme galaksi kuyruğu keşfedilmiştir.

TABLE OF CONTENTS

LIST OF FIGURES

LIST OF TABLES

LIST OF SYMBOLS

D_A	Angular diameter distance
f_X	X-ray flux
L_X	X-ray luminosity
m_e	Electron mass
m_p	Proton mass
$M_\odot$	Solar mass
n_e	Electron density
n_H	Hydrogen density
N_H	Hydrogen column density
P	Pressure
r_{cool}	Cooling radius
t_{cool}	Cooling time
z	Redshift
$Z_\odot$	Solar abundance
β	Slope of the surface brightness profile model
$\epsilon(\nu)$	Emissivity of the bremsstrahlung continuum
Γ	Photon index of the power-law emission
Σ_X	X-ray surface brightness

LIST OF ACRONYMS/ABBREVIATIONS

AGN	Active Galactic Nuclei
APEC	Astrophysical Plasma Emission Code
BCG	Brightest Cluster Galaxy
BH	Black Hole
CALDB	Calibration Database
CC	Cool Core
CCD	Charge Coupled Device
CCF	Current Calibration Files
CF	Cooling Flow
CCT	Central Cooling Time
CXB	Cosmic X-ray Background
EM	Emission Measure
GTE	Galactic Thermal Emission
HEASOFT	High Energy Astrophysics Software
HIFLUGCS	Highest X-ray Flux Galaxy Cluster Sample
HP	Hard Particle
ICM	Intracluster Medium
ISM	Interstellar Medium
LHB	Local Hot Bubble
NCC	Non-cool Core
PSF	Point Spread Function
SCC	Strong Cool Core
SMBH	Supermassive Black Hole
SP	Soft Proton
WCC	Weak Cool Core
XSPEC	An X-Ray Spectral Fitting Package

1. INTRODUCTION

Galaxy clusters are the largest gravitationally bound systems in the present universe. They can be defined as dark matter (DM) halos as a first approach, which follows the shape of the DM potential [1–3]. The deep gravitational potential well of galaxy clusters makes these massive objects ideal to study the astrophysical phenomena which has occurred in the cluster history, as well as to study cosmology. Since they are bound systems in general, the physical processes taking place inside the cluster leave their trace, again inside the cluster. The study of galaxy clusters is of great interest in astrophysics, primarily since the intracluster medium (ICM) is a thermal plasma in equilibrium with the highest temperatures which can be studied in detail. The largest gravitational lensing effects in the universe are also detected in clusters due to the large gravitational potential they possess [4]. The Sunyaev-Zeldovich effect can also be investigated at largest scales which is due to the ICM shadowing the cosmic microwave background and resulting in inverse-compton scattering [5]. In addition, galaxy cluster mergers release the highest amount of energies ($\sim 10^{63}$ erg) secondary to the big bang.

The optically thin hot plasma, ICM, accounts for the $\sim$12% of the baryonic matter inside galaxy clusters, where $\sim$3% is attributed to galaxies and stars and the remaining $\sim$85% is dark matter. Relativistic particles with velocities close to the speed of light are also a component of clusters and they emit diffuse synchrotron radiation [6]. However, the mass of these particles are negligible compared to the total ICM mass, yet their influence is significant for the investigation of material mixing inside the clusters. Galaxies are gravitationally bound to the galaxy clusters and the richness of a cluster is characterized by the number of galaxies within a specific radius [7]. Dark matter is the unknown matter component which was introduced to explain why the velocity dispersions of galaxies in a cluster are higher than the expected value from only ICM and galaxy mass [8].

Prior to X-ray observatories, optical observations of galaxy clusters suggested that the space in between the galaxies inside the cluster was matter free. First detection of X-ray emission in clusters was from the central region of Virgo cluster, namely from the region around the galaxy M87 [9, 10]. X-ray satellite *Uhuru* observations [11] indicated that clusters of galaxies are in general spatially extended X-ray sources. The mechanism behind the obtained X-ray spectra was in agreement with thermal Bremsstrahlung from hot gas which required that the space between the galaxies in a cluster was filled with hot ($\sim 10^7 - 10^8$ K) and dilute ($\sim 10^{-5}$ - 10^{-1} atoms/cm^3) plasma. While a density of $\sim 10^{-5}$ atoms/cm^3 correspond to the approximate value in the cluster outskirts, $\sim 10^{-1}$ atoms/cm^3 correspond to the densest regions in clusters. This thermal interpretation was then confirmed by the detection of of iron K (Fe-K) shell line emission from the nearby Virgo, Perseus and Coma clusters by *Ariel V* and *OSO-8* X-ray satellites [12, 13]. An Fe enrichment of 0.3-0.5 Solar was found from the spectral analysis of a sample of galaxy cluster ICM, through observations from *OSO-8* and *HEAO-1 A2* [14, 15]. Since the only known source of significant iron abundance then was nuclear reaction from stars, and extragalactic star population was not observed, it was suggested that a significant amount of this gas must originate from stellar injections from the galaxies [16], although the total mass of star in clusters were in the same order of magnitude with the mass of this intracluster gas. Following the launch of *ASCA* in 1993, different elements namely; O, Ne, Mg, Si, S, Ar, Ca, Fe and Ni were also detected form the ICM bringing on the discussion of the chemical enrichment processes involving supernovae hence the nucleosynthesis in galaxy clusters. These findings showed that the ICM also keeps the record of the chemical enrichment history of the cluster, revealing the integral yield of all stars which release their metals into the ICM through stellar winds and supernova explosions [17].

In relaxed clusters, the ICM shows spherical symmetry and is nearly in hydrostatic equilibrium. Due to the low density of the ICM plasma, all emitted photons within the plasma can leave the ICM which makes the spectra of clusters extremely informative [17]. Main processes leading to the photon emission result in a composed continuum and line emission in the cluster spectrum. The X-ray photon emission processes contributing to the continuum are in the form of; (i) thermal Bremsstrahlung by free-free emission of accelerated electrons in the electrostatic field of ions, (ii) recombination radiation by free-bound emission from an electron capture of an ion, and (iii) slow two-photon radiation with a distribution function resulting from 2s to 1s state radiative transition. Although the latter, (iii) bound-bound emission, is forbidden in laboratory plasmas since the deexcitation occurs more rapidly due to electron collisions, all forbidden transitions are allowed in ICM plasma since it has low density and the ions have sufficient time for the deexcitation prior to another collision. The line emission from the plasma is due to the deexcitation radiation by bound-bound emission resulting from the quantum level transition of an electron bound to an ion [17]. For a thermal plasma, the collision rates depend on the temperature and governed by the electron and ion density. Assuming thermal equilibrium, the shape of the X-ray spectrum of clusters therefore reflects the abundances of elements as well as the plasma temperature. While line emission is more prominent in clusters with lower average temperatures, in higher temperature clusters, line emissions are mostly shadowed by the thermal Bremsstrahlung since at high temperatures the plasma is almost fully ionized. In addition to these processes, a non-thermal emission from inverse Compton (IC) process also occur inside the ICM. The IC is due to the scattering of cosmic microwave background (CMB) with the hot ICM, which is called the Sunyaev-Zeldovich effect, and with relativistic particles. The expected spectra from an ICM plasma at different temperatures and with solar abundance ($Z_\odot$) are represented in Figure 1.1 [17].

The radiation emitted from the galaxy clusters are partially absorbed by the heavy elements of interstellar medium (ISM) of our galaxy, Milky Way. This absorption is corrected using the heavy element column densities and their cross sections which is a function of the photon energy. A good approximation is to use the hydrogen column density (N_H) to trace the heavy elements along the line of sight using radio HI observations from surveys such as the LAB survey [18].

X-ray emission of the ICM is a form of energy loss resulting in the cooling of the plasma. The X-ray emission, hence the cooling, is proportional to the square of particle number density in the medium [19]. This implies that in regions where the density is high, the cooling occurs faster leading to short cooling times. In the early X-ray observations of galaxy clusters, several studies have shown that the cooling times in the dense central regions of the galaxy clusters were much shorter than the Hubble time

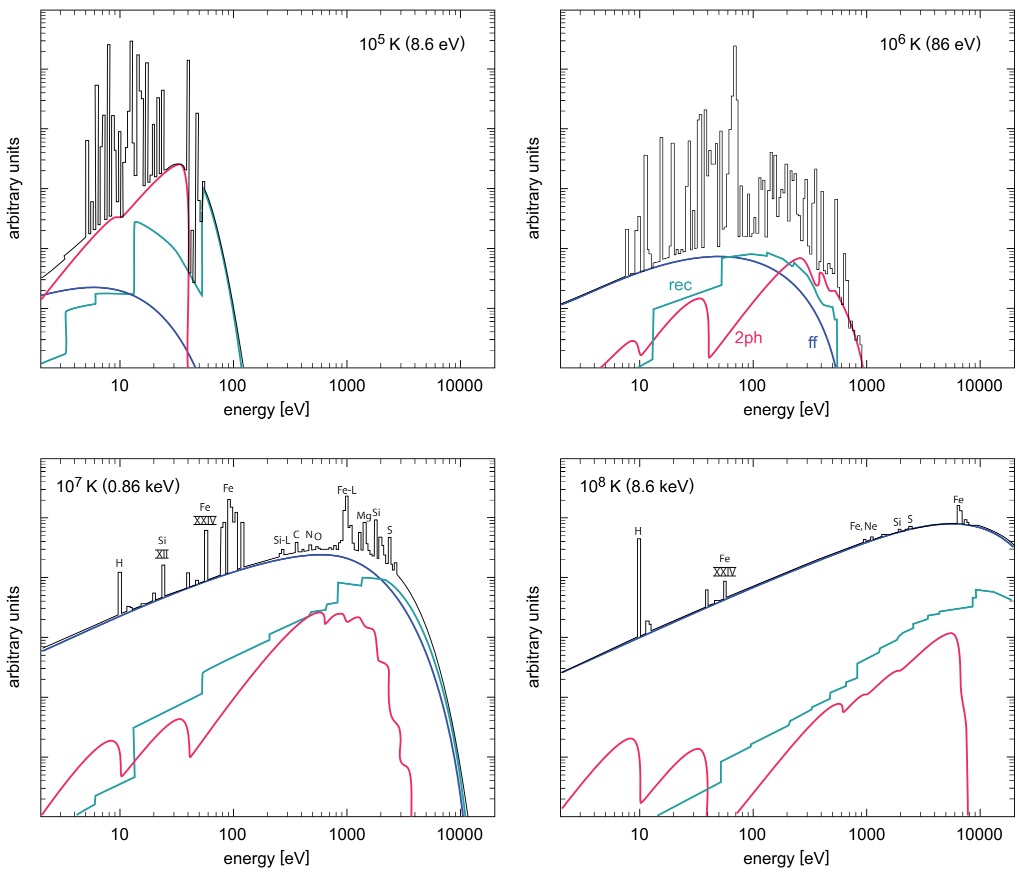

Figure 1.1. X-ray spectra for solar abundance at different plasma temperatures [17]. Bremsstrahlung (blue), recombination radiation (green), and two-photon radiation (red). The lower panel indicates the major line emissions from elements where label L stands for the transition to the L-shell of ions and roman numerals refer to the ions from which they originate.

(shorter than the age of the clusters), meaning that without a mechanism to hinder this cooling, the galaxy clusters would have cooled down completely and ultimately would no longer emit radiation in the X-ray band [20, 21]. As the plasma cools, the pressure of the central regions decrease and causes a flow of matter from the surrounding high pressure ICM.

Following these findings, a cooling flow (CF) model was developed, which predicts a steady gas inflow to the cluster center to maintain the hydrostatic equilibrium in the central regions of the cluster [22]. This model suggested that following a merger event, the clusters would reach a relaxed state, then eventually the central gas condensates and cools, leading to star formation. Although this scenario showed promise with the observations of surface brightness peak at the core of the clusters and central temperature drops, it was later understood with observations from latest generation high resolution *XMM-Newton* RGS observations of CF clusters, that the effect of such cooling flows would be much smaller than anticipated. Firstly, the spectra simply did not show the amount of cool gas anticipated by the CF model [23–29]. In addition, the amount of expected star formation and CO predicted by CF model were also much above of what was observed [30]. Furthermore, it was also shown that the central temperature values of CF clusters were also underestimated by this scenario, and these temperatures rarely dropped below 40% the ambient temperature [31]. When CF model was abandoned, the search for a new heating mechanism to keep the central gas in hydrostatic equilibrium began. This also resulted in the change of nomenclature where the CF clusters has become to be designated as cool core (CC) clusters [32].

Following the change of nomenclature, several studies attempted to distinguish CC clusters form non-cool core (NCC) clusters based on different parameters. Where some studies used central temperature drop parameter to define a CC cluster [33, 34], there were other studies relating the type to a short central cooling time (CCT) [35,36] or significant mass deposition rate [37].

Reiprich and Bohringer (2002) [38] sampled 64 galaxy clusters with a minimum flux of 2 $\times 10^{-11}$ erg s^{-1} cm^{-2} in the 0.1-2.4 keV energy band, using the data of *ROSAT*

All-Sky Survey, namely HIghest X-ray FLUx Galaxy Cluster Sample (HIFLUGCS), where they studied the gravitational masses using ICM gas density profiles of these clusters. Using this sample, Hudson *et al.* (2010) [31] studied the cool core properties of clusters.

As discussed by Hudson *et al.* (2010) [31], this complete sample of clusters are best grouped with a trimodality depending on their (CCT) where central corresponds to 0.4% R_{500}. Based on this trimodality, sample clusters are categorized by their central cooling time as strong cool core (SCC, $t_{cool} < 1.0$ Gyr), weak cool core (WCC, $1.0 < t_{cool} < 7.7$ Gyr) and NCC (7.7 Gyr $< t_{cool}$) clusters [31]. SCC type makes up of the 44% of the clusters in this sample, where WCC comprises the 28% and the remaining 28% belong to the NCC type. All of the CC types of clusters, that is; SCC and WCC combined, host an AGN in their BCGs, whereas only 45% of NCC clusters in this sample show the presence of a central AGN [39]. Cool core clusters show a radial temperature distribution with a low central temperature which rises gradually away from the center, then shows a gradual decrease towards the outskirts [31]. NCC clusters, on the other hand, show a rather flat temperature distribution without a notable decrease in their central temperature [32].

This CC/NCC bimodality is also shown by Cavagnolo *et al.* (2009) [40]. Poole *et al.* (2008) [41] argue, based on their merger simulations studies, that the CC structure is not completely destroyed by a merger activity, in addition CC/NCC is determined once and for all during the cluster formation [42]. Also, cool core remnants in a galaxy cluster which have gone through a merger was found by Rossetti and Molendi (2010) [43], yet some studies such as Pratt *et al.* (2010) [44] argue against this idea. Also, Sun (2009) [45] argue that most of the NCC or WCC systems behave like a mini-cooling core or CC clusters yet in a smaller scale, as in the case of NCC clusters from the HIFLUGCS sample [45]. In fact, these studies argue that these are unambiguous cases, meaning with deeper and high resolution observations of the clusters core would reveal that instead of CC/NCC bimodality, clusters would present a classification with a large cool core (LCC) class with their gas content of ICM origin, and a corona class confined by ISM with a typical radius of $r < 4$ kpc. This picture shows that the distinction between CC and NCC cluster seems to be more complex and is not yet well understood.

Several heating mechanisms were proposed to explain the short cooling time in the central regions of the clusters. Supernovae feedback was seen as a good candidate, however it was later on understood that it would provide an insufficient heating mechanism to overcome the energy loss except for shallow gravitational potential, low-luminosity galaxies [46]. Another proposed scenario was thermal conduction in which heat flows from the outskirts of the clusters inwards, yet afterwards found to be effective only in regions with temperature kT $\geqslant$ 5 keV, and the central rapid cooling regions of clusters mainly unaffected by this mechanism [47]. Recently, the most favored heating mechanism to balance the energy loses due to cooling in the central regions of the clusters is a self-regulated active galactic nuclei (AGN) mechanism [48–50].

AGN is the accretion of matter from the cool collapsed ISM and ICM, onto the supermassive black hole (SMBH) with $M \sim 10^7\ M_\odot$ at the center of galaxies, and their high luminosity as well as multi wavelength emission features distinguish them from regular galactic nuclei [51]. The AGN feedback operates through the partial transfer of the accretion power back to the ISM and ICM, which is believed to be mainly by means of mechanical dissipation [39, 52, 53]. The AGN can be detected in X-rays evidenced by a continuum X-ray emission as a first order a power-law, within 1 keV to over 100 keV [54]. This power-law emission is either characterized by an α parameter designated to the spectral slope, or by a Γ parameter ($\Gamma = \alpha + 1$), which is called the photon index. These photon indices have the range of $\Gamma \sim 1.5 - 2.5$ for different samples of AGN [55–57].

The scale of a SMBH is quite small compared to its host galaxy, therefore this process is expected to work on about a thousand millionfold scales [52]. Recent studies propose that this feedback may affect the ICM at a range of $r < 0.2\ \mathrm{R}_{500}$ [53]. On the other hand, the growth of SMBHs would not be possible without the matter feeding them, which creates a feeding and feedback loop between the central AGN and the ISM/ICM [58]. These findings introduce a co-evolution framework for the SMBH, ISM and ICM through multi-scale and multiphase outflows [59, 60].

Although the exact mechanism of the AGN feedback is still unclear, two main modes are recognized which are based on the BH energy outflow process [52]. One of these modes are called the radiative/quasar/wind mode taking effect at the time when the accreting BH is close to the Eddington limit, and mainly injecting the cold material outwards. Kinetic/radio jet/maintenance mode, operating when the galaxy hosts a hot halo and through powerful jets. Evidence of the mechanical feedback rely on numerous galaxy cluster observations where regions of low density and X-ray emission deficiency are detected, which are defined as cavities [39]. These cavities are most likely the regions where expanding radio lobes push away the ICM constituents and heat transfer occurs by means of sound or weak shock waves [61–63]. The central AGN and ICM interaction through large-scale shocks and ICM bubbles is also established by various studies [62, 64–66].

Brightest cluster galaxies (BCGs) are the most massive galaxies residing at the bottom of the gravitational potential well of the clusters of galaxies and most likely to have the most substantial influence on the surrounding ICM [45]. They are extremely bright objects due to the feeding from the accretion of matter around the central SMBH [67]. In addition, their host clusters are responsible for the evolution of BCGs [68, 69]. Higher fraction of radio-loud AGNs are found in BCGs with respect to other cluster member galaxies holding comparable black hole (BH) and stellar mass [70, 71].

Merger of galaxy clusters have the time scale of 2 - 5 Gyr, and in the hierarchical scenario of cluster formation proposed that clusters grow in size following the merger of smaller units [72–74]. Cool clumps in the central regions of cluster are associated with a post merger structure as evidenced by high quality data from *XMM-Newton* and *Chandra*, which are possibly caused by ram pressure stripping [75]. Disturbed systems are associated with a merger stage and several criteria are proposed for the identification of a cluster as a relaxed or disturbed system. An X-ray peak and BCG position offset cut-off at $r = 0.01$ R_{500} is suggested as a segregation tool between relaxed and disturbed systems [76]. In addition, 2D mapping of the thermodynamical properties of clusters also contribute to these proposed criteria [76].

In this thesis, a combined spectroscopic and imaging method is proposed and applied to a sample of HIFLUGCS NCC clusters to investigate their X-ray features in detail, as well as the role their central AGN plays on the cluster identity. This work is structured as follows; In Chapter 2, the theoretical background related to the implementation of the analysis adopted in this work is presented. In Chapter 3, the cluster sample description and related observables from the literature are given. The *XMM-Newton* data analysis techniques are described in Chapter 4. The *XMM-Newton* results of the implication of the methods on individual clusters are provided and discussed in Chapter 5. A separate chapter, Chapter 6, is reserved for a detailed analysis of MKW 08 using both *XMM-Newton* and *Chandra* data. In Chapter 7, the conclusion is presented.

2. THEORETICAL BACKGROUND

In this chapter, the calculation of the radiation spectrum of ICM in thermal equilibrium and related observables are described. The chemical composition as well as the ionization structure of the plasma are required for the modeling of ICM X-ray spectrum. Assuming a plasma in thermal equilibrium, where the ions are in thermal ionization equilibrium and electrons are in thermal Maxwellian equilibrium, the ionization and recombination rates must be balanced for each ionization step of a specific element [17]:

$$\begin{aligned}&[I^{n+}]n_e\,(C_{ci}+C_{ai}) \;+\; [I^{n+}]\left([H^+]X_{ce1}+[He^+,He^{++}]\;X_{ce2}\right)\\&=[I^{(n+1)+}]n_e\,(C_{rr}+C_{dr}) \;+\; [I^{(n+1)+}]\,([H]X_{ce3}+[He]\;X_{ce4})\end{aligned}\tag{2.1}$$

where ionization parameters are;

- C_{ci}; the direct electron impact ionization,
- C_{ai}; the electron impact excitation into an auto-ionization state with subsequent auto-ionization,
- H^+; the ionizing charge exchange with rate X_{ce1}, and
- He^+; and He^{++}, the ionizing charge exchange with rate X_{ce2}.

and recombination parameters are;

- C_{rr}; the radiative recombination,
- C_{dr}; the dielectronic recombination,
- H; the electron capture charge exchange with the rate X_{ce3}, and
- He; the electron capture charge exchange with the rate X_{ce4}.

A complete set of linear equations are calculated for significant ions and element to obtain the ionization structure [77–79].

These collision rates result in the radiation emission and can be described in the form:

$$R = n_e n_I C_{Ix} = n_e^2 \left[\frac{n_I}{n_E}\right] \left[\frac{n_E}{n_H}\right] \left[\frac{n_H}{n_e}\right] C_{Ix}(T) \tag{2.2}$$

where ionization parameters are;

- n_E are the number densities of the elements,
- n_I are the number densities of the ions,
- n_H are the number density of the Hydrogen nuclei, and
- C_{Ix} are the relevant collision rate coefficients for ion I.

Therefore;

- $[n_I/n_E]$ is the fractional abundance of ionization stage I,
- $[n_E/n_H]$ is the relative elemental abundance, and
- $[n_H/n_e]$ is the Hydrogen nuclei to electron ratio.

This description indicates that all collision rates are proportional to the squared plasma density, n_e^2, and the emission measure (EM) describes the spectrum normalization, i.e.;

$$EM = \int n_e^2 \; dV \tag{2.3}$$

However, most plasma codes defining the plasma use the definition of the EM as;

$$EM = \int n_e n_H dV \tag{2.4}$$

The temperature information of the plasma is provided by the shape of the Bremsstrahlung dominated continuum spectrum. The distribution of spectral energy for this spectrum is described as [80];

$$\epsilon(\nu) = \frac{16\ e^6}{3\ m_e\ c^2} \left(\frac{2\pi}{3m_e\ k_B T_X} \right)^{1/2} n_e n_i\ Z^2\ g_{ff}(Z, T_X, \nu)\ \exp\left(\frac{-h\nu}{k_B T_X} \right) \tag{2.5}$$

where;

- m_e is the electron mass,
- n_e is the electron density,
- n_i is the respective ion density,
- Z is the effective charge of the ion, and
- g_{ff} is the gaunt factor.

The gaunt factor is calculated numerically using a quantum-mechanical treatment and is close to unity. The exponential term, $-h\nu/k_BT$, leads to a sharp spectrum cut-off, T_X, at high energies, and the temperature can be measured with confidence once the energy window of the telescope is able to detect this cut-off. The intensity of the spectral lines reflect the abundances of elements.

The average cooling time for the gas can be calculated via [31],

$$t_{cool} = \frac{3}{2} \frac{(n_e + n_i)kT}{n_e n_H \Lambda(T, Z)} \tag{2.6}$$

where Λ is the cooling function and it is obtained by the emission integration and weighing this emission by the energy of the photons as [19];

$$\Lambda(T, Z) = \int_0^\infty E \frac{d\alpha}{dE}(E, T, Z) dE \tag{2.7}$$

The matter density distribution in the universe goes through a gravitational collapse in the overdense regions which gives rise to the galaxy cluster formation, followed by a configuration of equilibrium described by the virial relation;

$$E_{kinetic} = -2E_{potential} \quad \propto \quad \frac{GM}{R} \tag{2.8}$$

The potential energy of the ICM is converted to internal heat in this collapse activity. In this relation, M is the total mass of galaxy clusters, which also accounts for the dark matter. When the ICM is thermalized, a virial temperature is reached, which exhibits cluster's gravitational potential well depth. As suggested by gravitational collapse simulations [1, 2], this potential has a self-similar shape for galaxy clusters with different mass which leads to the cluster mass and ICM temperature relation;

$$T \propto \sigma_{DM}^2 \propto M/R \quad \propto \quad M^{2/3} \tag{2.9}$$

where σ_{DM} is described as the dark matter particle velocity dispersion. In this relation, $M^{2/3}$ part assumes $M \propto R^3$ and a constant dark matter density, ρ_{DM}. For the comparison of this self-similarity relation at various cluster masses, a radial scale is used based on the critical density of the background universe, ρ_c(z), at the cluster redshift. For the study of cluster with *XMM-Newton*, a typical scale of R_{500} is used. R_Δ corresponds to the radius of a point on a sphere whose density equals Δ times the critical density of the background universe, ρ_c(z), at the cluster redshift where Δ is the density contrast.

Thermal structure as well as thermal history of the ICM can also be characterized by the temperature distribution which is generally described by the structure of the entropy of the ICM. The astrophysical definition of entropy can be given as;

$$S = \frac{k_B T_X}{n_e^{2/3}} \tag{2.10}$$

This definition of entropy, S, is a parameter that labels adiabates, and stays fixed thus S stays fixed in during the ICM hydrodynamic evolution of since all processes in this evolution are adiabatic. The processes such as dissipation of turbulence or shock waves increase the entropy, where radiative cooling results in the decrease of this parameter. The entropy structure bears significant information on the two types of heating inside the ICM, namely; gravitational and non-gravitational processes. Gravitational heating processes refer to potential energy and heat conversion governed by dark matter, whereas non-gravitational processes include heating from galactic winds driven by by star formation and AGN jets.

Using assumptions of a isotropic radiation and energy conservation, the basic observables for cluster emission namely, *luminosity, flux* and *surface brightness* can be described. The power of the photon energy, E, is the luminosity, L_X, which is at the typical value of 10^{44} erg s^{-1} in the X-ray energy band 0.5-2.0 keV;

$$L_X = \frac{dE}{dt} \tag{2.11}$$

Luminosity per surface A, is defined as the flux, f_X;

$$f_X = \frac{dE}{dAdt} \tag{2.12}$$

Given the definition of the flux, the spectral parameters of the power-law emission from an AGN can also be described here as a power-law fit of the flux at a spesific energy [55];

$$f_X(E) = AE^{-\Gamma} \exp(-\sigma_{ph} N_H) \tag{2.13}$$

where, Γ is the spectral photon index and σ_{ph} is the cross section of the photoelectric absorption. The normalization A is given in keV^{-1} cm^{-2} s^{-1} and the hydrogen column density, N_H, is described in Chapter 1.

Following the measurement of the solid angle of the source, Ω, surface brightness, Σ_X is defined;

$$\Sigma_X = \frac{dE}{dA dt d\Omega} \tag{2.14}$$

which is proportional to the square of gas density. In most cases, instead of energy, the photon count in a given energy range is used.

Emissivity (Equation 2.5) and luminosity (Equation 2.11) are related through the following relation using volume V;

$$\epsilon = \frac{dL_X}{dV} \tag{2.15}$$

3. SAMPLE DESCRIPTION AND OBSERVATIONS

In order to study the non-cool core clusters and their central regions in detail, HIFLUGCS clusters that are identified as NCC, due to their central cooling time at 0.4% R_{500}, are selected for this work [31]. NCC clusters contain relaxed systems as well as disturbed systems where major merger events are observed. Some of the NCC clusters in this sample are not suitable for this work, since the main aim of this study is to investigate the azimuthally averaged profiles of clusters along with their BCGs. This requires a cluster morphology that is close to spherical symmetry as well as a clear X-ray emission peak that can be identified with the cluster BCG. The selection criteria for the clusters in this work comprises of NCC-CC segregation parameters from several works. These parameters are listed in Table 3.1. Although some clusters seem not suitable for this study, they are included in the sample since they show interesting features that may aid the understanding of the BCG of NCC cluster.

First criteria is to include the clusters which have a BCG corona. Amongst our sample, the BCG of Abell 1656, Abell 3391 and MKW 08 are identified as a corona [45,81]. Another criteria is the X-ray emission peak and the BCG position offset, which is used to distinguish relaxed systems from disturbed ones, which is referred to as BCG offset criteria in this work. Clusters with BCG offset of < 0.01 R_{500} are included in this sample as they are identified as relaxed clusters in literature using this criteria [82]. In addition, the clusters which are categorized as relaxed systems based on their two dimensional X-ray maps are also included [76].

The exclusion basis of some clusters from the NCC HIFLUGCS sample, and the inclusion of others which do not meet the aforementioned criteria are explained as follows. Since the deprojection methods require the assumption of a spherical symmetry, NCC clusters going under a major merger event have been excluded from the sample, namely; Abell 754, Abell 2163, Abell 3376. Abell 1367 and Abell 1736 have X-ray peak - BCG offset of ~ 500 kpc, hence are not included in this work. Abell 119, Abell 2255, Abell 2256 have no evident X-ray peak, therefore are excluded from the sample. Although Abell 1656 has a large BCG offset [82], it is reported to have a BCG corona [81], therefore it is investigated in this study. ZwCl 1215 meets the BCG offset criteria [82], yet it is categorized as a disturbed system [76]. This cluster is included due to this interesting contraversy. Abell 399, Abell 400, Abell 401, Abell 3158 are included since they are not studied in respect to BCG offset and 2D maps. Abell 3391 is included since it is found that the BCG is a corona [81] although it shows a disturbed morphology [76]. Abell 3395 has two elliptical subclusters therefore azimuthally averaged clusters profiles can not be achieved. It is however included in our sample in order to provide surface brightness and temperature maps to the literature. MKW 08 is included since it meets all criteria. These criteria as well as the cluster properties are summarized in Table 3.1.

In this sample, MKW 08 is also studied with *Chandra* given its deep exposure time and the fact that it is the only cluster that meets all criteria. The detailed study of this cluster is presented separately in Chapter 6.

In this work, archival *XMM-Newton* EPIC observations are used to investigate the azimuthally averaged thermodynamical profiles of the sample of the clusters, as well as the spectral analysis of the central regions. The specifications of the data are summarized in Table 3.2.

Table 3.1. Description of the sample of galaxy clusters used in this work.

Cluster Name	**Equatorial Coordinates**[a] (RA DEC)		**z**[b]	**N**$_H$ [c] (10^{20} cm^{-2})	**Scale**[d] (kpc/arcsec)	**R**$_{500}$ [e] (Mpc)	**CCT**[f] (Gyr)	**Offset** [g] (kpc)	**2D Map**[h]
Abell 399	02h 57m 49.8s	$+13°2'57''$	0.0722	10.6	1.375	1.1169	$12.13^{+1.44}_{-1.22}$	N/A	N/A
Abell 400	02h 57m 38.9s	$+6°0'22''$	0.0238	8.15	0.480	0.6505	$8.04^{+1.99}_{-1.47}$	N/A	N/A
Abell 401	02h 58m 57.5s	$+13°34'46''$	0.0739	9.95	1.405	1.2421	$8.81^{+1.41}_{-1.08}$	N/A	N/A
Abell 1656	12h 59m 43.1s	$+27°56'19''$	0.0231	0.84	0.466	1.1378	$15.97^{+4.52}_{-2.95}$	75.2	RELAXED
Abell 3158	03h 42m 53.9s	$-53°38'7''$	0.0590	1.38	1.141	1.0667	$8.22^{+0.54}_{-0.47}$	N/A	N/A
Abell 3391	06h 26m 22.8s	$-53°41'44''$	0.0514	5.58	1.003	0.8978	$12.46^{+2.49}_{-1.89}$	3.2	DISTURBED
Abell 3395	06h 27m 14.4s	$-54°28'12''$	0.0506	6.70	0.989	0.9298	$12.66^{+3.04}_{-2.18}$	11.6	DISTURBED
ZwCl 1215	12h 17m 41.6s	$+3°39'45''$	0.0766	1.74	1.451	1.0548	$10.99^{+2.09}_{-1.61}$	2.1	DISTURBED
MKW 08	14h 40m 38.2s	$+3°28'35''$	0.0263	2.45	0.529	0.6316	$10.87^{+2.59}_{-1.87}$	3.8	RELAXED

[a] Cluster X-ray peak coordinates [83]

[b] Cluster redshift [83]

[c] The mean atomic hydrogen column density values retrieved from the calculator tool that is based on the methods of Willingale *et al.* (2013) [84] and the data of The Leiden/Argentine/Bon (LAB) Survey of Galactic HI [85].

[d] Spatial and angular ratio, i.e.; 1 arcsec corresponds to the given scale value in kpc [83]

[e] The radius whose density equals 500 times the critical density of the background universe, ρ_c(z), at the cluster redshift [83].

[f] Central cooling time at 0.4% R$_{500}$ [31]

[g] X-ray peak and BCG position offset [82]

[h] Cluster morphology as seen from 2D maps [76]

Table 3.2. *XMM-Newton* EPIC observation log and effective exposure times of the cluster sample data.

Cluster Name	**Observation ID**	**Equatorial Coordinates** (RA DEC)		**Exposure** (ks)
Abell 399	0112260101	02h 57m 52.99s	$+13°1'60.0''$	24.7
Abell 400	0300210501	02h 57m 39.65s	$+0.6°1'1.2''$	17.0
	0404010101	02h 57m 41.59s	$+0.6°1'28.8''$	73.4
Abell 401	0112260301	02h 58m 58.00s	$+13°34'0.0''$	33.3
Abell 1656	0300530701	12h 59m 36.92s	$+27°58'14.8''$	63.7
Abell 3158	0300210201	0.3h 42m 54.77s	$-53°37'48.3''$	53.3
	0300211301	0.3h 42m 54.77s	$-53°37'48.3''$	21.5
Abell 3391	0505210401	0.6h 26m 22.18s	$-53°41'37.3''$	66.2
	0720252301	0.6h 26m 22.7s	$-53°41'43.8''$	33.9
Abell 3395	0400010301	0.6h 27m 11.35s	$-54°27'58.8''$	75.1
ZwCl 1215	0300211401	12h 17m 41.28s	$+0.3°39'37.4''$	57.3
MKW 08	0300210701	14h 40m 38.1s	$+0.3°28'18.1''$	82.7

4. DATA ANALYSIS

In this chapter, the treatment of the archival *XMM-Newton* data of the cluster sample is explained. Firstly, a preliminary cleaning is realized to eliminate the signals unrelated to the source, to obtain proper cluster ICM emission. Subsequently, X-ray surface brightness and temperature maps are constructed. Afterwards, consecutive annular regions are selected to deduce azimuthally averaged radial surface brightness and temperature profiles. Once these profiles are obtained, they are fit using analytical functions to acquire three dimensional, deprojected profiles. In necessary cases, an additional spectral analysis is applied. Throughout this thesis, the ΛCDM cosmology with $H_0 = 70$ km s^{-1} Mpc^{-1}, $\Omega_0 = 0.3$, $\Omega_\Lambda = 0.7$ is assumed.

4.1. The *XMM-Newton* Observatory

XMM-Newton space observatory is launched on December 10, 1999 as a project of European Space Agency (ESA) Horizon 2000 program. The craft is composed of two modules which are connected by a long carbon fibre tube forming the telescope optical bench. Two Reflection Grating Spectrometers (RGS), two European Photo Imaging Cameras (EPIC), namely; Metal Oxide Semi-conductor (MOS) imaging detectors (MOS1 and MOS2), and an EPIC PN readout cameras are located on the Focal Plane Assembly. An Optical Monitor (OM) instrument, star trackers and the three X-ray Mirror Modules are contained in the spacecraft's Service Module.

In this thesis, for the analysis of the X-ray emission from the ICM, EPIC data is used. The field of view of the telescope (FOV) is 30 arcmin, and EPIC cameras provide sensitive imaging in the energy range 0.15 −15 keV, and a spectral resolution of E / Δ E ∼ 20-50, where the angular resolution, i.e.; point spread function (PSF) has FWHM of 6 arcsec [86].

4.2. Data Reduction

As a first step in the data reduction process, the soft proton flares are eliminated from photo detection events using a temporal wavelet filtering of the soft (1-5 keV) and hard (10-12 keV) light curves. Three dimensional position-energy cubes which match the angular and spectral resolution of each EPIC detector are then created by rebinning these composite event-lists. A background noise and an effective exposure value are assigned to each element of these data cubes.

Spectral and spatial dependencies of the mirror effective areas, detector quantum efficiencies and filter absorptions are taken into account in effective exposure values and are combined with bad pixels and CCD gaps positions as detailed in Bourdin and Mazzotta (2008) [87]. The current calibration files and calibration data bases, namely the CCF and the CALDB (v. 4.3.3), are used for the pre-processing of the event lists in order to extract these components. Point sources identification is achieved by a wavelet analysis. These point sources are subtracted for extended emission analysis except for the BCGs, which are also a point of interest in this study.

Astrophysical X-ray background components, namely Galactic Thermal Emission (GTE), Local Hot Bubble (LHB) and Cosmic X-ray Background (CXB), are modeled using the following approach. Two absorbed thermal components $kT_1 = 0.099$ keV and $kT_2 = 0.248$ keV [88] for the GTE, an unabsorbed thermal component $kT = 0.1$ keV [88] for LHB, and an absorbed power-law with photon spectral index $\Gamma = 1.42$ [89] for CXB are used. These models are then jointly fit along with the ICM emission from an annular region with $12' \leqslant r \leqslant 14'$, where GTE and LHB normalizations are freed to vary and CXB normalization is fixed at the blank-sky estimates [90].

Non astrophysical X-ray background can be divided into two components, Soft Proton (SP) Background and Quiescent Particle Background (QPB) [88]. SP is modeled as a broken power-law in case of a soft flare excess after the preliminary data cleaning. QPB, which is due to physical particles interacting with the detectors, is treated analytically following the method of Bourdin *et al.* (2013) [91]. The fluorescent lines produced by the QPB are modeled as Gaussians using the Filter Wheel Closed (FWC) observations, which have different responses from *XMM-Newton* EPIC, namely MOS1, MOS2 and PN cameras. On the other hand, the continuum emission caused by the QPB has a flat response across the detectors. For the quiescent continuum model, a product of power-law and an inverted error function increasing in the soft band is used. For the fluorescent line energies, the values reported by Leccardi and Molendi (2008) [92] are retrieved. The fluorescent lines are subsequently added to the continuum after they are convolved with the detector energy responses. The joint-fit of background and cluster emissions of clusters are shown in the appendix chapter of this work.

4.3. ICM Surface Brightness and Temperature Maps

In order to extract the surface brightness map of the cluster sample in the 0.3 - 2.5 keV energy band, photon images, which are corrected for the effective area and background, are used. For the denoising of the images, the Multi-Scale Variance Stabilized Wavelet Transform (MSVST, [93]) of the count rate and background images are applied. Subsequently, thresholds for the count rate coefficients are set as a function of a tabulated confidence level. By subtracting background coefficients to the non-zero coefficients of the count rate maps, the denoised ICM surface brightness maps are reconstructed.

The projected ICM temperature maps are obtained by using the wavelet spectral imaging algorithm introduced in Bourdin and Mazzotta (2008) [87]. The algorithm extracts spectroscopic temperature values inside overlapping meta-pixels of various sizes along with the confidence intervals. These values are propagated towards a B2-spline wavelet transform and delimited at the specific confidence level as a function of the coefficient variance. In order to estimate local temperatures, a spectroscopic likelihood maximization is used with the assumption that the ICM emission follows the Astrophysical Plasma Emission Code (APEC, [94]). In the individual cluster sections, Chapter 5, two maps for both temperature and surface brightness are presented, where one of each are aimed to show the overall cluster structure and the other two maps are the enlarged figures of the primary images which emphasize the central regions of the cluster. Temperature and surface brightness maps are obtained in soft energy band 0.3-2.5 keV within 4σ errors, unless otherwise stated.

4.4. ICM Surface Brightness and Temperature Profiles

The ICM surface brightness and temperature profiles are extracted from a circular region for each cluster in the energy band of 0.5 - 2.5 keV whose specifications are explained in detail in the individual chapters reserved for each cluster. Surface brightness profiles are extracted with logarithmic binning of the data in concentric annuli. For the temperature profile, a specific number of bins are selected depending on the quality of the data, which are then fit by a single temperature `apec` model absorbed by a galactic hydrogen column density, N_H. Assuming spherical symmetry and hydrostatic equilibrium, an analytical double β-model (Eqn. 4.1) described in Vikhlinin *et al.* (2006) [95] is applied for the deprojection of gas density distributions.

$$[n_e n_p](r) = n_0^2 \frac{(r/r_c)^{-\alpha}}{(1+r^2/r_c^2)^{3\beta-\alpha/2}} \frac{1}{(1+r^\gamma/r_s^\gamma)^{\varepsilon/\gamma}} + \frac{n_{02}^2}{(1+r^2/r_{c2}^2)^{3\beta_2}} \tag{4.1}$$

where,

n_e	electron density
n_p	proton density
n_0	central number density of the ICM component
n_{02}	central number density of the corona component
r	radius (independent variable)
r_c	core radius of the ICM distribution
r_{c2}	core radius of the corona distribution
α	central power-law cusp index
γ	width of the transition region
ε	slope change near the radius r_s
β	slope of the electron density profile

This parametric model, adds two terms for cluster emission and the gas emission from the central region of the cluster. In case there is no prominent, distinct emission from the central region a cluster at hand, the secondary β-model normalization, namely n_{02}, is set to zero. Furthermore, this double β-model incooperates an α parameter to define the power-law characteristics of the gas density in the centers of clusters, which may deviate from a flat core [96]. By using the proton (n_p) and electron (n_e) densities obtained from the fit and integrating the ICM density along the line of sight in the energy band between 0.5 - 2.5 keV, the projected surface brightness profiles, $\Sigma_x(r$, are obtained. In the surface brightness profile figures, background is shown with *black* curves, point spread function modeling is shown in *yellow* and *blue* curves correspond to surface brightness of the cluster The total β-model fit of the projected functions of temperature and brightness are shown with *dotted black* curves.

The double β-model comprises the description of both the central region emission and the ICM as well as a correction for the central power cusp feature, which deviates from the original β-model [97]. That is to say; the β parameter is designated to the slope of the electron density profile in this double β-model treatment, instead of bearing its original description $\beta = \mu m_p \sigma^2 / kT_{gas}$ referring to isothermal spheres. In essence, the purpose of this treatment is to find a smooth analytical function, which describes the electron density profile and also conserves its shape when integrated. The parameters are degenerate, meaning that different values for several parameters can result in the same curve, which does not affect the integration along the line of sight, and the β values by themselves should not be used to estimate further physical properties.

For modeling three dimensional temperature profiles, a broken power-law with five parameters and a temperature decline,T_{cool}(r), in the central region, r_{cool}(r), of the clusters are used as given in Eqn. 4.2 and Eqn. 4.3 [95]. This treatment is followed by the integration along the line of sight to deduce the projected "spectroscopic-like" temperature profiles as described by [98]. In case a temperature decline in the central region of the cluster of interest is not observed in its projected temperature profile, the parameter that defines the cool gas, T_{min}, is set equal to T_0, which then appoints the value of unity to the parameter T_{cool}(r). In contrast with the literature, the choice of label for temperature decline is used as T_{cool}(r) instead of t_{cool}(r), with the intention of dissociating the temperature decline parameter of the temperature model and central cooling time for clusters.

$$T_{3D}(r) = T_0 \frac{(r/r_t)^{-a}}{(1+(r/r_t)^b)^{c/b}} T_{cool}(r) \tag{4.2}$$

where;

$$T_{cool}(r) = \frac{x + (T_{min}/T_0)}{x+1}, x = \left(\frac{r}{r_{cool}}\right)^{a_{cool}} \tag{4.3}$$

Projected temperature profiles plotted over the corresponding three dimensional temperature profiles are shown in the related sections of the individual clusters. These methods are described in detail by Bourdin and Mazzotta (2008) [87]. Confidence envelopes for temperature profiles are propagated from Monte Carlo realizations of the fit analytical functions. Unless otherwise stated, these envelopes and error bars correspond to 68% confidence levels.

4.5. Spectroscopic Analysis

For certain clusters whose temperature and surface brightness maps as well as radial temperature profiles show interesting features at the central regions, such as surface brightness profile with a double β fitting requirement and a well defined cooler temperature component coincident with the BCG of the cluster, a further detailed spectroscopic analysis of centered at the position of the BCG is applied. For the spectral analysis, a fitting package *XSPEC* (v. 12.10.0) [99] of High Energy Astrophysics Software (HEASOFT) is used. In order to begin with a detailed spectral analysis, a circular region centered at the BCG of the cluster is selected defined by the guidance of the related radial temperature profiles of the cluster in question. In case this guidance is deemed insufficient, the radius of this region is selected as 0.01 R_{500}. If the cluster redshift is not low enough to resolve *XMM-Newton* point spread function (PSF), then the region radius is set equal to the PSF. The R_{500} values obtained from literature is presented in Table 3.1

The aim of this approach is to obtain a best model for the ICM emission from the region in case a single temperature `apec` model is seen to not properly describe the X-ray emission. Subsequently, a single temperature `apec` model, absorbed by a galactic hydrogen column density (N_H) with units of mean atomic hydrogen cm^{-2} specific to the position of the cluster, is applied. The `apec` model has four free parameters, namely; temperature in keV units, abundance in solar abundance ($Z_\odot$) units, redshift (z) and a normalization ($norm$). The `apec` model normalization is given as;

$$\left[10^{-14}/4\pi\left[D_A(1+z)\right]^2\right]\int n_e n_H dV \tag{4.4}$$

where the integrant is the emission measure (EM), n_e and n_H are electron and hydrogen densities in cm^{-3}, and D_A is the angular diameter distance of the cluster. Following the application of this model, the errors on temperature, abundance and normalizations are investigated where the redshift value is fixed.

An additional `apec` model is applied to examine the requirement of a cooler temperature model in order to search for a possible corona. Then, best-fit the statistics, namely C-stat/d.o.f (C / ν), of the models are compared. Depending on the result, a `powerlaw` model, which describes the power-law emission from an AGN, is added either to the single temperature or to the double temperature model. The model `powerlaw` has a dimensionless photon index parameter (Γ) and a normalization parameter, κ, with units of photons keV^{-1} cm^{-2} s^{-1} at 1 keV.

Photon counts of the spectra are grouped with a minimum of 5 counts per bin, therefore the data follow a Poisson distribution. The maximum likelihood-based statistics (hereafter, C-stat) for Poisson data proposed by Cash (1979) [100] is applied for this purpose. In this work, mean atomic hydrogen column density values retrieved from the N_H calculator tool [101] based on the methods of [84] and the data of The Leiden/Argentine/Bon (LAB) Survey of Galactic HI [85], and the redshift, z, specific to each cluster is retrieved form Piffaretti *et al.* [83], as presented in Table 3.1. All errors on spectral parameter values are presented with 1σ confidence levels, unless otherwise stated. At each spectra figure, upper curves correspond to the simultaneous fit of the *XMM-Newton* EPIC source and background counts, where the lower curves present the background model.

5. RESULTS AND DISCUSSION OF INDIVIDUAL CLUSTERS

In this section the analysis results of the cluster sample are presented. The sample description and the archival *XMM-Newton* observational properties are described in Chapter 3. In this context, the radial profile nomenclature refers to the values presented with respect to selected radial annuli which are centered at the BCG, and extend to a specific radius for a given cluster. A uniform emission within each annuli and spherical symmetry are assumed.

5.1. Abell 399

Abell 399 is found to be interacting with a nearby cluster, Abell 401, where neither of the clusters are reported to host an active galactic nucleus at their BCG [102]. A global temperature of $kT = 7.2$ is reported for this cluster [102].

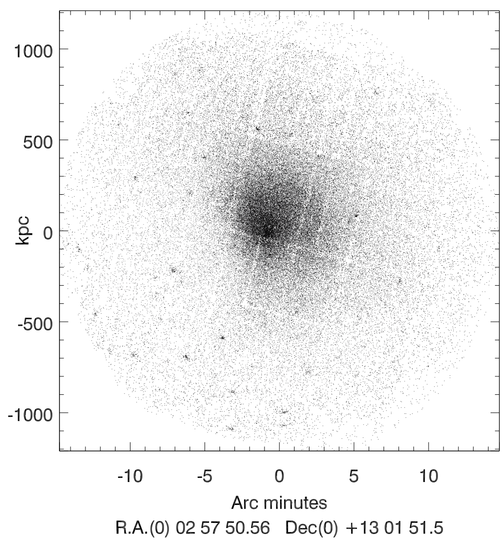

Figure 5.1. Photon image of Abell 399 in 0.3-2.5 keV band.

The photon image of Abell 399 shows an extended, prominent X-ray emission at the central region with $r \sim 300$ kpc with no evident X-ray peak that can be associated

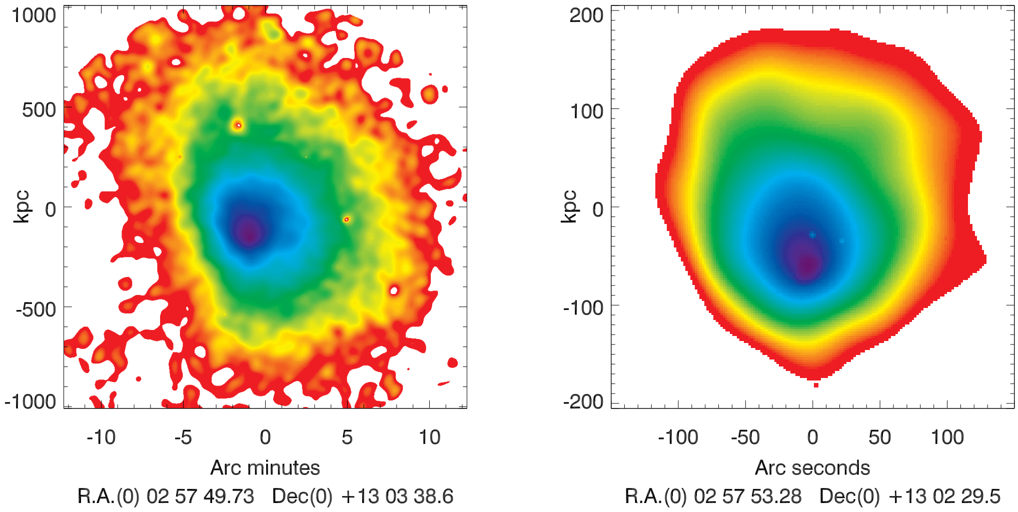

Figure 5.2. Surface brightness maps of Abell 399 enclosing the the FOV (*left*) and enlarged at the central region (*right*).

with the BCG, UGC 2438.

The enlarged surface brightness map of Abell 399 shown in the *right* panel Figure 5.2 suggests a motion in the southern direction which is in agreement with the suggestion that Abell 399 and Abell 401 have encountered each other, and are moving apart given that Abell 401 lies northeast of Abell 399 [102]. This scenerio may have caused the destruction of the AGN in the process, since neither a BCG X-ray peak is seen from the photon image nor a preserved central temperature structure is evident from the temperature maps.

For the analysis of the radial surface brightness and temperature profiles, 25 and 7 consecutive logarithmic bins are selected respectively. The shallow observation time of the cluster leads to poor statistics for this specific analysis when a larger number of bins are used. The fitting of the surface brightness profile required an additional α parameter, which implies that the central region has a rather cuspy nature instead of a flat one. The temperature profile of this system shows a flat distribution as expected from a typical NCC cluster. The shape of the profile as well as the temperature values are in agreement with the literature [102]. However, due to low photon statistics and

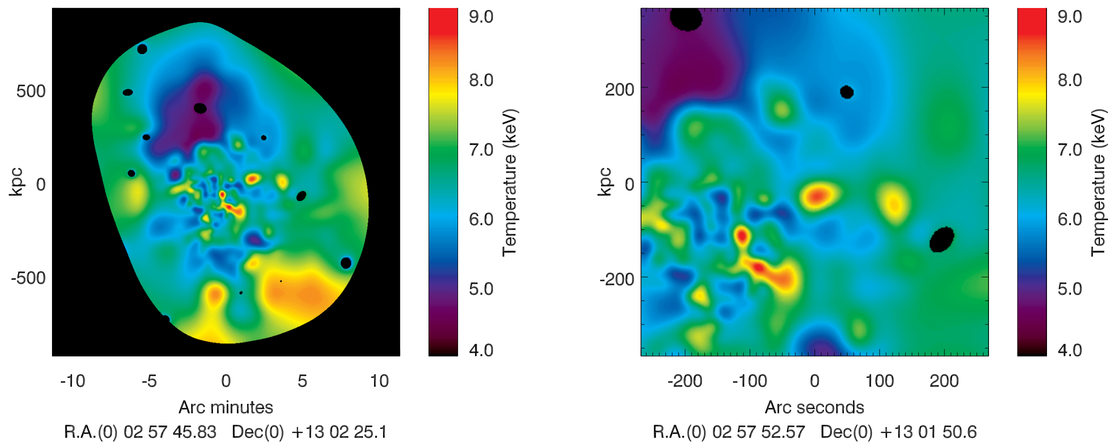

Figure 5.3. Temperature map of Abell 399 enclosing the the FOV (*left*) and enlarged at the central region (*right*).

temperature variations, the central 25 kpc region could not be included. With a deep observation, it is possible that a corona in the central region may be detected, as also evidenced by the multi temperature clumps in the central region of the cluster as shown in the *right* panel of Figure 5.3.

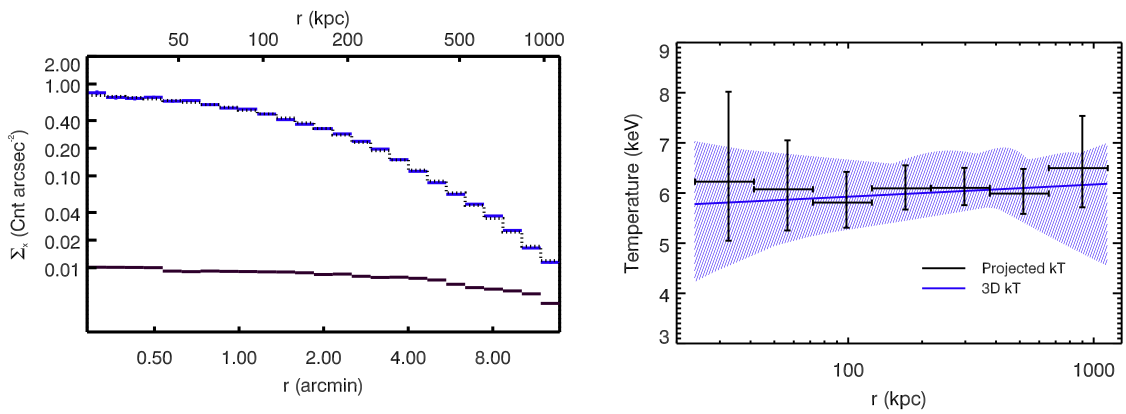

Figure 5.4. Surface brightness (*left*) and temperature (*right*) profiles of Abell 399.

5.2. Abell 400

Abell 400 hosts two radio sources namely 3C75A and 3C75B at the central region [103]. This double galaxy system is also evidenced by the photon image of the cluster as shown in Figure 5.5.

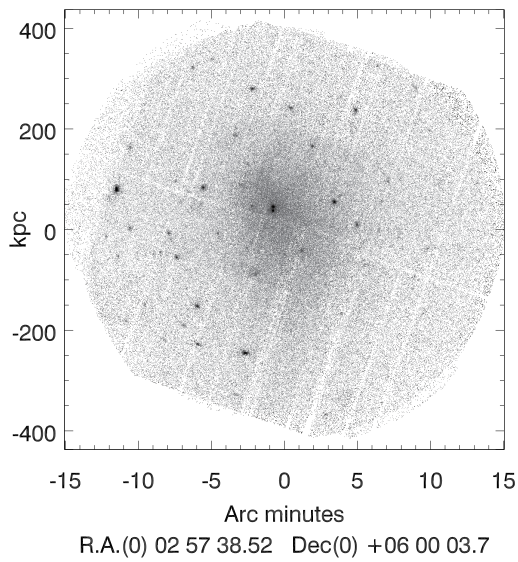

Figure 5.5. Photon image of Abell 400 in 0.3-2.5 keV band.

The surface brightness maps show the trace of a previous passage of another galaxy in the south-west direction *left* panel of Figure 5.6. The enlarged surface brightness map, *right* panel of Figure 5.6, shows evidence that the galaxies are in the process of a merger, and there is a bridge suggesting a strong interaction between.

Both temperature maps show strong anisotropies, yet interestingly the enlarged temperature map shows that the BCGs have conserved their integrity although they have distinct temperatures. This is in agreement with the findings of Hudson *et al.* (2016), who report a low temperature component at the center of the cluster with spectroscopic analysis, although their temperature map shows no such evidence of this feature [103]. The fit of the surface brightness profile requires a double β-model, where

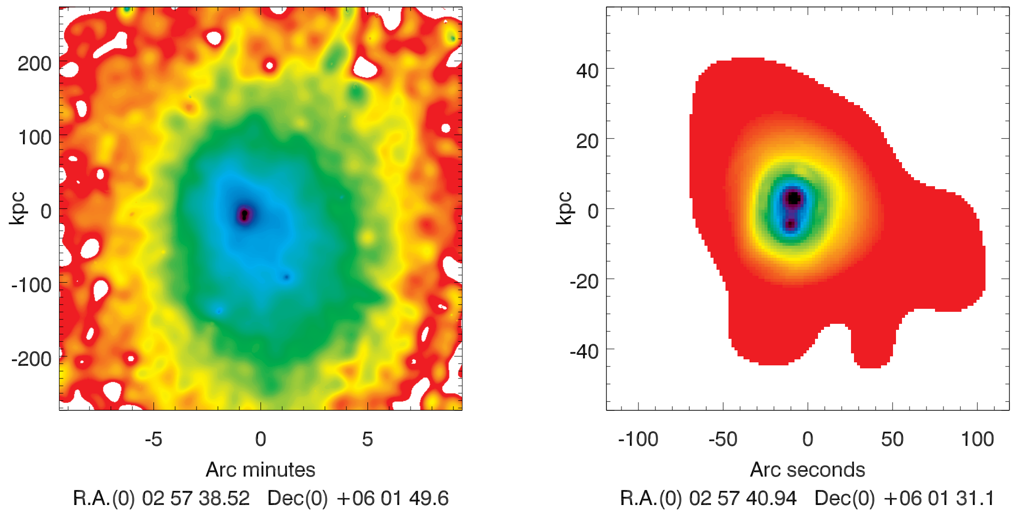

Figure 5.6. Surface brightness maps of Abell 400 enclosing the the FOV (*left*) and enlarged at the central region (*right*).

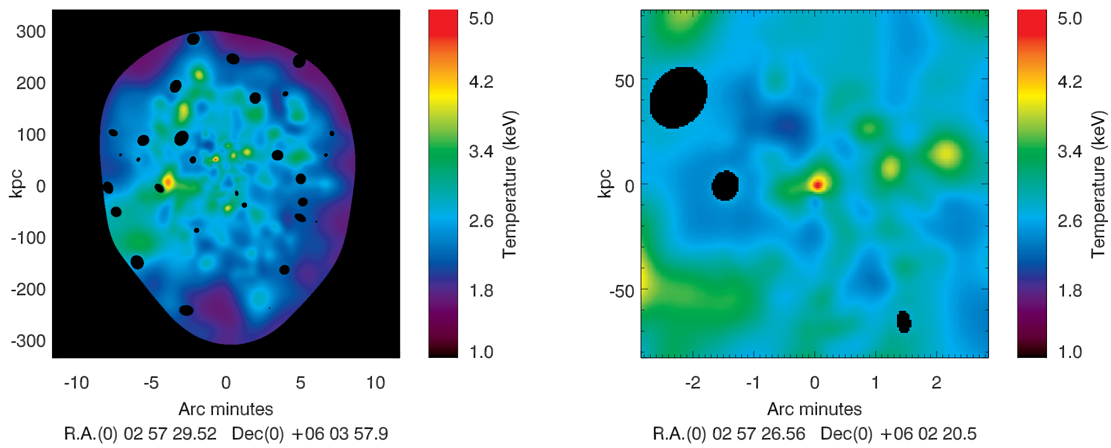

Figure 5.7. Temperature map of Abell 400 enclosing the the FOV (*left*) and enlarged at the central region (*right*).

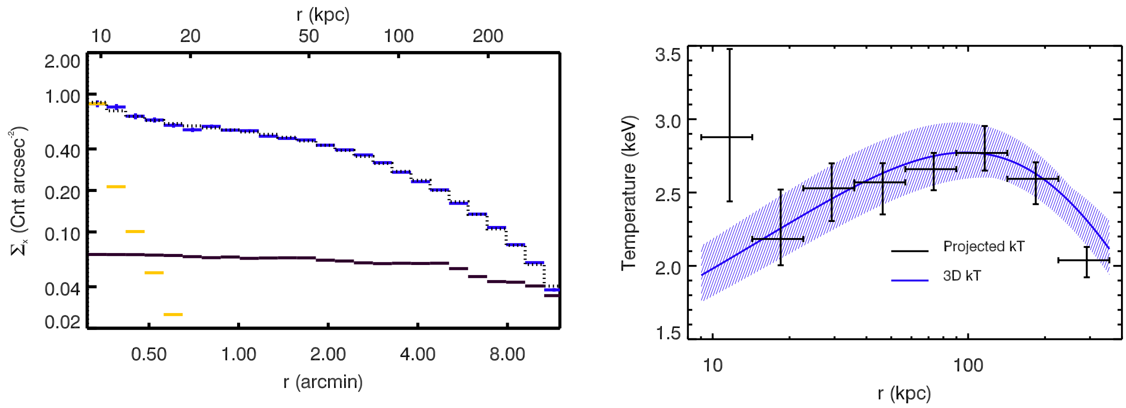

Figure 5.8. Surface brightness (*left*) and temperature (*right*) profiles of Abell 400.

the central region emission extends to $r \sim 20$ kpc. The temperature profile is quite similar to that of a cool core cluster, where there is a gradual increase up to $r \sim 100$ kpc, followed by a gradual decrease. Due to the double galaxy system at the central region, the errors of the first temperature bin is quite large. The reported overall cluster temperature by Hudson *et al.* (2016) [103] is also in agreement with the values presented here, however, having chosen large temperature bins ($\approx 1'$), they do not find any central temperature drop. This may be due to their choice of deprojection method, and the smaller FOV of the *Chandra* data they analyze, since the outermost regions may also contribute to the reported temperature values.

Individual selection of source regions ($r \sim 4$ kpc) enclosing each BCG for a spectral analysis is not achievable due to the PSF which corresponds to $r \sim 7.2$ kpc. A $r \sim 10$ kpc region is selected for spectral analysis where a temperature $kT = 0.78$ keV plasma is found along with a power-law emission with photon index $\Gamma = 1.42$ which may both favor the emission feature of an AGN or an X-ray binary system [104]. Due to the uncertainty of the resulting values, the spectrum is not presented here, and a high spatial resolution observation is required to resolve the X-ray emission form these sources.

5.3. Abell 401

A global temperature of $kT = 8.5$ keV is reported for this cluster who shows evidence of interaction with Abell 399 [102] (see Section 5.1). The photon image suggests an elongated ICM emission without a prominent X-ray peak coincident with the BCG, UGC 2450. The cluster morphology as seen from the photon image in Figure 5.9, presents an elliptical structure.

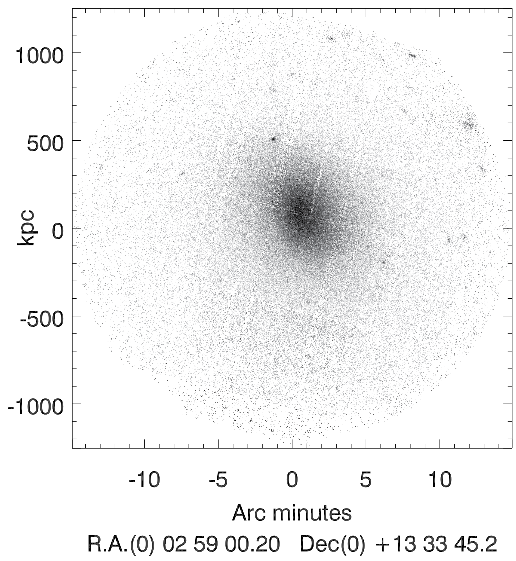

Figure 5.9. Photon image of Abell 401 in 0.3-2.5 keV band.

Surface brightness maps also suggests an elongated ICM emission in agreement with the scenario that the cluster may have passed by Abell 399 as discussed in Section 5.1.

A very hot spot to the south of the center of the cluster is detected in the temperature map of the cluster as shown in Figure 5.11, which also suggests a previous merger activity with Abell 399. The ICM temperature distribution is highly disturbed. This hot spot has been extracted from the data analysis at the point-source extraction stage, and it is possible that at this region was where the BCG used to be, but due the previous merger, the region might have been heated. It is also interesting that while a hot region is spotted at the southern part of this cluster, a cooler region was indicated

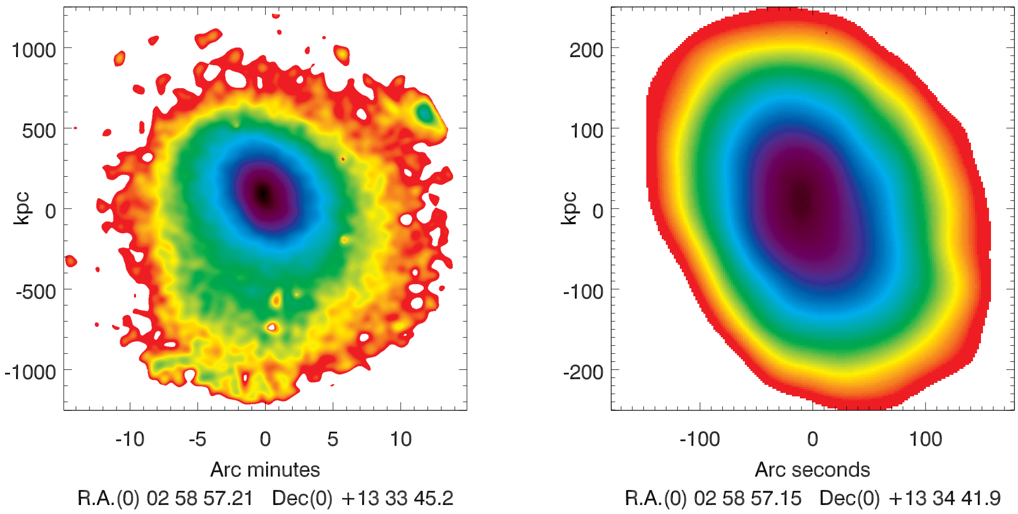

Figure 5.10. Surface brightness maps of Abell 401 enclosing the the FOV (*left*) and enlarged at the central region (*right*).

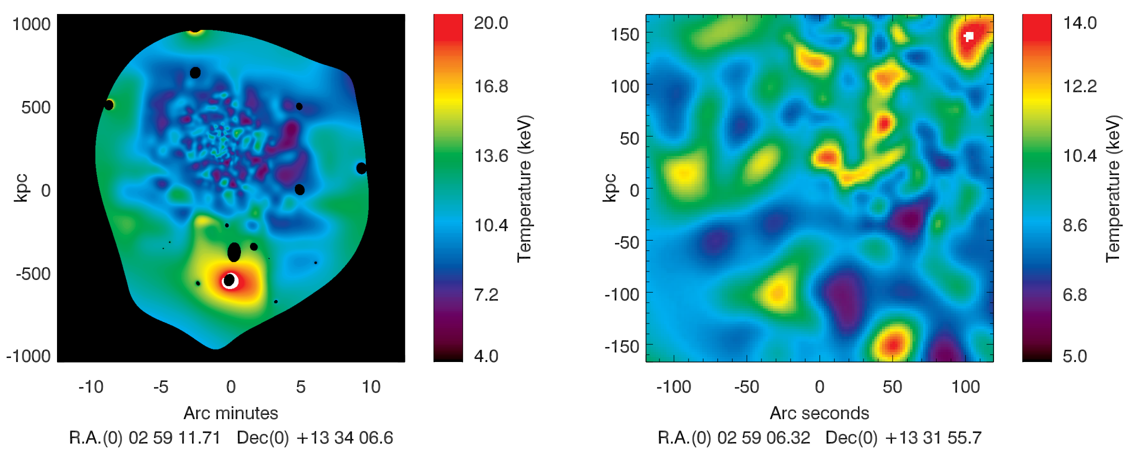

Figure 5.11. Temperature map of Abell 401 enclosing the the FOV (*left*) and enlarged at the central region (*right*).

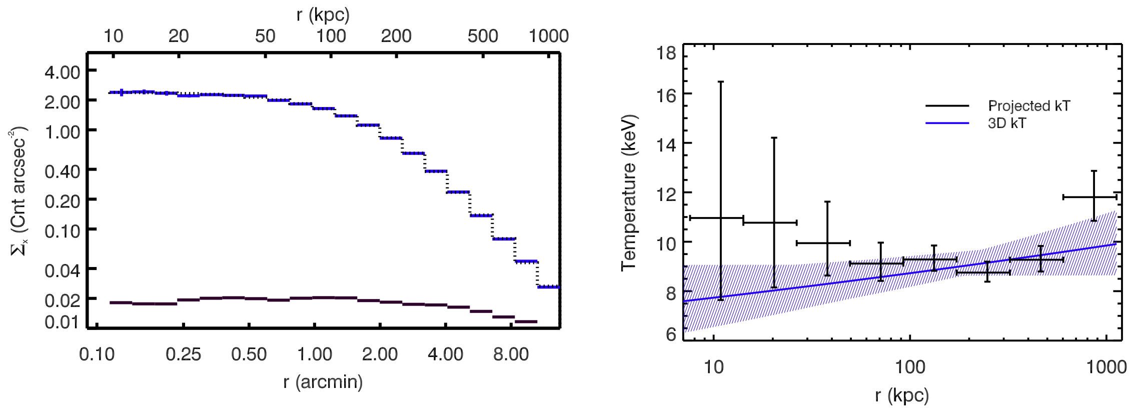

Figure 5.12. Surface brightness (*left*) and temperature (*right*) profiles of Abell 401.

by the temperature map at the northern part of Abell 399 (see Section 5.1, Figure 5.3).

Once again, as in the case of Abell 399, this cluster has a very short exposure time, therefore only 20 and 8 consecutive logarithmic bins are selected for the analysis of the radial surface brightness and temperature profiles, respectively. The radial temperature profile shows strong uncertainties in the central region, and has similar feature and values reported in the literature [102]. Unfortunately, due to the absence of an X-ray emission peak coincident with the BCG, a spectral analysis can not be performed for the BCG emission.

5.4. Abell 1656 - Coma Cluster

Coma is a well studied, very nearby cluster whose has two BCGs, where the first BCG, NGC 4874, is closer to the X-ray emission peak than the secondary BCG, NGC 4889 [82]. The photon image in Figure 5.13 is centered on the NGC 4874, where NGC 4889 lies at the east (left) of the primary BCG in the photon image.

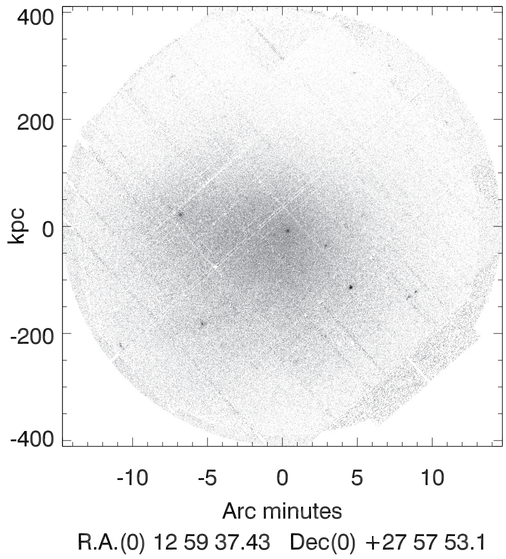

Figure 5.13. Photon image of Abell 1656 in 0.3-2.5 keV band.

Surface brightness maps show a homogenous X-ray emission distribution beyond $r = 100$ kpc, yet within $r = 100$ kpc the signs of an on going merger is evidenced. In addition, a tail-like structure around NGC 4874 is also evidenced.

Although Coma is previously described as a relaxed system based on two dimensional temperature map, the temperature map presented in the *left* panel of Figure 5.15 shows a strong anisotropy. However, amidst the merger and the multi temperature structure of the cluster, the enlarged temperature map (*right*) shows a cooler clump which is centered at the BCG. This BCG is reported to host a mini-cool core [81] in agreement with the maps presented in this work.

Surface brightness profile fitting of the Coma cluster required a double β-model, where 24 logarithmic bins are used. For the temperature profile, high quality data allowed the selection of 10 bins.

Surface brightness profile shown in the *left* panel of Figure 5.16, shows evidence that within $r = 10$ kpc, there is a distinct emission at the central region of the cluster which does not follow the emission curve from the ICM. It is also evident that this

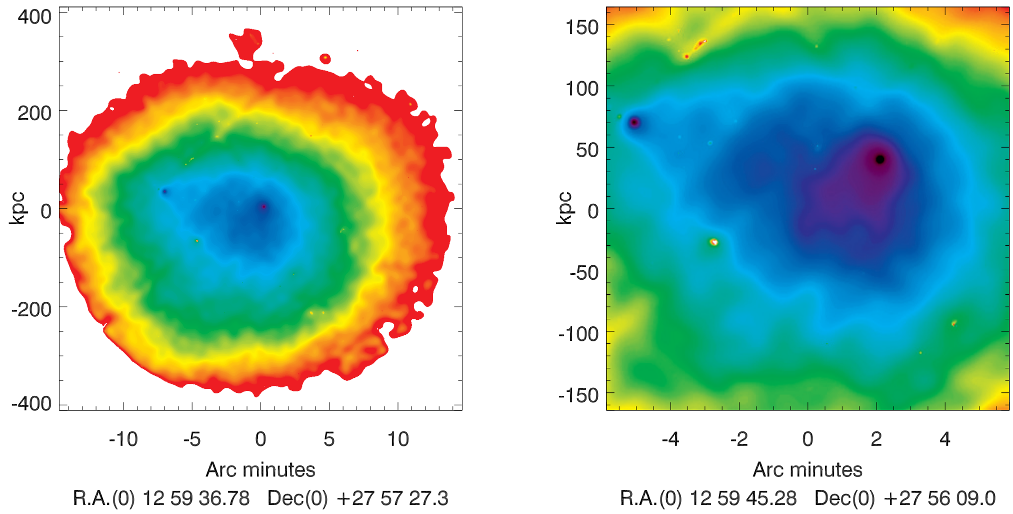

Figure 5.14. Surface brightness maps of Abell 1656 enclosing the the FOV (*left*) and enlarged at the central region (*right*).

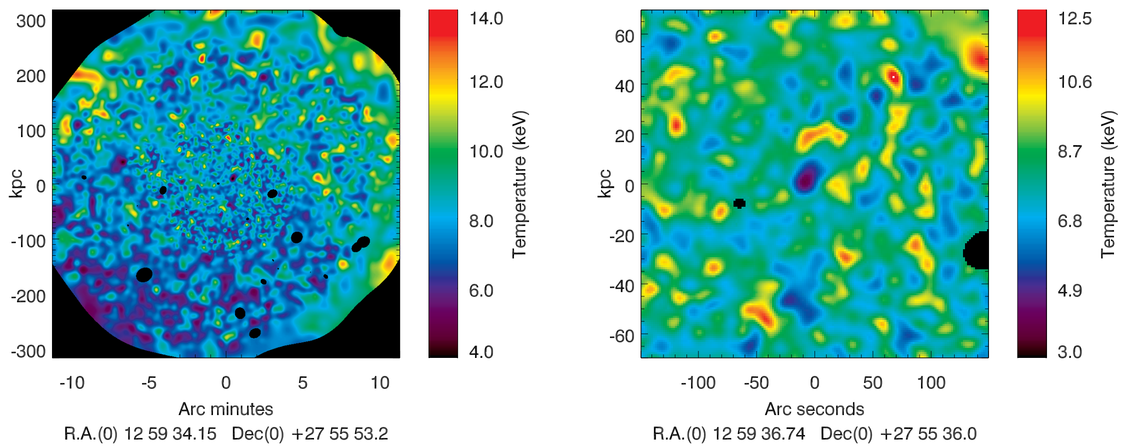

Figure 5.15. Temperature map of Abell 1656 enclosing the the FOV (*left*) and enlarged at the central region (*right*).

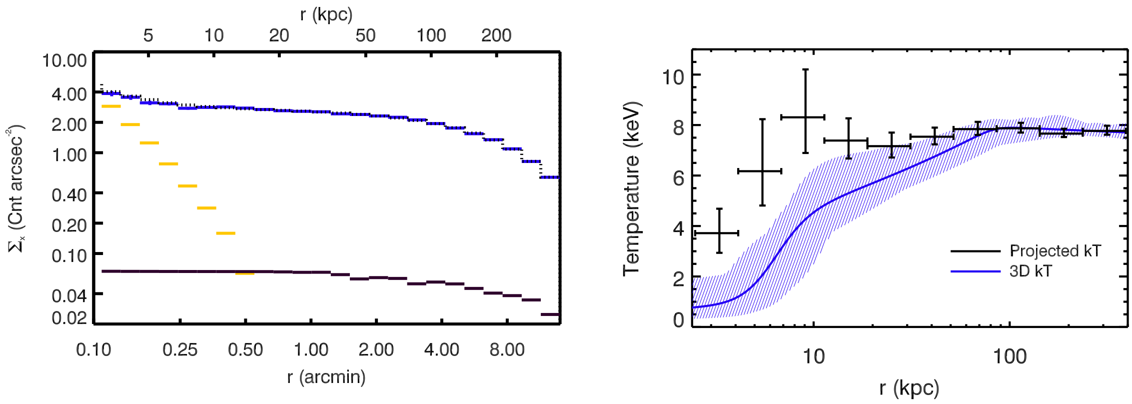

Figure 5.16. Surface brightness (*left*) and temperature (*right*) profiles of Abell 1656.

central emission extends beyond the *XMM-Newton* PSF (*yellow* curve), therefore is not an artifact of the PSF itself.

Although the projected temperature profile shows a gradient in the central region in the *right* panel of Figure 5.16, the deprojection of the profile (*blue* curve) shows that, it is merely a projection affect and the gas enclosed inside $r = 4$ kpc is isothermal.

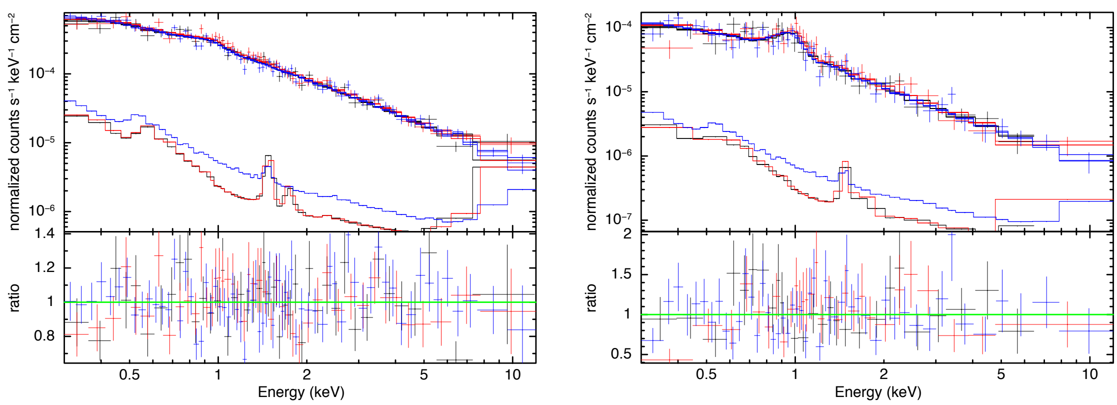

Figure 5.17. Spectral fit of NGC 4874 for Region 1 with $r = 11.5$ kpc. Adjacent bins are grouped until they have a significant detection at least as large as 6σ, with maximum 20 bins for Region 1, and 3σ with maximum 5 bins for Region 2, for plotting purposes only.

Table 5.1. Best-fit results of *XMM-Newton* EPIC spectra for Region 1 (r = 11.5 kpc) and Region 2 (r = 4 kpc) of Abell 1656.

Region 1	**phabs × (apec + apec + powerlaw)**
kT (keV)	$1.04^{+0.01}_{-0.03}$
Z ($Z_\odot$)	0.3 (fixed)
norm (10^{-5})	$3.54^{+0.71}_{-0.64}$
$\mathbf{kT_2}$ (keV)	$7.53^{+1.22}_{-1.42}$
$\mathbf{Z_2}$ ($Z_\odot$)	0.3 (fixed)
norm (10^{-4})	$3.12^{+1.28}_{-0.54}$
$\mathbf{\Gamma}$	$1.51^{+0.19}_{-0.11}$
$\boldsymbol{\kappa}$ (10^{-5})	$4.03^{+1.24}_{-2.39}$
C-stat / d.o.f.	290.25/307
Region 2	**phabs × (apec + powerlaw)**
kT (keV)	$1.21^{+0.09}_{-0.09}$
Z ($Z_\odot$)	1 (fixed)
norm (10^{-5})	$1.13^{+0.23}_{-0.16}$
$\mathbf{\Gamma}$	$1.58^{+0.05}_{-0.03}$
$\boldsymbol{\kappa}$ (10^{-5})	$1.51^{+0.12}_{-0.18}$
C-stat / d.o.f.	137.03/307

For the spectral analysis of the BCG of Abell 1656, we selected a circular region centered at the BCG with r = 11.5 kpc (Region 1), which corresponds to 0.01 R_{500}. This region has 2049 (MOS1), 2222 (MOS2) and 4208 (PN) net photon counts and corresponds to the central surface brightness extent shown in the *left* panel of Figure 5.16. Models of single temperature `phabs` × `apec`, multi temperature `phabs` × (`apec` + `apec`), and multi temperature and AGN power-law `phabs` × (`apec` + `apec` + `powerlaw`) are applied and the best-fitting model is found to be `phabs` × (`apec` + `apec` + `powerlaw`). This model suggests two distinct temperature plasma with a cooler (kT = 1.04 keV) and a hot (r = 7.53 kpc) component with a power-law photon index Γ = 1.51 which favors an AGN emission [104].

Furthermore, another region with r = 4 kpc (Region 2) is selected to investigate the coronal properties where the abundance is fixed at 1 $Z_{\odot}$ as expected from a BCG corona [81]. This region has 351 (MOS1), 386 (MOS2) and 731 (PN) net photon counts and corresponds to the isothermal region shown in the *right* panel of Figure 5.16

Firstly, the model `phabs` × `apec` is applied. This model resulted in with *C-stat* / *d.o.f.* = 199.93/151, where the spectra is poorly fit. Then, a power-law model is added to the spectra and the best-fit resulted in *C-stat* / *d.o.f.* = 137.03/150. This model again suggested a strong AGN emission evidence by the normalization, and a low temperature plasma. The addition of a second temperature model failed to improved the fit which suggests that the region encloses the corona alone and not the ICM emission. In addition, the Fe-L shell line bump seen in the spectra of Region 2 around 1 keV is also a characteristic of corona [81]. This finding is supporting the coronal parameters of NGC 4874 found by Sun (2009) [45], yet, as opposed to a temperature gradient in the central r = 4 kpc region, the deprojected temperature profile suggest a gas, which seems to be isothermal. The spectra are presented in Figure 5.17 and the best-fit results along with their 1σ errors are given in Table 5.1.

5.5. Abell 3158

In a study of the member galaxy velocity distribution of Abell 3158, the cluster is reported as a relaxed system [105]. The cluster is reported to be a centrally condensed and elliptically dominated cluster [106], where it hosts three central dominant galaxies at its central region [107]. A significant AGN emission is not found at the center of the cluster [75].

The photon image suggests a spherical ICM emission distribution but without an X-ray peak coincident with the cluster BCG, LEDA 13641. However, the surface brightness maps presented here show a slightly elliptical ICM emission as also reported in literature, and the absence of a bright core is supported by the work of Hudson *et al.* (2010) [31].

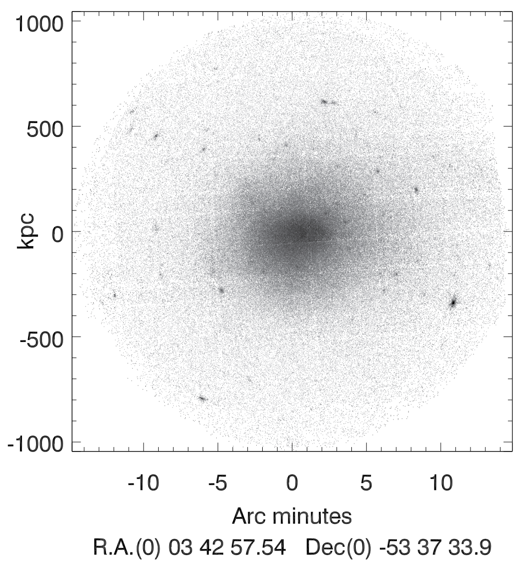

Figure 5.18. Photon image of Abell 3158 in 0.3-2.5 keV band.

Although it is described as a relaxed system [105], the temperature maps show strong anisotropy in the temperature distribution. A 2001 *ASCA* study of the cluster temperature map also suggests the absence of a spherically symmetric temperature distribution and points to a previous merger with a smaller cluster [108]. With a higher resolution data of *XMM-Newton*, this work presents a better spatially resolved

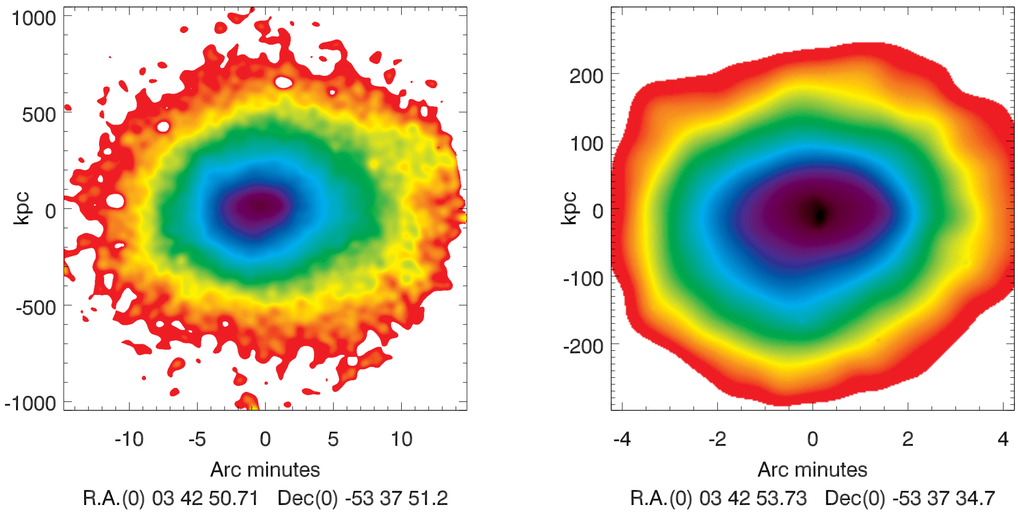

Figure 5.19. Surface brightness maps of Abell 3158 enclosing the the FOV (*left*) and enlarged at the central region (*right*).

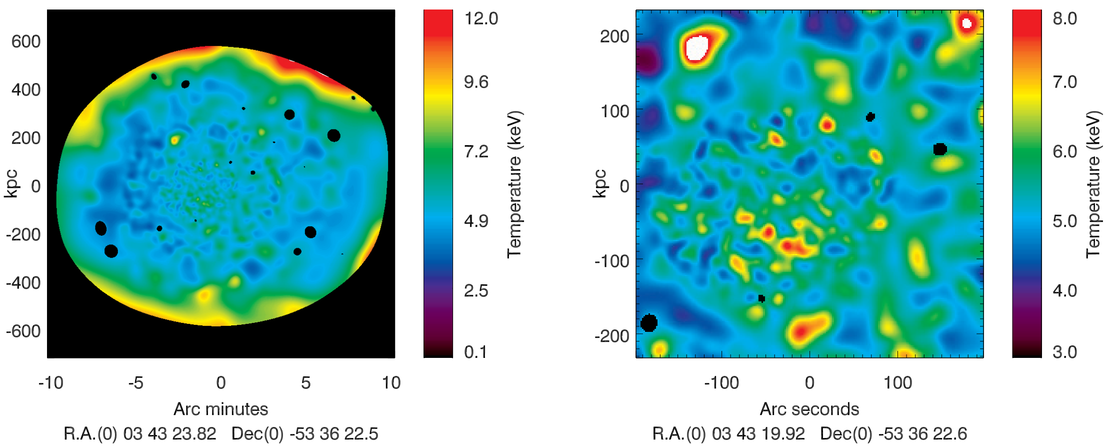

Figure 5.20. Temperature map of Abell 3158 enclosing the the FOV (*left*) and enlarged at the central region (*right*).

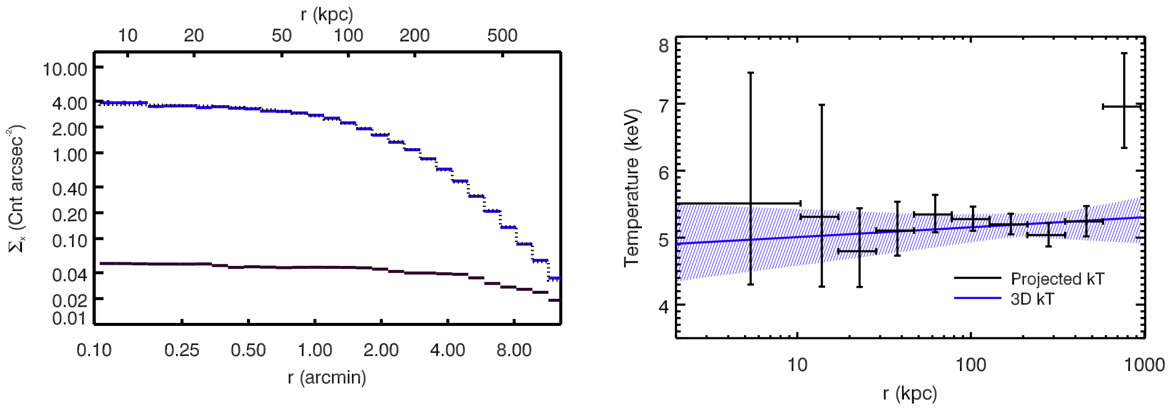

Figure 5.21. Surface brightness (*left*) and temperature (*right*) profiles of Abell 3158.

temperature map. Furthermore, the cluster is reported to move towards a double cluster system Abell 3125 and Abell 3128. The teperature map points to several cool gas clumps at the central region in agreement with literature, which is associated with a past merger event and may be due to a cool core remnant [75].

The surface brightness and temperature profile fitting of Abell 3158 was realized with 30 and 10 logarithmic bins for the surface brightness and temperature profiles, respectively. The surface brightness fit required an additional α component suggesting a not-flat surface brightness distribution. Temperature profile shows almost a flat ICM temperature distribution with high uncertainties in the central 20 kpc, as also evidenced by the temperature maps. Having no evident X-ray emission from the BCG, a spectral analysis is not suitable to study the BCG of the cluster in detail. The temperature of the central region is $\sim$ 5.5 keV, which is in a very good agreement with the reported central value of Hudson *et al.* (2010) [31]. However, the temperature profile provided Hudson *et al.* (2010) shows a very steep, centrally peaked temperature value, in agreement with the projected temperature profile presented here, yet the deprojection gives evidence that this peak can be a projection effect, and the cluster shows a rather flat temperature distribution.

5.6. Abell 3391

The ICM of Abell 3391 has elliptical shape where the BCG, ESO 161-7 is coincident with the X-ray emission peak [31]. A filament between this cluster and Abell 3395 was found [109]. The BCG is apparent on the X-ray photon image, and the elliptical shape is mildly visible.

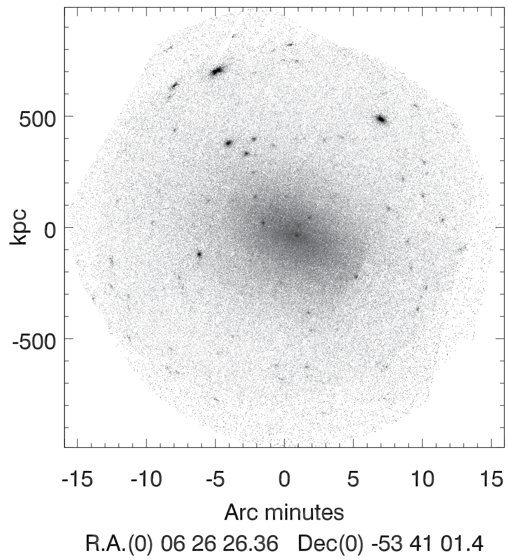

Figure 5.22. Photon image of Abell 3391 in 0.3-2.5 keV band.

With the help of the surface brightness maps, the elliptical shape of the distribution of the ICM is more prominent than as seen by the photon image. The emission peak is centered, with no strong inhomogeneity.

A cool ($\simeq$ 3.5 keV) circular region of a few kpc at the center of the enlarged temperature map is surrounded by a hotter ICM, with a few clumps of much hotter regions. The temperature map covering the *XMM-Newton* FOV does not show strong anisotropy. The surface brightness and temperature maps point to a rather relaxed morphology.

The best-fit of the projected surface brightness profile is achieved with a double-β model along with an additional α parameter contribution pointing to a corona emis-

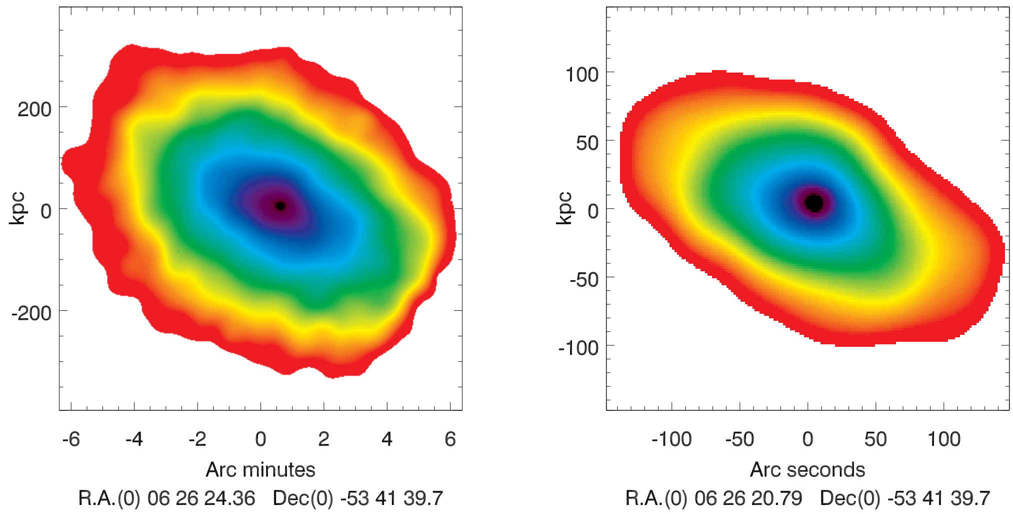

Figure 5.23. Surface brightness maps of Abell 3391 enclosing the the FOV (*left*) and enlarged at the central region (*right*).

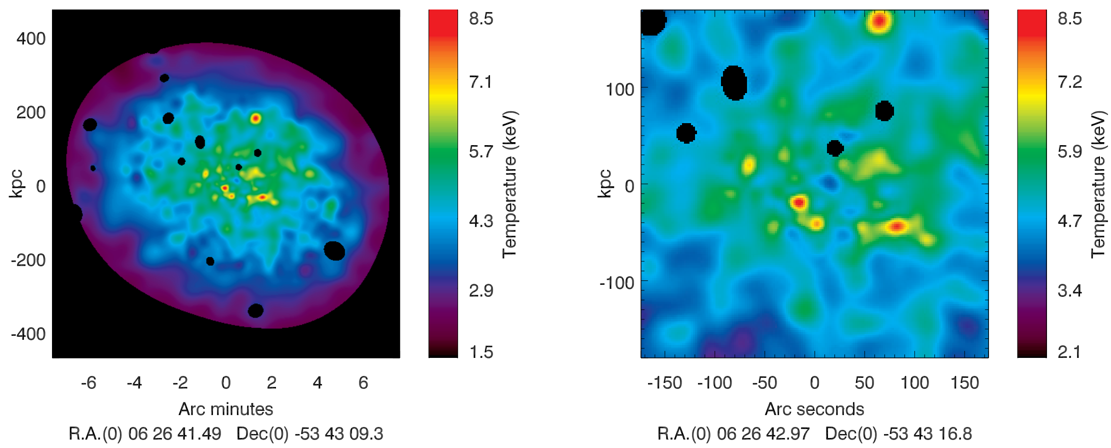

Figure 5.24. Temperature map of Abell 3391 enclosing the the FOV (*left*) and enlarged at the central region (*right*).

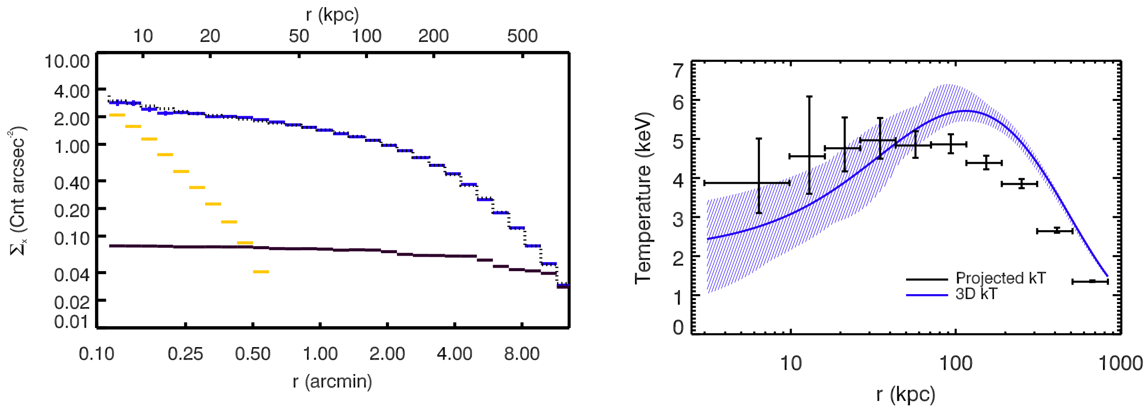

Figure 5.25. Surface brightness (*left*) and temperature (*right*) profiles of Abell 3391.

sion and the cuspy feature of the central region of the cluster, respectively. Up to $\simeq 50$ kpc, the projection effect of the outer regions is evident from the temperature profile. However, beyond 50 kpc, the elliptical ICM structure prevails over the spherical symmetry assumption of the deprojection technique. In addition, the temperature profile resembles to a cool core cluster temperature profile.

In order to investigate the cool clump at the central region of the cluster, a circular region of $r = 15$ kpc is selected, which is approximately the PSF radius. Since the 0.01 R_{500} corresponds to 9 kpc given the moderately high redshift of the cluster, the PSF is taken as the lower limit. This region has 640 (MOS1), 659 (MOS2) and 1384 (PN) net photon counts. The best model to describe the spectra is `phabs` × (`apec` + `apec`). Although an AGN powerlaw emission was found as suggested by Ineson *et al.* (2015) [110], its normalization was insignificant due to the large radius of the region, therefore `powerlaw` model was excluded to fit the spectra of this region. At $r = 15$ kpc, the AGN emission is negligible. This model suggests a two temperature plasma, a cooler one with kT (keV) $= 1.14^{+0.13}_{-0.08}$, and a hotter component kT (keV) $= 6.05$ $^{+0.85}_{-0.62}$. The abundance is well constrained with $Z = 0.39^{+0.14}_{-0.13}$ $Z_{\odot}$. This model resulted in a statistics with C-stat/d.o.f (C / ν) = 235.73/225. These finding are in very good agreement with the literature [110]. The spectral analysis of the central $r = 15$ kpc region provided a well constrained abundance value. In addition, this value supports the existence of a BCG corona as suggested by Sun (2009) as also evidenced by the

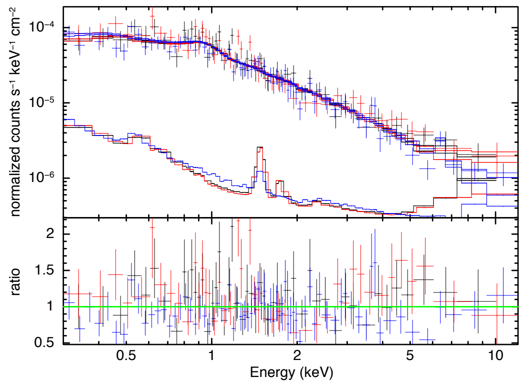

Figure 5.26. Spectral fit results of the BCG of Abell 3391, ESO 161-7, for the region with $r = 15$ kpc. For plotting purposes only, adjacent bins are grouped until they have a significant detection at least as large as 3σ, with maximum 10 bins.

Fe-L bump around 0.8 keV, which is a characteristic of a BCG corona [45].

5.7. Abell 3395

Abell 3395 is a double system at redshift $z = 0.0498$ hosting two sub-clusters as is evident from Figure 5.27. The cluster is classified as a merging clusters of galaxies by Lakhchaura *et al.* (2011) [111], and specifically at the stage of a near first core passage. These two sub-clusters are labelled as Abell 3395S and 3395N, where "S" denotes the sub-cluster lying at South of the double system, and "N" refers to the sub-cluster at North.

The BCG of A3395N is ESO 161-8, which is located at a distance of 11.6 kpc (or 0.008R_{500}) from the X-ray centroid of the sub-cluster [82]. Therefore, although A3395 is a merging system, the sub-cluster of A3395N is classified as a relaxed system according to X-ray offset criteria introduced by Lopes *et al.* (2018) [82]. The double elliptical structure of the ICM of the cluster, prevents to apply a deprojection technique in order to present a radial profile of this cluster.

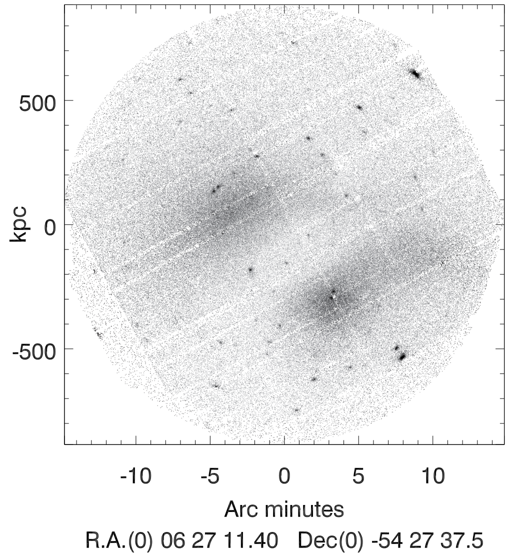

Figure 5.27. Photon image of Abell 3395 in 0.3-2.5 keV band.

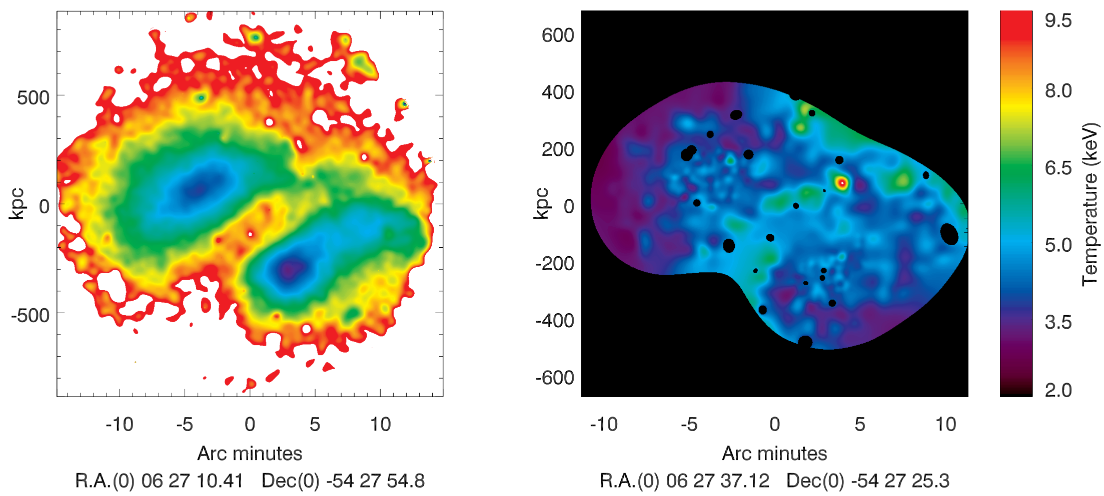

Figure 5.28. Surface brightness map (*left*) obtained in soft energy band 0.3-2.5 keV and temperature maps (*right*) of Abell 3395.

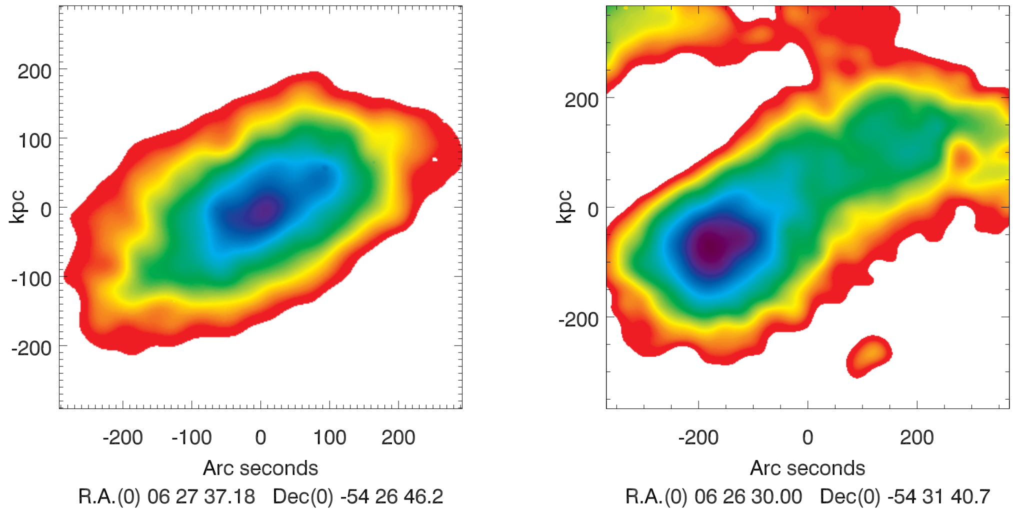

Figure 5.29. Surface brightness maps of northeast section; A3395N (*left*), and southwest section; A3395S (*right*).

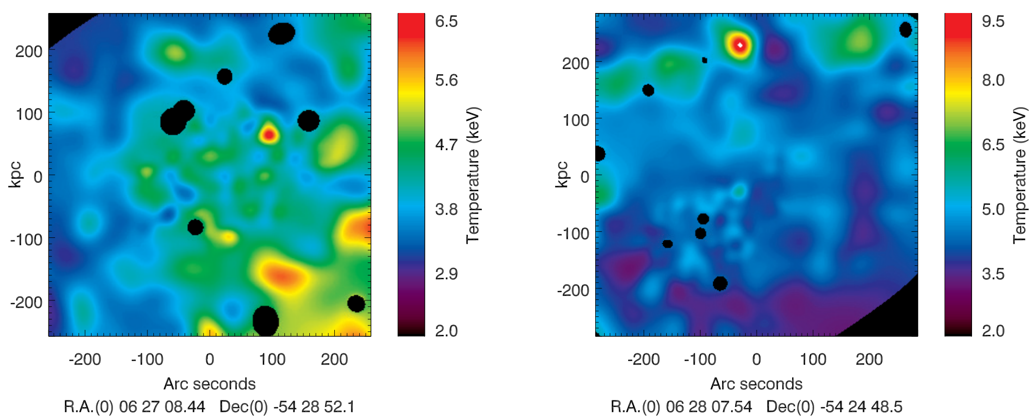

Figure 5.30. Temperature maps of northeast section; A3395N (*left*) and southwest section; A3395S (*right*).

5.8. ZwCl 1215

The galaxy cluster ZwCl 1215 at the redshift $z = 0.0766$ [83], is classified as an NCC cluster due to its slow central cooling rate $t_{cool} = 10.99$ Gyr with no bright central X-ray emission peak [31]. The BCG of the cluster is LEDA 39445 whose optical position is 22.9 kpc away from the X-ray emission peak position [112] using a single *Chandra* observation with short (12ks) exposure time. However, due the presence of a confusing structure and/or the lack of presence of a cooling core, the authors emphasize the uncertainty of the X-ray core position which they report. They also report a cooling time value of $t_{cool} = 15.8^{+6.4}_{-5.9}$ Gyr at $r = 37$ kpc. They report the absence of central radio sources and bubbles. Lovisari and Reiprich (2019) report a central abundance value of $Z = 0.33\ Z\odot$ at the core radius which is defined within 0.3 R_{500} [113]. They use $R_{500} = 1.0548$ Mpc reported by the work of [83]. In their dynamical state study of a cluster sample, [82] reports a BCG - X-ray emission peak offset of $r = 2.1$ kpc (0.001 R_{500}). Given that this value is much lower than their offset cut of 0.01 R_{500} to distinguish between relaxed and disturbed systems, ZwCl 1215 is categorized as a relaxed system. The overall temperature of the cluster was reported as $kT = 6.62$ keV by [40] and as $kT = 6.54$ keV by [38]. The merger activity of this cluster is not reported in literature to the best of our knowledge.

The photon image of shown in Figure 5.31 does not reveal a prominent X-ray peak nor a well defined spatial structure which can be attributed to the BCG of the cluster. The emission from the central region is nearly round without any immediate evidences of substructures formed by a merger activity.

The position of the BCG is not evident from the temperature map since there are strong anisotropies of temperature at various scales. A central hot region is surrounded by multiple cooler regions inside $r \simeq 50$ kpc.

The surface brightness maps are centered at the optical position of the BCG obtained from the Sloan Digital Sky Survey and a low cut-off for the high end of the brightness threshold in order to emphasize the brightness peak is used. The overall

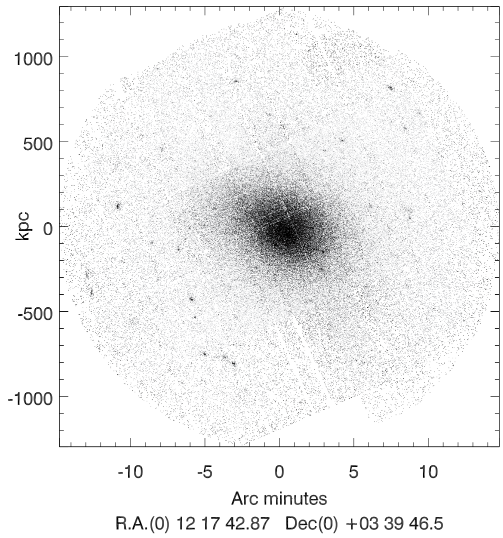

Figure 5.31. Photon image of ZwCl 1215 in 0.3-2.5 keV band.

cluster surface brightness map shown in the left panel of Figure 5.32 shows a rather elliptical/elongated structure.

The ICM surface brightness and temperature profiles are extracted from a circular region of $r = 12'$ in the energy band of 0.5 - 2.5 keV. Surface brightness profile is extracted with logarithmic binning of the data in 30 concentric annuli. For the temperature profile, eight bins are used, which are fit by a single temperature `apec` model. The inner radius of the first bin is limited to the value of $r \simeq 20$ kpc since including smaller radial regions in the profile resulted in large error bars which may be due to the multi-temperature structures at this spatial scale.

The surface brightness profile was fitted smoothly with a single β-model without the requirement of an additional β-model to describe the central region of the cluster.

The radial temperature profile shows the projection effect at the scale $r \simeq 100$ kpc. In the central region, namely the first bin, a relatively large scatter of the temperature value can be seen, which may be caused by a possible multi-temperature plasma. The radial pressure profile shows that in the inner $r \simeq 100$ kpc, the gas is in pressure

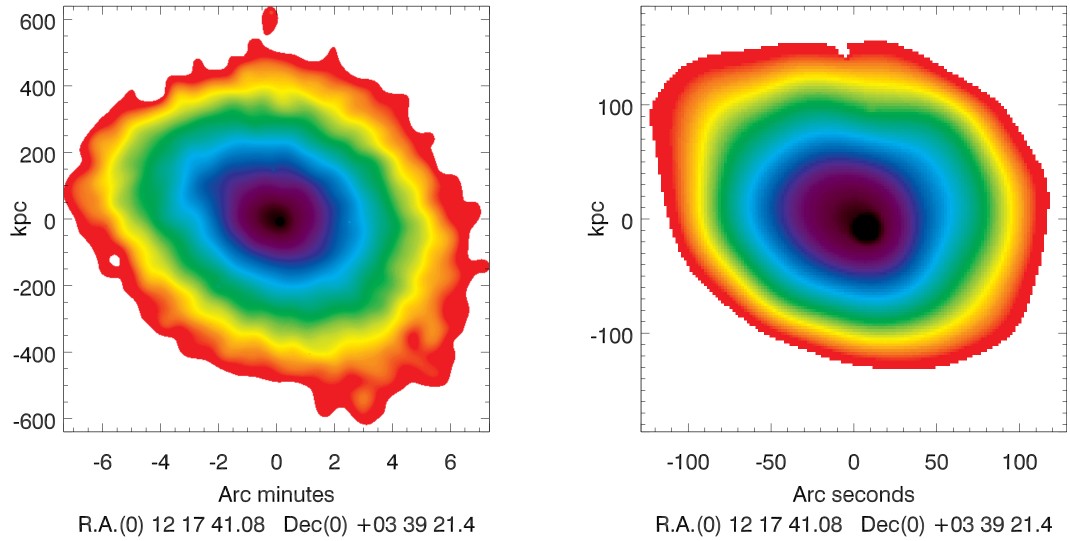

Figure 5.32. Surface brightness maps of ZwCl 1215 enclosing the the FOV (*left*) and enlarged at the central region (*right*).

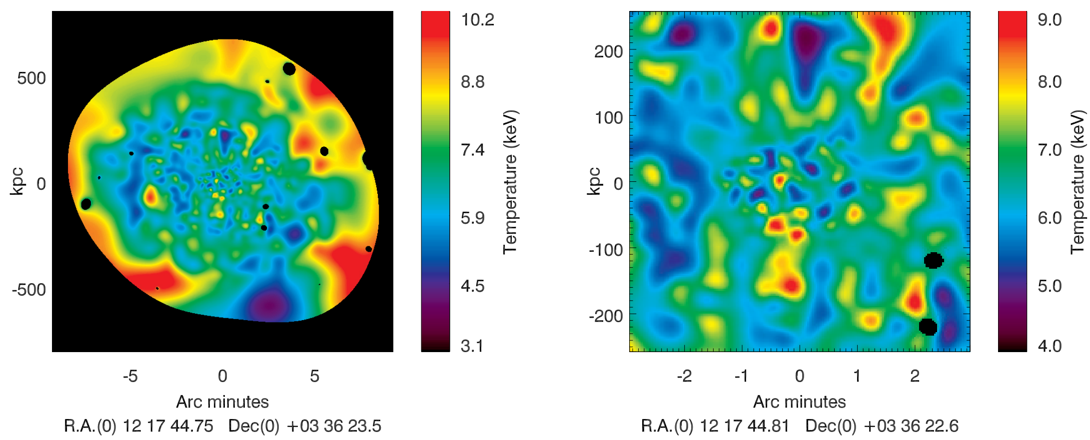

Figure 5.33. Temperature map of ZwCl 1215 enclosing the the FOV (*left*) and enlarged at the central region (*right*).

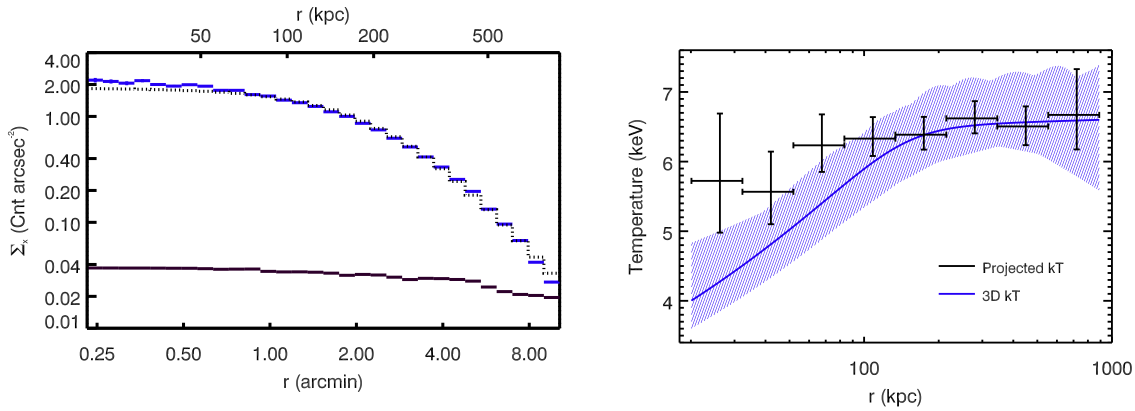

Figure 5.34. Surface brightness (*left*) and temperature (*right*) profiles of ZwCl 1215 centered on the BCG.

equilibrium then shows a gradual decrease in the range 100 kpc $< r <$ 1 Mpc.

For the spectral analysis of the central region of the cluster using the *XMM-Newton* data, three consecutive regions centered at the position of the BCG are selected in order to investigate the effect of the multi-temperature plasma as pointed out by temperature map shown in Figure 5.33. These regions enclose the spatial extent of the first bin (r = 30 kpc) in the temperature profile as shown in Figure 5.34 where there is a significant uncertainty in the temperature values which points to a multiple component plasma.

Region 1 is a circular region with $r = 10$ kpc where the temperature map points to multiple temperature components shown in Figure 5.33. The extent and/or existence of multi-temperature components are investigated in two more regions selected as annuli, namely Region 2 for 10-20 kpc and Region 3 for 20-30 kpc.

A single temperature `apec` model absorbed by a galactic hydrogen column density, i.e. `phabs` × `apec`, with *XSPEC* is implemented for all regions as a first estimate. Following the spectral fit with a single temperature model, another `apec` component is added in order to investigate the existence of multiple component plasma. Only for Region 1, an additional `powerlaw` component is used to investigate the affect of an

AGN.

Single temperature fit of Region 1 suggests a $kT \simeq 5$ keV plasma where the plasma abundance is fixed at the value $Z = 0.33\ Z_{\odot}$ as suggested by the work of Lovisari and Reiprich (2019) [113]. When the abundance is freed to vary, the abundance is $Z = 0.3$ $Z_{\odot}$, however the lower limit reaches zero with a higher limit of 0.65 $Z_{\odot}$. C-stat/d.o.f ($C\ /\ \nu$) is found to be 61.48/70.

Adding a `powerlaw`, namely using model `phabs` × (`apec` + `powerlaw`), results in a slightly improved statistics ($C\ /\ \nu = 57.21/68$) with a well constrained photon index Γ $= 1.65^{+0.06}_{-0.07}$ which is consistent with a typical AGN emission. Interestingly, the resulting temperature value is found to be $kT \simeq 1$ keV. This temperature value is consistent with a typical BCG corona temperature as suggested by Sun *et al.* (2007) [81].

An additional `apec` component does not improve the best-fit, therefore a two temperature plasma model without the power-law component, namely `phabs` × (`apec` + `apec`) is used. This model suggests two distinct temperature components. Hotter temperature is found to be $kT \simeq 5.8$ keV, whereas cooler component is $kT \simeq 0.5$ keV. This second temperature value is within the range of X-ray embedded corona. With this model, the abundance is well constrained and yielded a value of $Z = 0.46\ Z_{\odot}$.

For Region 1 and Region 2, the same tests are applied and a single temperature model presented with the best statistically significant results for both of these regions. Although there is a gradual decrease in the abundance value from Region 1 through Region 3, the temperature values do not demonstrate a distinct increasing profile.

The best-fit results of these models are presented in Table 5.2. The spectra is shown in Figure 5.35.

The surface brightness maps in Figure 5.32 show an elliptical cluster structure as opposed to a round one as suggested by Hudson *et al.* (2010) [31] who utilized the short *Chandra* observation for their analysis. With the larger field of view (FOV) and

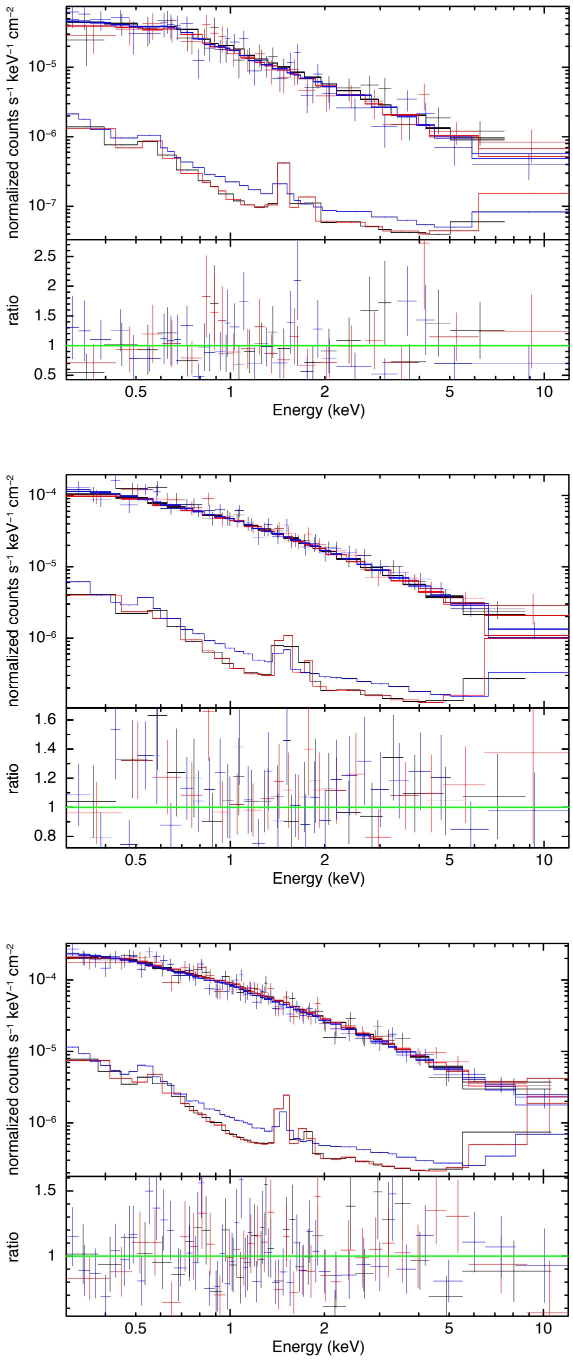

Figure 5.35. The spectral fit of Region 1, Region 2 and Region 3 of ZwCl 1215 from top to bottom respectively. Adjacent bins are grouped until they have a significant detection at least as large as 4σ, with maximum 10 bins for plotting purposes only.

Table 5.2. Spectral parameters and 1σ uncertainty ranges of *XMM-Newton* EPIC spectra for Region 1, Region 2 and Region 3 centered on the BCG of ZwCl 1215.

Region 1 (10 kpc)	**phabs × (apec + apec)**
kT (keV)	$6.14\ ^{+1.45}_{-1.04}$
Z ($Z_\odot$)	$0.46\ ^{+0.37}_{-0.40}$
norm (10^{-5})	$3.91^{+0.45}_{-0.59}$
$\mathbf{kT_2}$ (keV)	$0.40^{+0.72}_{-0.11}$
$\mathbf{Z_2}$ ($Z_\odot$	0.46 (tied to Z_1)
norm (10^{-6})	$2.98^{+19.2}_{-1.38}$
C-stat / d.o.f.	55.52/67
Region 2 (10-20 kpc)	**phabs × apec**
kT (keV)	$7.57\ ^{+1.09}_{-0.95}$
Z ($Z_\odot$)	0.27 ±0.23
norm (10^{-4})	1.12 ±0.07
C-stat / d.o.f.	130.72/166
Region 3 (20-30 kpc)	**phabs × apec**
kT (keV)	6.07 ±0.48
Z ($Z_\odot$))	$0.22^{+0.15}_{-0.13}$
norm (10^{-4})	2.04 ±0.10
C-stat / d.o.f.	190.29/228

relatively longer exposure time of the *XMM-Newton* this feature is presented. The temperature map shows hot and cool clumps especially at the central region at large range of values and the temperature structure as well as the temperature values are similar to the 2D maps presented by Lagana *et al.* (2019) [76].

The temperature profile presented by Cavagnolo *et al.* (2009) [40] has large scatter of values given the aforementioned issues, however their reported overall cluster temperature is in good agreement with the findings presented here. An important distinction is that, since their first annular bin comprises a region with the scale r = 100 kpc, the temperature profile presented here resolves the temperature gradient residing inside these region. The temperature value of kT = 6.54 $\pm$0.21 keV from literature [38], is also in agreement with the reported values in this work.

A central abundance value of Z = 0.33 $\pm$0.024 $Z_{\odot}$ is reported by Lovisari and Reiprich (2019) [113] for $r \simeq$ 300 kpc, using the only *XMM-Newton* observation of the cluster. This value is lower than the *XMM-Newton* abundance value of Z = 0.46 $^{+0.37}_{-0.40}$ $Z_{\odot}$ at r = 10 kpc found here, which is reasonable given that the cluster abundances tend to increase from the outskirts to the central regions [113] and in this work thermodynamical profiles of the cluster at various smaller scales compared to literature are reported. The central abundance values reported in this work from spectral analysis are in agreement with their work within 1σ errors.

Although Lopes *et al.* (2018) [82] reports ZwCl 1215 as a relaxed system based on the BCG - X-ray emission peak offset criteria, the temperature map presented here shows a disturbed morphology with multiple temperature regions at the center, in agreement with the findings of Lagana *et al.* (2019) [76] who categorizes the cluster as a disturbed cluster based on 2D maps. However, they also state that the cluster is an NCC type along with [31], yet the temperature profile presented here resembles to that of a cool core cluster, and spectral analysis suggests a possible presence of a corona also given the low temperature component at r = 10 kpc. Temperature maps supports the idea that the cluster may be subjected to multiple sub-clumps infalling for the first time [114].

6. MKW 08 IN DEPTH

NGC 5718 is the BCG of the galaxy cluster MKW 08 [115], which is categorized as a BCG corona by Sun *et al.* (2007) from the study of a single *Chandra* observation [81]. In their work, due to the lack of data quality of the single *Chandra* observation, a thorough study of this cluster was not achieved. The temperature profile of the cluster shows a gradual decrease from the central region to R_{500} showing a typical feature of a NCC cluster [116,117]. In this chapter, along with an *XMM-Newton* EPIC data, three deep *Chandra* archival observations are used to study both the ICM behavior and the corona. Data specifications are presented in Table 6.1.

Table 6.1. Effective exposure times of *XMM-Newton* EPIC and *Chandra* ACIS-I.

XMM-Newton **Observation ID**	**Equatorial coordinates (J2000)**	**EPIC effective exposure time (ks)**
0300210701	14 40 38.1 +0.3°28′18.1″	82.7
Chandra **Observation ID**	**Equatorial coordinates (J2000)**	**ACIS-I effective exposure time (ks)**
4942	14 40 38.3 +0.3°28′18.2″	23.1
18266	14 40 41.9 +0.3°28′4.4″	35.6
18850	14 40 41.9 +0.3°28′4.4″	39.6

The archival *XMM-Newton* data is used to study the ICM surface brightness and thermal structure at large, where the archival *Chandra* ACIS-I observations is used to investigate the central region and the BCG thanks to the a higher angular resolution of *Chandra*.

For *Chandra* a particle background model, the method proposed by Bartalucci *et al.* (2014) is adopted . This instrumental background is the sum of a continuum and fluorescence emission lines . This approach used an analytical model of the continuum

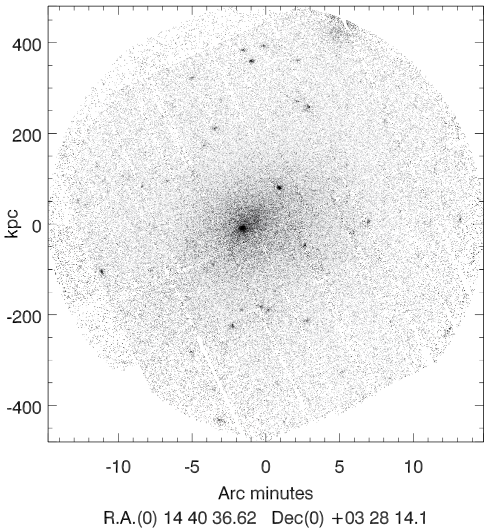

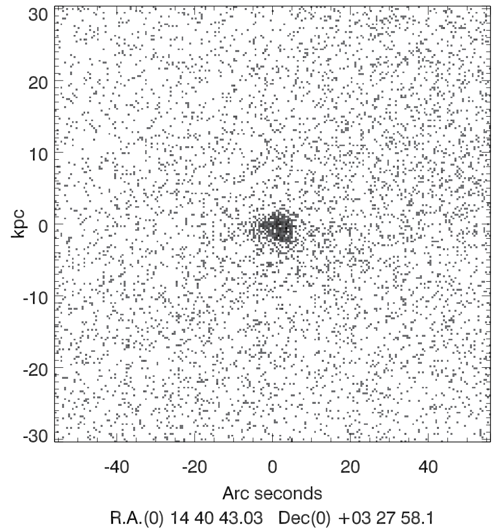

Figure 6.1. Photon images of *XMM-Newton* (*left*) and *Chandra* (*right*) of MKW 08 in soft X-ray (0.3-2.5 keV) band. Although a mosaic of three *Chandra* observations for background estimations were used, an enlarged image of *Chandra* (*right*) is shown in order to emphasize the BCG emission.

to fit the observations spanning eight years starting from 2001, in order to isolate the flux of ACIS-I instrumental background from sky components. Blank-sky observations during this period was used to fit the eleven fluorescence emission lines. The fit of the resulting spectra is presented in the appendix section of this work.

6.1. Cluster emission

6.1.1. ICM surface brightness and temperature maps

Temperature and surface brightness maps of *XMM-Newton* and *Chandra* in Figure 6.2 show an extended emission from the BCG of the cluster facilitated by the low temperature feature, with the guidance of the optical image overlaid with *Chandra* X-ray contours. There are no strong anisotropies in *XMM-Newton* temperature map beyond $r \sim 100$ kpc. These features point to a relaxed system as suggested by Lagana *et al.* (2019) [76]. *XMM-Newton* surface brightness map shows an elliptical/elongated

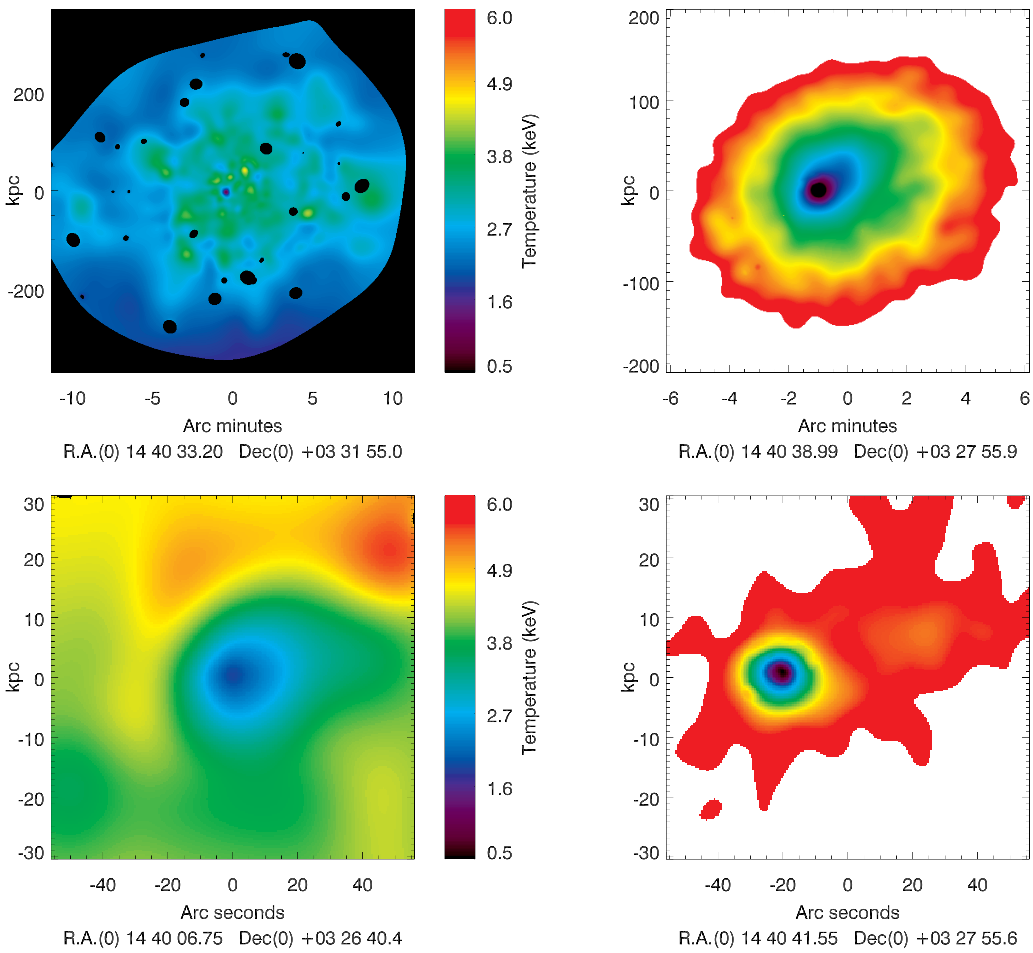

Figure 6.2. urface Brightness and Temperature Maps of MKW 08. *Upper panel: XMM-Newton* temperature map (*left*) and surface brightness map (*right*). *Lower panel: Chandra* temperature (*left*) and surface brightness maps (*right*).

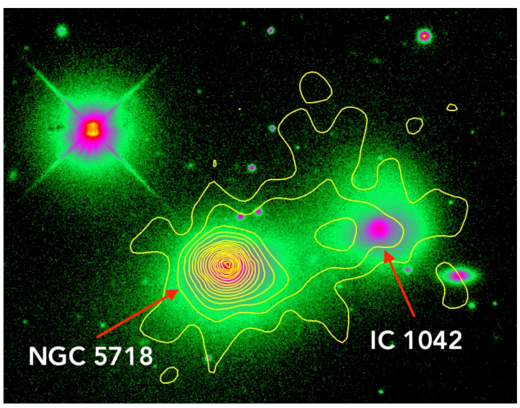

Figure 6.3. Optical image of the central BCG - NGC 5718 and IC 1042 in the I band overlaid with *Chandra* X-ray contours (*yellow*), which are equispaced by a factor $2^{1/4}$.

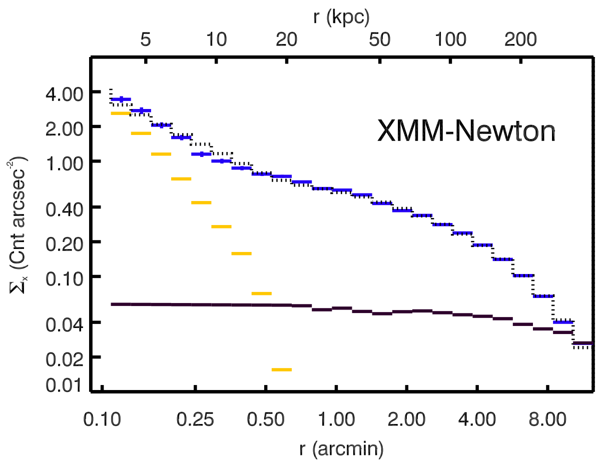

Figure 6.4. *XMM-Newton* surface brightness fitting with double β-model in the 0.5 - 2.5 keV energy band.

cluster core and the surface brightness map of the *Chandra* data shows a $\sim$ 40 kpc tail behind the BCG. A cold clump centered on the BCG, which is embedded in the hotter ICM is evident from both temperature maps.

6.1.2. X-ray Brightness Measurements and ICM Temperature Profiles

Surface brightness profiles are extracted with 25 logarithmic concentric annuli and for the temperature profiles, 11 and 10 bins are used for *XMM-Newton* and *Chandra* respectively.

The ICM surface brightness required double β-model along with the additional α parameter for both *XMM-Newton* and *Chandra*. High spatial resolution and deep exposure time of *Chandra* data enables to investigate the contributions of double β-model terms given in Eqn. 4.1. In order to visualize their contributions, n_0,$n_0 2$ and α parameters are set to zero at a time. With this approach, the location where the coronal gas emission is prominent is found to be $r \approx 4$ kpc.

The *XMM-Newton* projected temperature profile shown in Figure 6.6 presents an isothermal $r \leqslant 5$ kpc region with a temperature component $kT \simeq 1$ keV. The projected temperature values obtained from the *Chandra* data show the presence of

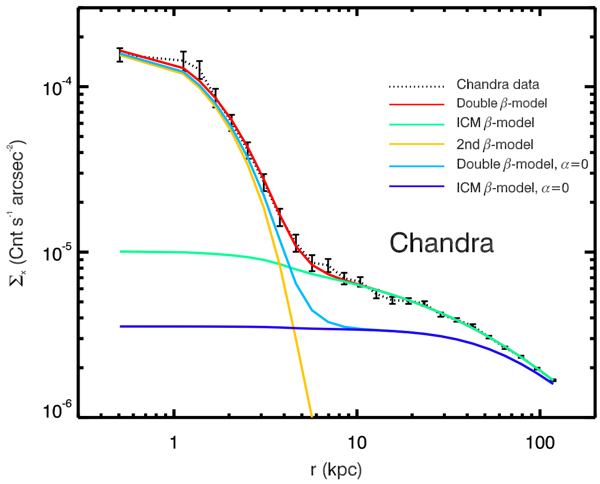

Figure 6.5. *Chandra* surface brightness fit of double β-model in 0.5 - 2.5 keV energy band. Projected surface brightness (*dotted black curve*); the double β-model (*red*); the β-model corresponding to the ICM (*green*); the second β-model corresponding to the corona (*yellow*); the double β-model with α parameter is set to zero (*light blue*); the β-model of the ICM with α parameter is set to zero (*dark blue*).

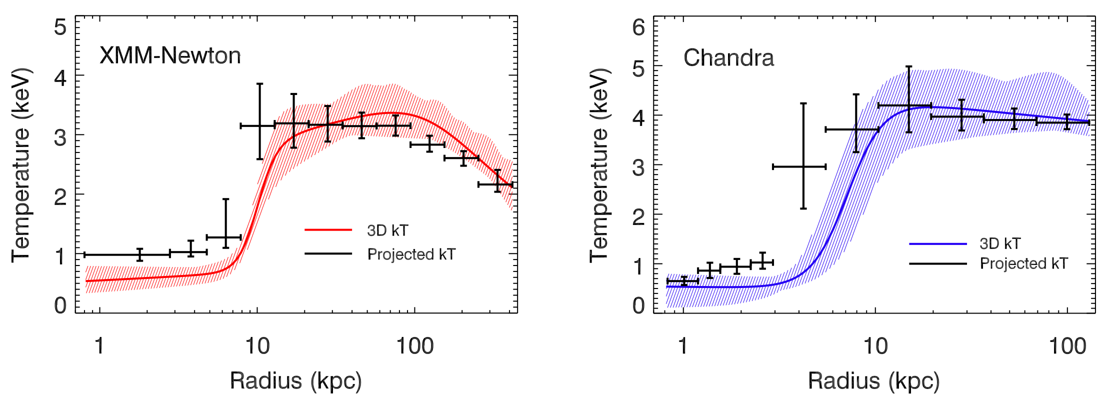

Figure 6.6. Projected radial ICM temperature values plotted over the three deprojected temperature profiles corresponding to $r = 12.5'$ for *XMM-Newton* (*top*) and $r = 4'$ for *Chandra* (*bottom*) as described in Section 6.1.2. Confidence envelopes for *XMM-Newton* (*red*) and *Chandra* (*blue*) were propagated from Monte Carlo realizations of the fitted analytical functions.

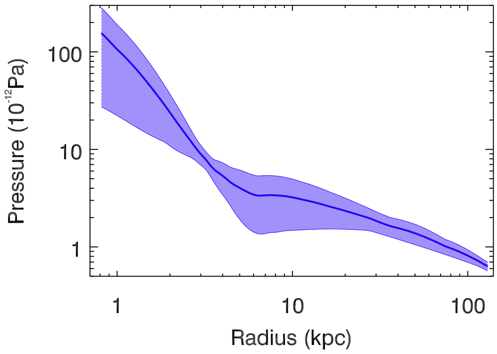

Figure 6.7. Hot gas pressure profile of MKW 08, centered on the BCG NGC 5718.

gradient within $r \leqslant 3$ kpc. With the deprojection, it is seen that the gradient is not physical but is due to the projection effect and the gas is isothermal up to $r \simeq 4$ kpc. Using fundamental thermodynamic equations for an ideal gas, a 3-dimensional pressure profile is also obtained given the profiles of electron density and temperature. There is an interface region, $4 \leqslant r \leqslant 10$ kpc, where there is a pressure slope distinguishable from both the inner and outer region.

6.2. Spectral analysis of the BCG: NGC 5718

6.2.1. *XMM-Newton* EPIC spectral fitting

As suggested by the surface brightness and temperature profiles, a circular $r = 10$ kpc region centered at the BCG is selected, which has 595 (MOS1), 629 (MOS2), 1481 (PN) net photon counts. Three spectral model was applied to obtain a best-fit of the spectra. *Model 1* is a single temperature model, namely; `phabs` × `apec`, *Model 2* has multi temperature components, i.e.; `phabs` × (`apec` + `apec`), and *Model 3* is applied to investigate the central AGN contribution in addition to two component thermal plasma, i.e.; `phabs` × (`apec` + `apec` + `apec`). The best fitting model to describe the spectra is found to be *Model 3*. The corresponding best-fit values and spectra are given in Table 6.2 and Figure 6.8, respectively.

Table 6.2. Best-fit results of *XMM-Newton* EPIC spectra for r = 10 kpc.

Model 1	**phabs × apec**
kT (keV)	1.32 ±0.02
Z ($Z_\odot$)	1 (fixed)
norm (10^{-5})	$7.67^{+0.45}_{-0.31}$
C-stat / d.o.f.	747.79/189
Model 2	**phabs × (apec + powerlaw)**
kT (keV)	0.98 ±0.03
Z ($Z_\odot$)	1 (fixed)
norm (10^{-5})	$2.38^{+0.18}_{-0.14}$
Γ	$1.81\ ^{+0.05}_{-0.09}$
$\boldsymbol{\kappa}$ (10^{-5})	$2.28^{+0.12}_{-0.17}$
C-stat / d.o.f.	239.80/187
Model 3	**phabs × (apec + apec + powerlaw)**
kT (keV)	$0.84^{+0.08}_{-0.05}$
Z ($Z_\odot$)	1 (fixed)
norm (10^{-5})	$1.64^{+0.12}_{-0.13}$
Γ	$1.62^{+0.29}_{-0.26}$
$\boldsymbol{\kappa}$ (10^{-5})	$0.88^{+0.43}_{-0.34}$
$\mathbf{kT_2}$ (keV)	$2.37^{+0.79}_{-0.37}$
$\mathbf{Z_2}$ ($Z_\odot$)	1 (fixed)
norm (10^{-5})	$5.39^{+1.19}_{-1.43}$
C-stat / d.o.f.	204.59/185

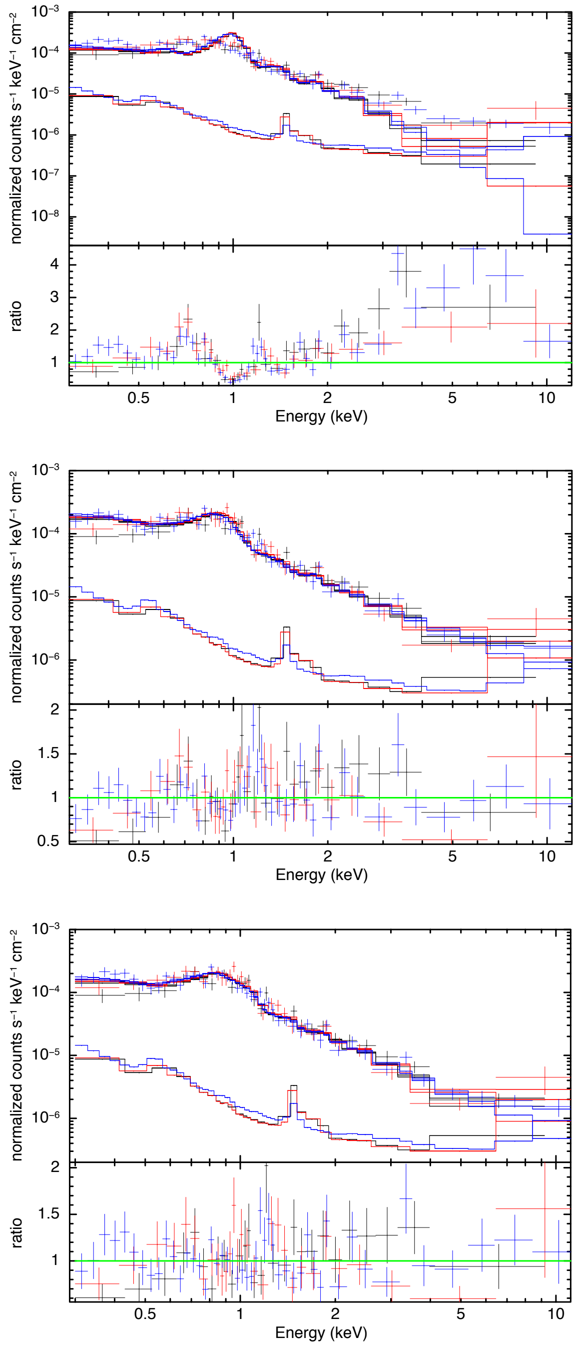

Figure 6.8. *XMM-Newton* spectral fitting of circular 10 kpc region centered at NGC 5718 with *Model 1* (*top*), *Model 2* (*middle*) and *Model 3* (*bottom*). For plotting purposes only, adjacent bins are grouped until they have a significant detection at least as large as 4σ, with maximum 10 bins.

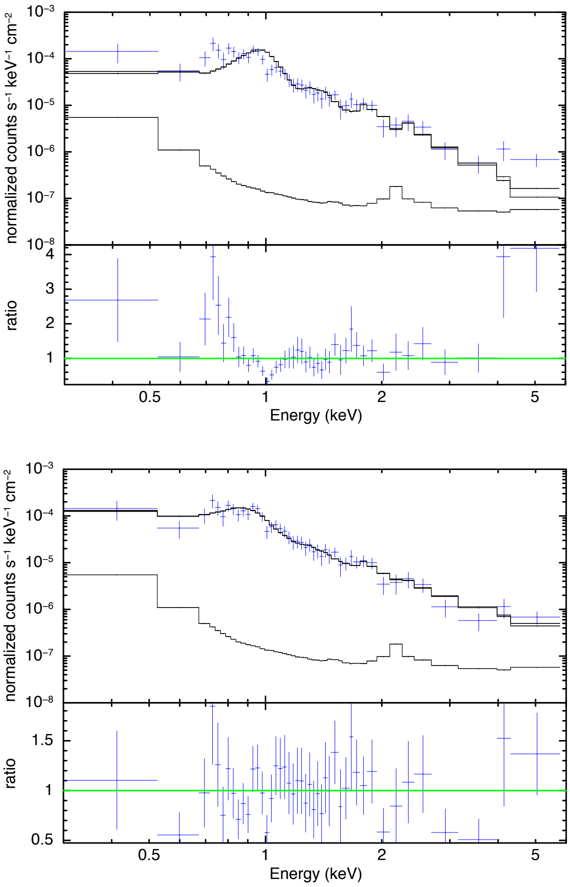

Figure 6.9. *Chandra* spectral fitting of $r = 3$ kpc circular region centered at NGC 5718 with *Model 1* (*upper panel*) and *Model 2* (*lower panel*). For plotting purposes only, adjacent bins are combined until they have a significant detection at least as large as 2σ, with maximum 5 bins.

6.2.2. *Chandra* ACIS-I spectral fitting

For the spectral analysis of the *Chandra* observations, a $r = 3$ kpc ($\approx$5) circular region centered at NGC 5718 is selected, which has 515 net photon counts. The same application of spectral models as described in Section 6.2.1 is followed. However, within $r = 3$ kpc, the second temperature model did not improve the fit which suggests that at this region, the X-ray emission is dominated by the coronal gas, and ICM contribution is negligible. The corresponding best-fit values and spectra are given in Table 6.3 and Figure 6.9, respectively.

Table 6.3. Best-fit results of *Chandra* ACIS-I spectrum for $r = 3$ kpc.

Model 1	**phabs × apec**
kT (keV)	$1.21\ ^{+0.04}_{-0.06}$
Z ($Z_\odot$)	1 (fixed)
norm (10^{-5})	$3.25^{+0.12}_{-0.17}$
C-stat / d.o.f.	111.70/44
Model 2	**phabs × (apec + powerlaw)**
kT (keV)	$0.91^{+0.08}_{-0.09}$
Z ($Z_\odot$)	1 (fixed)
norm (10^{-5})	$1.51^{+0.20}_{-0.21}$
$\boldsymbol{\Gamma}$	$2.49^{+0.26}_{-0.34}$
$\boldsymbol{\kappa}$ (10^{-5})	$1.13^{+0.25}_{-0.22}$
C-stat / d.o.f.	39.60/42

6.2.3. Luminosity

The luminosity of an emission component is found by using the model `phabs` × (`clumin` × `apec` + `clumin` × `powerlaw`), where the normalizations of `apec` and `powerlaw` to a nonzero value, and the normalizations of `clumin` are freed to vary. The luminosity ratio by selecting a new circular region with $0 \leqslant r \leqslant 3$ kpc. Total luminosity of the $r \leqslant 3$ kpc region in the energy band 0.5 - 2.5 keV is found to be $L_X = 1.07^{+0.12}_{-0.13} \times 10^{41}$ erg s^{-1}, where the power-law component is $L_X = 3.04^{+0.75}_{-0.79} \times 10^{40}$ erg s^{-1}. We conclude that power-law accounts for ~30% of the total luminosity in the central region up to $r \simeq 3$ kpc.

6.2.4. Cooling time profile

An order of magnitude estimation of the cooling time is performed at $r = 3$ kpc centered at NGC 5718 with the *Chandra* data using the procedure proposed by Tombesi *et al.* (2017) [118]. The normalization of the *XSPEC* model `apec` emission

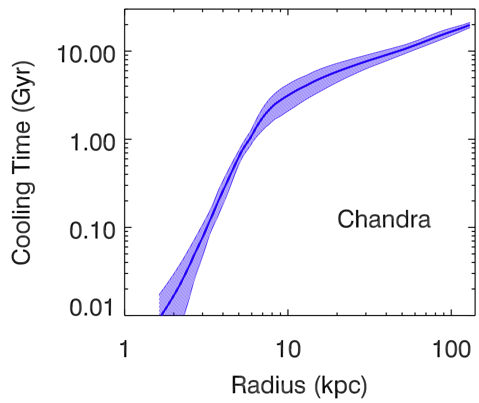

Figure 6.10. Cooling time profile of MKW 08 obtained from *Chandra* data.

measure (EM) is used as described in Chapter 2. The EM is found to be $\simeq 2.38^{+0.31}_{-0.33} \times 10^{63}$ cm^{-3}, and by using the assumption of a fully ionized plasma ($n_e \simeq 1.2\ n_H$) within a spherical volume with $r \simeq 3$ kpc, a density of $n_H \sim 0.02$ cm^{-3} is found..

Following the method described by Peterson *et al.* (2006) [19], we estimated the cooling time in the following steps. The X-ray luminosity of the coronal gas within r = 3 kpc in the 0.3 - 10 keV energy band of the `apec` model was found to be $L_{hot} \simeq 1.07 \times 10^{41}$ erg s^{-1} as described in Section 6.2.3. Changing the energy band from 0.5 - 2.5 keV to 0.3 - 10 keV did not significantly affect the luminosity. The cooling time of this hot gas of a galaxy can be estimated as $t_{cool} = U \ / \ L_{hot}$ where $U = (5/2)\ NkT$ is the internal energy of the gas. Estimating the number of particles, N, from the gas density and volume, we calculated $U \simeq 2.12 \times 10^{56}$ erg for $kT \simeq 1$ keV gas at $T \simeq 10^7$ K. Then, cooling time at $r = 3$ kpc was found to be ~ 64 Myr. By applying this set of calculations using the parameter values obtained from our density and 3-dimensional temperature profiles, we obtained the cooling time curve for *Chandra*, corresponding to each radial element up to $r \simeq 130$ kpc as shown in Figure 6.10.

6.3. Spectroscopic properties of the ∼40 kpc tail

From the *Chandra* surface brightness map given in Figure 6.2, the presence a 40 kpc tail is seen. In literature, these tails are reported to be very scarce, therefore a detailed spectroscopic analysis of region is implemented by choosing two sectors,

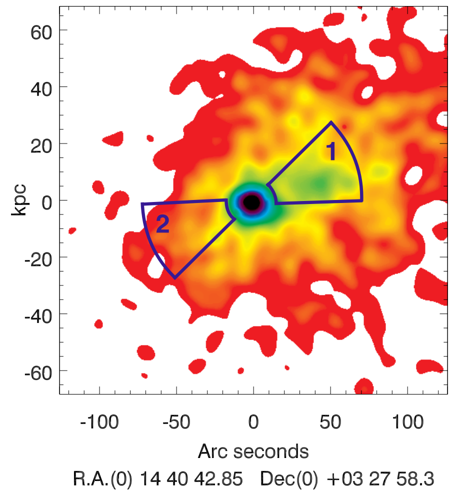

Figure 6.11. Sectors selected from *Chandra* observations outlined on surface brightness map.

Table 6.4. Best-fit results of *Chandra* and *XMM-Newton* spectra for Sector 1 and Sector 2.

Sector 1	**Chandra**	**XMM-Newton**
kT (keV)	$4.65\ ^{+0.39}_{-0.36}$	$3.62\ \pm0.23$
Z ($Z_\odot$)	$0.90^{+0.35}_{-0.22}$	$0.49^{+0.13}_{-0.11}$
$norm$ (10^{-4})	$1.30^{+0.08}_{-0.11}$	1.48 ± 0.08
C / ν	61.69/87	205.18/198
$Luminosity$ ($10^{41} ergs^{-1}$)	1.68 ± 0.05	1.76 ± 0.08
Sector 2	**Chandra**	**XMM-Newton**
kT (keV)	$4.09^{+0.48}_{-0.43}$	$2.90^{+0.26}_{-0.28}$
Z ($Z_\odot$)	$0.22\ ^{+0.19}_{-0.16}$	$0.20\ ^{+0.10}_{-0.09}$
$norm$ (10^{-4})	$1.06^{+0.07}_{-0.08}$	0.90 ± 0.07
C / ν	39.60/42	155.45/163
$Luminosity$ ($10^{41} ergs^{-1}$)	1.16 ± 0.05	0.96 ± 0.06

which are symmetric along the true northeat-southwest axis. Figure 6.11 describes the selection of these regions. While the region Sector 1 encloses the tail region, Sector 2 is not associated with this feature. By means of spectral analysis, the spectroscopic parameters are analyzed with both *Chandra* and *XMM-Newton* in order to investigate which parameters of this tail differs from the spectra of the Sector 2, namely; the region of the ICM emission. These sectors have an inner radius of 10 kpc and an outer radius of 40 kpc, which cover a 45 degree angle. Sector 1 selected from *Chandra* contains 1570 net photon counts , whereas Sector 2 contains 985 net photon counts. The *XMM-Newton* net photon counts for Sector 1 is 547 (MOS1), 468 (MOS2), 1278 (PN), while Sector 2 contains 357 (MOS1), 333 (MOS2), 820 (PN) net photon counts. Even prior to a spectral analysis, the difference in the photon count emissions points to an flux much different from that of the ICM in a region with the same area. The model `phabs` $\times$ `apec` is applied to both sectors, and to both data sets as well as a luminosity calculation using the model `phabs` $\times$ (`clumin` $\times$ `apec`). The corresponding spectra and parameters are presented in Figure 6.12 and Table 6.4, respectively.

Although temperature values of Sector 1 and Sector 2 agree within 2σ errors, both the spectral fit and parameter values show that the NGC 5718 tail (Sector 1) encloses a medium with high luminosity and abundance with respect to Sector 2, while the *XMM-Newton* spectral analysis results provide a better constrained abundance values.

6.4. Discussion

Three characteristic regions of the corona ($r \leqslant 4$ kpc), the corona - ICM interface ($4 \leqslant r \leqslant 10$ kpc) and the ICM (10 kpc $\leqslant r$) are revealed from the temperature and pressure profiles of the *Chandra* data. The temperature, characteristic scale, luminosity are in well agreement with the literature [81]. In addition, contrary to what is previously reported in literature [45], the isothermal nature of these corona is reported for the first time to the author's best knowledge provided by a detailed imaging and spectroscopic analysis of the high spatial resolution and deep exposure time of the data. The hot ISM in BCG coronae seems to survive ICM stripping, since otherwise a pure ICM cooling would have resulted in large scale smooth cooling profile instead of strong gradients

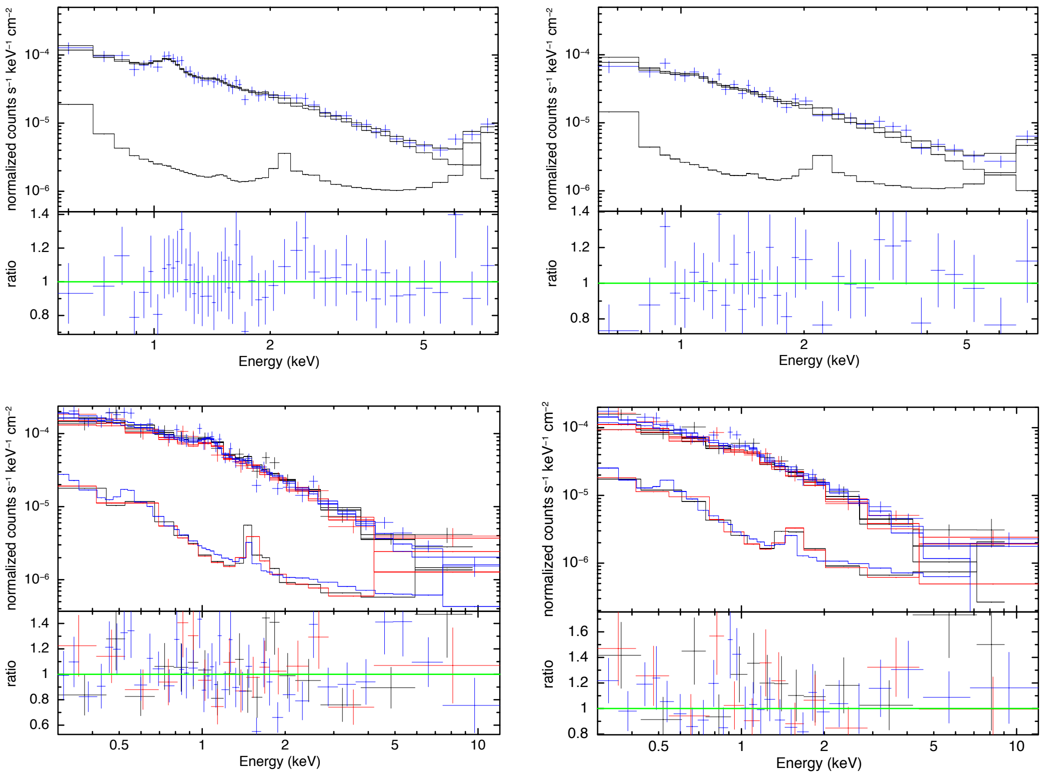

Figure 6.12. *Chandra* (*upper panel*) and *XMM-Newton* (*lower panel*) spectral fitting of Sector 1 (*left panel*) and Sector 2 (*right panel*) with `phabs` $\times$ `apec` models. For plotting purposes only, adjacent bins are combined until they have a significant detection at least as large as 5σ, with maximum 10 bins.

enclosed by $r \sim 4$ kpc [119]

In both *XMM-Newton* and *Chandra* spectral analysis, a prominent power-law emission is found with photon indices of $\Gamma = 1.81^{+0.05}_{-0.09}$ and $\Gamma = 2.49^{+0.26}_{-0.34}$ for *XMM-Newton* and *Chandra*, respectively. This finding suggests the existence of an AGN along with the findings of Hogan *et al.* (2015) [120] who find evidence for radio activity of this BCG, and of Bharadwaj *et al.* (2014) [117] who point to the central radio source in MKW 08.

The cooling time value of ~ 60 Myr is reported for this cluster at $r = 3$ kpc, although MKW 08 was classified as a NCC by its large central cooling time at $r = 0.4\%$ R_{500} [31]. The investigation of a smaller region in this work compared with the literature gave rise to the understanding that mini cool core can be easily missed when an average of a large central bin is used. This cooling time is 3 orders of magnitude smaller than the Hubble time, therefore a heating mechanism is needed to keep the ISM hot. The possible heating mechanisms are AGN heating, heat conduction from the ICM, and star formation. The star formation heats the gas mostly through stellar winds and shocks from supernova [121]. The X-ray luminosity and star formation relation, i.e., $L_{X(0.5-8.0keV)} \simeq 4 \times 10^{39}$ $(\dot{M}_*/M_\odot yr^{-1})$ [122], allows the estimation of star formation rate. Using the luminosity value found in Section 6.2.3, a star formation rate of $\dot{M}_* \sim 40$ $M_\odot$ yr^{-1} is estimated. However, this value is quite large compared to the rate expected from radio galaxies [118, 123], therefore will not be adequate to suppress the cooling. Since the gas is isothermal inside $r = 3$ kpc is fount to be isothermal, therefore heat conduction does not play a role.

A hot ISM with a temperature of $kT \sim 1$ keV located within ~ 4 kpc of the AGN is recently reported also in the *Chandra* grating spectra of two bright radio galaxies, namely 3C 390.3 and 3C 120 [118, 124]. These radio galaxies show evidence of both powerful wind and jets, and it is suggested that their mechanical power may be enough to provide a heating source for the hot ISM [118]. Theories of AGN feedback driven by winds or jets predicts the existence of hot shocked bubbles [125–127]. The forward shock decelerates while the AGN wind sweeps up the ambient medium, resulting in a cooler gas with a temperature of T $\sim 10^7$ K for a shock velocity of $\sim$ 1000 km s^{-1}. Depending on the power of the central AGN, the X-ray luminosity of the thermal bremsstrahlung expected from wind-shocked gas is $L_X \sim 10^{41}$-10^{42} erg s^{-1} [128, 129]. These parameters are overall consistent with estimates for the hot X-ray-emitting gas in the central 3 kpc region of NGC 5718.

The scarcity of the X-ray tails are discussed for a sample of 76 early-type galaxy coronae including NGC 5718, where no tail-like structure was reported for the cluster [81]. This work suggests that these structures may not be as rare as expected (5%), but may be missed by data with low resolution and/or short exposure time. The high abundance value ($Z \simeq 0.9\ Z_\odot$ of this tail found by the spectral analysis suggests that this structure might have been formed by the stripped material from the BCG, or is a result of an interaction process between NGC 5718 and IC 1042.

7. CONCLUSION

In this work, a combined spectroscopic and imaging study of a sample of NCC galaxy clusters and their BCGs using archival *XMM-Newton* EPIC observations is presented.

The galaxy cluster Abell 1656 and MKW 08 host a BCG corona as reported by Sun *et al.* [81]. In this work, it is found that these corona are isothermal contrary to what is suggested by the literature [81], where the most possible mechanism to sustain the heating of these central regions is the AGN feedback and thermal conduction does not play an important role at small scales.

A a chemically rich, ~ 40 kpc X-ray tail is discovered in this work, which originates from the BCG of MKW 08, namely; NGC 5718. Previously, these tails were redeemed very scarce in clusters of galaxies. Sun *et al.* (2007) reported an X-ray tail fraction of 5% of their population of 76 early-type galaxy coronae [81]. With high spatial resolution and deep observations combined with spectroscopic and imaging studies, it is possible that these structure are common in clusters.

The analysis results of ZwCl 1215 provided that the cluster BCG is a good corona candidate, showing typical coronal features [81] at $r = 10$ kpc. However, a deep *Chandra* observation is required to test this hypothesis given the redshift of the cluster, where *XMM-Newton* PSF prevented a higher spatial resolution study of the central region. This work also includes the first detailed study of ZwCl 1215.

MKW 08 shows very rapid cooling in the central region $r = 3$ kpc. However, it was reported as an NCC cluster due to its long cooling time (~ 10 Gyr) at $r = 0.4\%$ R_{500} [31]. The central cooling time parameter, which is used to describe a dichotomy between NCC and CC types of clusters, may not be the best approach to segregate clusters of galaxies unless the central region behavior is studied in depth for a complete sample.

AGN in non-cool core clusters are mostly preserved yet significant at smaller radii in contrast with cool core types of cluster. These findings are in line with the scenario that non-cool core clusters are most probably dynamically young objects and during their evolution they become cool core clusters once the cluster becomes relaxed and more accretion of material onto the central SMBH is achieved.

A combined spectroscopic and imaging method is introduced and applied to the study of a sample of NCC clusters in this work. This work suggests that high spectral and spatial resolution is required to improve the understanding of the evolution of BCGs, the influence of the AGN and their interaction with their host clusters. The methodology adopted in this work, will therefore have important implications with future missions such as *XRISM* [130], *Lynx* [131], *AXIS* [132] and *Athena* [133].

REFERENCES

1. Navarro, J. F., C. S. Frenk and S. D. M. White, "Simulations of X-ray Clusters", *Monthly Notices of the Royal Astronomical Society*, Vol. 275, pp. 720–740, 1995.

2. Moore, B., S. Ghigna, F. Governato, G. Lake, T. Quinn, J. Stadel and P. Tozzi, "Dark Matter Substructure in Galactic Halos", *The Astrophysical Journal*, Vol. 524, pp. 19–22, 1999.

3. Gao, L., J. F. Navarro, S. Cole, C. Frenk, S. D. M. White, V. Springel, A. Jenkins and A. F. Neto, "The redshift dependence of the structure of massive LCDM halos", *Monthly Notices of the Royal Astronomical Society*, Vol. 387, p. 536, 2008.

4. Hattori, M., J. Kneib and N. Makino, "Gravitational Lensing in Clusters of Galaxies", *Progress of Theoretical Physics Supplement*, Vol. 113, pp. 1–51, 1999.

5. Birkinshaw, M., "The Sunyaev-Zel'dovich effect", *Physics Reports*, Vol. 310, p. 97, 1999.

6. Willson, M. A. G., "Radio observations of the cluster of galaxies in Coma Berenice", *Monthly Notices of the Royal Astronomical Society*, Vol. 151, p. 1, 1970.

7. Abell, G. O., "The Distribution of Rich Clusters of Galaxies.", *Astrophysical Journal Supplements*, Vol. 3, p. 211, 1958.

8. Zwicky, F., "How Far Do Cosmic Rays Travel?", *Physical Review*, Vol. 43, No. 147, 1933.

9. Byram, E. T. and Chubb, T. A. and Friedman, H., "Cosmic X-ray Sources, Galactic and Extragalactic", *Science*, Vol. 152, pp. 66–71, 1966.

10. Bradt, H. and Mayer, W. and Naranan, S. and Rappaport, S. and Spada, G., "Evidence for X-Radiation from the Radio Galaxy M87", *Astrophysical Journal Letters*, Vol. 150, p. 199, 1967.

11. Giacconi, R., S. Murray, H. Gursky, E. Kellogg, E. Schreier and H. Tananbaum, "The Uhuru catalog of X-ray sources", *Astrophysical Journal*, Vol. 178, pp. 281–308, 1972.

12. Mitchell, R. J. and Culhane, J. L. and Davison, P. J. N. and Ives, J. C., "Ariel 5 observations of the X-ray spectrum of the Perseus Cluster", *Monthly Notices of the Royal Astronomical Society*, Vol. 175, p. 29, 1976.

13. Serlemitsos, P. J. and Smith, B. W. and Boldt, E. A. and Holt, S. S. and Swank, J. H., "X-radiation from clusters of galaxies - Spectral evidence for a hot evolved gas", *Astrophysical Journal Letters*, Vol. 211, p. 63, 1977.

14. Mushotzky, R. F. and Boldt, E. A. and Holt, S. S. and Rothschild, R. and Serlemitsos, P. J., "HEAO-1 Observations of Compact Extragalactic X-Ray Sources", *Bulletin of the American Astronomical Society*, Vol. 10, p. 503, 1978.

15. Mushotzky, R. F., "X-ray spectra of clusters of galaxies", *NASA STI/Recon Technical Report N*, Vol. 84, 1984.

16. Bahcall, J. N. and Sarazin, C. L., "Parameters and predictions for the X-ray emitting gas of Coma, Perseus, and Virgo", *Astrophysical Journal Letters*, Vol. 213, pp. L99–L103, 1977.

17. Boehringer, H. and N. Werner, "X-ray Spectroscopy of Galaxy Clusters: Studying astrophysical processes in the largest celestial laboratories", *Astronomy and Astrophysics Review*, Vol. 18, No. 1, pp. 127–196, 2009.

18. Kalberla, P. M. W., W. B. Burton, D. Hartmann, E. M. Arnal, E. Bajaja, R. Morras and W. G. L. Poppel, "The Leiden/Argentine/Bonn (LAB) Survey of Galactic

HI: Final data release of the combined LDS and IAR surveys with improved stray-radiation corrections", *Astronomy and Astrophysics*, Vol. 440, p. 775, 2005.

19. Peterson, J. R. and A. C. Fabian, "X-ray Spectroscopy of Cooling Clusters", *Phys.Rept.*, Vol. 427, pp. 1–39, 2006.

20. Fabian, A. C. and Nulsen, P. E. J., "Subsonic accretion of cooling gas in clusters of galaxies", *Monthly Notices of the Royal Astronomical Society*, Vol. 180, p. 479, 1977.

21. Mathews, W. G., "The enormous mass of the elliptical galaxy M87 - A model for the extended X-ray source", *Astrophysical Journal*, Vol. 219, p. 413, 1978.

22. Fabian, A. C., "Cooling flows in clusters of galaxies", *Annual Review of Astronomy and Astrophysics*, Vol. 32, pp. 277–318, 1994.

23. Tamura, T., J. A. M. Bleeker, J. S. Kaastra, C. Ferrigno and S. Molendi, "XMM-Newton observations of the cluster of galaxies Abell496 -Measurements of the elemental abundances in the intracluster medium-", *Astronomy and Astrophysics*, Vol. 379, pp. 107–114, 2001.

24. Peterson, J. R., F. B. S. Paerels, J. S. Kaastra, M. Arnaud, T. H. Reiprich, A. C. Fabian, R. F. Mushotzky, J. G. Jernigan and I. Sakelliou, "X-ray Imaging Spectroscopy of Abell 1835", *Astronomy and Astrophysics*, Vol. 365, pp. 104–109, 2001.

25. Kaastra, J. S., C. Ferrigno, T. Tamura, F. B. S. Paerels, J. R. Peterson and J. P. D. Mittaz, "XMM-Newton observations of the cluster of galaxies Sersic 159-03", *Astronomy and Astrophysics*, Vol. 365, No. 99-103, 2001.

26. Xu, H., S. M. Kahn, J. R. Peterson, E. Behar, F. B. S. Paerels, R. F. Mushotzky, J. G. Jernigan and K. Makishima, "High Resolution Observations of the Elliptical Galaxy NGC 4636 with the Reflection Grating Spectrometer On-Board XMM-

Newton", *Astrophysical Journal*, Vol. 579, pp. 600–606, 2002.

27. Sakelliou, I., J. R. Peterson, T. Tamura, F. B. S. Paerels, J. S. Kaastra, E. Belsole, H. Boehringer, G. Branduardi-Raymont, C. Ferrigno, J. W. den Herder, J. Kennea, R. F. Mushotzky, W. T. Vestrand and D. M. Worrall, "High Resolution Soft X-ray Spectroscopy of M87 with the Reflection Grating Spectrometers on XMM-Newton", *Astronomy and Astrophysics*, Vol. 391, p. 903, 2002.

28. Peterson, J. R., S. M. Kahn, F. B. S. Paerels, J. S. Kaastra, T. Tamura, J. A. M. Bleeker, C. Ferrigno and J. G. Jernigan, "High Resolution X-ray Spectroscopic Constraints on Cooling-Flow Models", *Astrophysical Journal*, Vol. 590, p. 207, 2003.

29. Sanders, J. S., A. C. Fabian, S. W. Allen, R. G. Morris, J. Graham and R. M. Johnstone, "Cool X-ray emitting gas in the core of the Centaurus cluster of galaxies", *Monthly Notices of the Royal Astronomical Society*, Vol. 385, pp. 1186–1200, 2008.

30. Edge, A. C. and Frayer, D. T., "Resolving Molecular gas in the Central Galaxies of Cooling Flow Clusters", *Astrophysical Journal Letters*, Vol. 594, p. 13, 2003.

31. Hudson, D. S., R. Mittal, T. H. Reiprich, P. E. J. Nulsen, H. Andernach and C. L. Sarazin, "What is a Cool-Core Cluster? A Detailed Analysis of the Cores of the X-ray Flux-Limited HIFLUGCS Cluster Sample", *Astronomy and Astrophysics*, Vol. 513, p. A37, 4 2010.

32. Molendi, S. and F. Pizzolato, "Is the Gas in Cooling Flows Multiphase?", *The Astrophysical Journal*, Vol. 560, No. 1, p. 194, 2001.

33. Sanderson, A. J. R., T. J. Ponman and E. O'Sullivan, "A statistically-selected Chandra sample of 20 galaxy clusters – I. Temperature and cooling time profiles", *Monthly Notices of the Royal Astronomical Society*, Vol. 372, p. 1496, 2006.

34. Burns, J. O., E. J. Hallman, B. Gantner, P. M. Motl and M. L. Norman, "Why Do Only Some Galaxy Clusters Have Cool Cores?", *Astrophysical Journal*, Vol. 675, p. 1125, 2008.

35. Bauer, A. E., N. Drory, G. J. Hill and G. Feulner, "Specific Star Formation Rates to Redshift 1.5", *Astrophysical Journal*, Vol. 621, p. 89, 2005.

36. O'Hara, T. B., J. J. Mohr, J. J. Bialek and A. E. Evrard, "Effects of Mergers and Core Structure on the Bulk Properties of Nearby Galaxy Clusters", *Astrophysical Journal*, Vol. 639, p. 64, 2006.

37. Chen, L., R. de Grijs and J. L. Zhao, "Mass segregation in very young open clusters – A case study of NGC 2244 and NGC 6530", *Astronomical Journal*, Vol. 134, p. 1368, 2007.

38. Reiprich, T. H. and H. Böhringer, "The Mass Function of an X-Ray Flux-Limited Sample of Galaxy Clusters", *Astrophysical Journal*, Vol. 567, pp. 716–740, 2002.

39. Mittal, R., D. S. Hudson, T. H. Reiprich and T. Clarke, "AGN heating and ICM cooling in the HIFLUGCS sample of galaxy clusters", *Astronomy and Astrophysics*, Vol. 501, pp. 835–850, 2009.

40. Cavagnolo, K. W., M. Donahue, G. M. Voit and M. Sun, "Intracluster Medium Entropy Profiles for a Chandra Archival Sample of Galaxy Clusters", *Astrophysical Journal Supplements*, Vol. 182, p. 12, 2009.

41. Poole, G. B., A. Babul, I. G. McCarthy, A. J. R. Sanderson and M. A. Fardal, "The impact of mergers on relaxed X-ray clusters - III. Effects on compact cool cores", *Monthly Notices of the Royal Astronomical Society*, Vol. 391, p. 1163, 2008.

42. McCarthy, I. G., A. Babul, R. G. Bower and M. L. Balogh, "Towards a Holistic View of the Heating and Cooling of the Intracluster Medium", *Monthly Notices*

of the Royal Astronomical Society, Vol. 386, p. 1309, 2008.

43. Rossetti, M. and S. Molendi, "Cool core remnants in galaxy clusters", *Astronomy and Astrophysics*, Vol. 510, p. 83, 2010.

44. Pratt, G. W., M. Arnaud, R. Piffaretti, H. Boehringer, T. J. Ponman, J. H. Croston, G. M. Voit, S. Borgani and R. G. Bower, "Gas entropy in a representative sample of nearby X-ray galaxy clusters (REXCESS): relationship to gas mass fraction", *Astronomy and Astrophysics*, Vol. 511, p. 85, 2010.

45. Sun, M., "Every BCG with a strong radio AGN has an X-ray cool core: is the cool core - noncool core dichotomy too simple?", *Astrophysical Journal*, Vol. 704, pp. 1586–1604, 2009.

46. Mathews, W. G. and F. Brighenti, "Hot Gas In and Around Elliptical Galaxies", *Annual Review of Astronomy and Astrophysics*, Vol. 41, pp. 191–239, 2003.

47. Voigt, L. M. and A. C. Fabian, "Thermal conduction and reduced cooling flows in galaxy clusters", *Monthly Notices of the Royal Astronomical Society*, Vol. 347, p. 1130, 2004.

48. Churazov, E., R. Sunyaev, W. Forman and H. Boehringer, "Cooling Flows as a Calorimeter of AGN Mechanical Power", *Monthly Notices of the Royal Astronomical Society*, Vol. 332, p. 729, 2002.

49. Roychowdhury, S., M. Ruszkowski, B. B. Nath and M. C. Begelman, "Entropy "floor" and effervescent heating of intracluster gas", *The Astrophysical Journal*, Vol. 615, pp. 681–688, 2004.

50. Voit, G. M. and M. Donahue, "An Observationally Motivated Framework for AGN Heating of Cluster Cores", *The Astrophysical Journal*, Vol. 634, pp. 955–963, 2005.

51. Padovani, P., D. M. Alexander, R. J. Assef, B. D. Marco, P. Giommi, R. C. Hickox, G. T. Richards, V. Smolcic, E. Hatziminaoglou, V. Mainieri and M. Salvato, "Active Galactic Nuclei: what's in a name?", *Astronomy and Astrophysics Review*, Vol. 25, p. 2, 2017.

52. Fabian, A. C., "Observational Evidence of Active Galactic Nuclei Feedback", *Annual Review of Astronomy and Astrophysics*, Vol. 50, p. 455, 2012.

53. Gaspari, M., F. Brighenti, P. Temi and S. Ettori, "Can AGN Feedback Break the Self-similarity of Galaxies, Groups, and Clusters?", *Astrophysical Journal Letters*, Vol. 783, p. L10, 3 2014.

54. Risaliti, G. and M. Elvis, "A panchromatic view of AGN", Barger, A. J. (Editor), *Supermassive Black Holes in the Distant Universe*, Vol. 308, p. 187, 2004.

55. Nandra, K. and Pounds, K. A., "GINGA Observations of the X-Ray Spectra of Seyfert Galaxies", *Monthly Notices of the Royal Astronomical Society*, Vol. 268, p. 405, 1994.

56. Reeves, J. and M. Turner, "X-ray Spectra of a large sample of Quasars with ASCA", *Monthly Notices of the Royal Astronomical Society*, Vol. 316, p. 234, 2000.

57. Piconcelli, E., E. Jimenez-Bailon, M. Guainazzi, N. Schartel, P. M. Rodriguez-Pascual and M. Santos-Lleo, "The XMM-Newton view of PG quasars I. X-ray continuum and absorption", *Astronomy and Astrophysics*, Vol. 432, pp. 15–30, 2005.

58. Gaspari, M. and A. Sadowski, "Unifying the micro and macro properties of AGN feeding and feedback", *Astrophysical Journal*, Vol. 837, p. 149, 3 2017.

59. Tombesi, F., M. Melendez, S. Veilleux, J. N. Reeves, E. Gonzalez-Alfonso and C. S. Reynolds, "Wind from the black-hole accretion disk driving a molecular

outflow in an active galaxy", *Nature*, Vol. 519, p. 436, 2015.

60. Cicone, C., M. Brusa, C. R. Almeida, G. Cresci, B. Husemann and V. Mainieri, "The largely unconstrained multiphase nature of outflows in AGN host galaxies", *Nature Astronomy*, Vol. 2, pp. 176–178, 2018.

61. Jones, C., W. Forman, A. Vikhlinin, M. Markevitch, L. David, A. Warmflash, S. Murray and P. E. J. Nulsen, "Chandra Observations of NGC 4636 - An Elliptical Galaxy in Turmoil", *The Astrophysical Journal*, Vol. 576, p. L115, 2002.

62. Fabian, A. C., J. S. Sanders, S. W. Allen, C. S. Crawford, K. Iwasawa, R. M. Johnstone, R. W. Schmidt and G. B. Taylor, "A deep Chandra observation of the Perseus cluster: shocks and ripples", *MRNAS*, Vol. 344, p. L43, 2003.

63. Mathews, W. G., F. Brighenti, A. Faltenbacher, D. A. Buote, P. J. Humphrey, F. Gastaldello and L. Zappacosta, "Large scatter in X-ray emission among elliptical galaxies: correlations with mass of host halo", *The Astrophysical Journal*, Vol. 652, pp. L17–L20, 2006.

64. Birzan, L., D. A. Rafferty, B. R. McNamara, M. W. Wise and P. E. J. Nulsen, "A Systematic Study of Radio-Induced X-ray Cavities in Clusters, Groups, and Galaxies", *Astrophysical Journal Letters*, Vol. 607, pp. 800–809, 2004.

65. McNamara, B. R., P. E. J. Nulsen, M. W. Wise, D. A. Rafferty, C. Carilli, C. L. Sarazin and E. L. Blanton, "Heating a Distant Galaxy Cluster by Giant X-ray Cavities and Large-Scale Shock Fronts", *Nature*, Vol. 433, p. 45, 2005.

66. Nulsen, P. E. J., B. R. McNamara, M. W. Wise and L. P. David, "The cluster-scale AGN outburst in Hydra A", *Astrophysical Journal Letters*, Vol. 628, pp. 629–636, 2005.

67. Sadowski, A. and M. Gaspari, "Kinetic and radiative power from optically thin accretion flows", *Monthly Notices of the Royal Astronomical Society*, Vol. 468,

pp. 1398–1404, 2017.

68. Lin, Y.-T. and J. J. Mohr, "Radio Sources in Galaxy Clusters: Radial Distribution, and 1.4 GHz and K-band Bivariate Luminosity Function", *Astrophysical Journal Supplements*, Vol. 170, p. 71, 2007.

69. McDonald, M., M. Gaspari, B. R. McNamara and G. R. Tremblay, "Revisiting the Cooling Flow Problem in Galaxies, Groups, and Clusters of Galaxies", *Astrophysical Journal*, Vol. 858, p. 45, 2018.

70. Best, P. N., A. von der Linden, G. Kauffmann, T. M. Heckman and C. R. Kaiser, "On the prevalence of radio-loud active galactic nuclei in brightest cluster galaxies: implications for AGN heating of cooling flows", *Monthly Notices of the Royal Astronomical Society*, Vol. 349, p. 894, 2017.

71. von der Linden, A., P. N. Best, G. Kauffmann and S. D. M. White, "How special are Brightest Group and Cluster Galaxies?", *Monthly Notices of the Royal Astronomical Society*, Vol. 379, pp. 867–893, 2007.

72. Roettiger, K. and Loken, C. and Burns, J. O., "Numerical Simulations of Merging Clusters of Galaxies", *Astrophysical Journal Supplements*, Vol. 109, p. 307, 1997.

73. Ascasibar, Y. and M. Markevitch, "The origin of cold fronts in the cores of relaxed galaxy clusters", *Astrophysical Journal*, Vol. 650, pp. 102–127, 2006.

74. Poole, G. B., A. Babul, I. G. McCarthy, A. J. R. Sanderson and M. A. Fardal, "The impact of mergers on relaxed X-ray clusters - III. Effects on compact cool cores", *Monthly Notices of the Royal Astronomical Society*, Vol. 373, p. 881, 2006.

75. Wang, Y., H. Xu, L. Gu, J. Gu, Z. Qin, J. Wang, Z. Zhang and X.-P. Wu, "A Joint Chandra and XMM-Newton View of Abell 3158: Massive Off-Centre Cool Gas Clump As A Robust Diagnostic of Merger Stage", *Monthly Notices of the Royal Astronomical Society*, Vol. 403, p. 1909, 2010.

76. Laganá, T. F., F. Durret and P. A. A. Lopes, "Physical properties of the X-ray gas as a dynamical diagnosis for galaxy clusters", *Monthly Notices of the Royal Astronomical Society*, Vol. 484, pp. 2807–2830, 2019.

77. Arnaud, M. and R. Rothenflug, "An updated evaluation of recombination and ionization rates", *Astronomy and Astrophysics Supplement Series*, Vol. 60, No. 425-457, 1985.

78. Arnaud, M., R. Rothenflug, O. Boulade, L. Vigroux and E. Vangioni-Flam, "Some Constraints on the Origin of the Iron Enriched Intracluster Medium", *Astronomy and Astrophysics*, Vol. 254, No. 49, 1992.

79. Mazzotta, P., G. Mazzitelli, S. Colafrancesco and N. Vittorio, "Ionization balance for optically thin plasmas: rate coefficients for all atoms and ions of the elements H to Ni", *Astronomy and Astrophysics Supplement Series*, Vol. 133, p. 403, 1998.

80. Gronenschild, E. H. B. M. and R. Mewe, "Calculated X-radiation from optically thin plasmas. III - Abundance effects on continuum emission", *Astronomy and Astrophysics Supplement Series*, Vol. 32, pp. 283–305, 1978.

81. Sun, M., C. Jones, W. Forman, A. Vikhlinin, M. Donahue and M. Voit, "X-ray thermal coronae of galaxies in hot clusters – ubiquity of embedded mini cooling cores", *Astrophysical Journal*, Vol. 657, pp. 197–231, 2007.

82. Lopes, P. A. A., M. Trevisan, T. F. Laganá, F. Durret, A. L. B. Ribeiro and S. B. Rembold, "Optical Substructure and BCG Offsets of Sunyaev-Zel'dovich and X-ray Selected Galaxy Clusters", *Monthly Notices of the Royal Astronomical Society*, Vol. 478, pp. 5473–5490, 2018.

83. Piffaretti, R., M. Arnaud, G. W. Pratt, E. Pointecouteau and J. B. Melin, "The MCXC: a Meta-Catalogue of X-ray detected Clusters of galaxies", *Astronomy and Astrophysics*, Vol. 534, p. 109, 2011.

84. Willingale, R., R. L. C. Starling, A. P. Beardmore, N. R. Tanvir and P. T. O'Brien, "Calibration of X-ray absorption in our Galaxy", *Monthly Notices of the Royal Astronomical Society*, Vol. 431, pp. 394–404, 2013.

85. Kalberla, P. M. W., W. B. Burton, D. Hartmann, E. M. Arnal, E. Bajaja, R. Morras and W. G. L. Poppel, "The Leiden/Argentine/Bonn (LAB) Survey of Galactic HI: Final data release of the combined LDS and IAR surveys with improved stray-radiation corrections", *Astronomy and Astrophysics*, Vol. 440, pp. 775–782, 2005.

86. ESA: XMM-Newton SOC, *XMM-Newton Users Handbook*, 2019, `http://xmm-tools.cosmos.esa.int/external/xmm_user_support/documentation/uhb/`, accessed in June 2019.

87. Bourdin, H. and P. Mazzotta, "Temperature structure of the intergalactic medium within seven nearby and bright clusters of galaxies observed with XMM-Newton", *Astronomy and Astrophysics*, Vol. 479, pp. 307–320, 2 2008.

88. Kuntz, K. D. and S. L. Snowden, "Deconstructing the Spectrum of the Soft X-Ray Background", *Astrophysical Journal Letters*, Vol. 543, No. 1, p. 195, 2000.

89. Lumb, D. H., R. S. Warwick, M. Page and A. D. Luca, "X-ray background measurements with XMM-Newton EPIC", *Astronomy and Astrophysics*, Vol. 389, No. 1, pp. 93–105, 2002.

90. Read, A. M. and T. J. Ponman, "The XMM-Newton EPIC Background: Production of Background Maps and Event Files", *Astronomy and Astrophysics*, Vol. 409, pp. 395–410, 2003.

91. Bourdin, H., P. Mazzotta, M. Markevitch, S. Giacintucci and G. Brunetti, "Shock heating of the merging galaxy cluster A521", *Astrophysical Journal*, Vol. 764, p. 82, 2 2013.

92. Leccardi, A. and S. Molendi, "Radial temperature profiles for a large sample of

galaxy clusters observed with XMM-Newton*", *Astronomy and Astrophysics*, Vol. 486, No. 2, pp. 359–373, 2008.

93. Starck, J.-L., J. M. Fadili, S. Digel, B. Zhang and J. Chiang, "Source detection using a 3D sparse representation: application to the Fermi gamma-ray space telescope", *Astronomy and Astrophysics*, Vol. 504, pp. 641–652, 9 2009.

94. Smith, R. K., N. S. Brickhouse, D. A. Liedahl and J. C. Raymond, "Collisional Plasma Models with APEC/APED: Emission-Line Diagnostics of Hydrogen-like and Helium-like Ions", *Astrophysical Journal Letters*, Vol. 556, pp. L91–L95, 8 2001.

95. Vikhlinin, A., A. Kravtsov, W. Forman, C. Jones, M. Markevitch, S. S. Murray and L. V. Speybroeck, "Chandra sample of nearby relaxed galaxy clusters: mass, gas fraction, and mass-temperature relation", *Astrophysical Journal*, Vol. 640, pp. 691–709, 2006.

96. Pointecouteau, E., M. Arnaud, Kaastra, J. and de Plaa, J., "XMM-Newton observation of the relaxed cluster A478", *Astronomy and Astrophysics*, Vol. 423, No. 1, pp. 33–47, 2004.

97. Cavaliere, A. and R. Fusco-Femiano, "The Distribution of Hot Gas in Clusters of Galaxies", *Astronomy and Astrophysics*, Vol. 70, p. 677, 1978.

98. Mazzotta, P., E. Rasia, L. Moscardini and G. Tormen, "Comparing the temperatures of galaxy clusters from hydrodynamical N-body simulations to Chandra and XMM-Newton observations", *Monthly Notices of the Royal Astronomical Society*, Vol. 354, pp. 10–24, 10 2004.

99. Arnaud, K. A., "XSPEC: The First Ten Years", Jacoby, G. H. and Barnes, J. (Editor), *Astronomical Data Analysis Software and Systems V*, Vol. 101 of *Astronomical Society of the Pacific Conference Series*, p. 17, 1996.

100. Cash, W., “Parameter estimation in astronomy through application of the likelihood ratio”, *Astrophysical Journal*, Vol. 228, pp. 939–947, 1979.

101. UK Swift Science Data Centre, *Calculate Galactic Nh*, 2013, `https://www.swift.ac.uk/analysis/nhtot/`, accessed in June 2019.

102. Sakelliou, I. and T. J. Ponman, “XMM-Newton observations of the binary cluster system Abell 399/401”, *Monthly Notices of the Royal Astronomical Society*, Vol. 351, p. 1439, 2004.

103. Hudson, D. S., T. H. Reiprich, T. E. Clarke and C. L. Sarazin, “X-ray Detection of the Proto Supermassive Binary Black Hole at the Centre of Abell 400”, *Astronomy and Astrophysics*, Vol. 453, p. 433, 2006.

104. Tozzi, P., R. Gilli, V. Mainieri, C. Norman, G. Risaliti, P. Rosati, J. Bergeron, S. Borgani, R. Giacconi, G. Hasinger, M. Nonino, A. Streblyanska, G. Szokoly, J. X. Wang and W. Zheng, “X-ray spectral properties of active galactic nuclei in the Chandra Deep Field South”, *Astronomy and Astrophysics*, Vol. 451, pp. 457–474, 2006.

105. Lokas, E. L., R. Wojtak, S. Gottloeber, G. A. Mamon and F. Prada, “Mass distribution in nearby Abell clusters”, *Monthly Notices of the Royal Astronomical Society*, Vol. 367, p. 1463, 2006.

106. Quintana, H., “Core radii and mass segregation in clusters of galaxies”, *Astronomical Journal*, Vol. 84, p. 15, 1979.

107. Sérsic, J. L., “A list of peculiar galaxies, interacting pairs, groups and clusters south of declination”, *Astrophysics and Space Science*, Vol. 28, p. 365, 1974.

108. Ohta, Y. and Kumai, Y. and Watanabe, M. and Furuzawa, A. and Akimoto, F. and Tawara, Y. and Sato, S. and Yamashita, K. and Arai, K. and Shiratori, Y. and Miyoshi, S. and Mazure, A. , “Temperature Map of ABELL 3158”, *New*

Century of X-ray Astronomy, Vol. 251, p. 474, 2001.

109. Tittley, E. R. and Henriksen, M., "A Filament between Galaxy Clusters A3391 and A3395", *Astrophysical Journal*, Vol. 563, p. 673, 2001.

110. Ineson, J., J. H. Croston, M. J. Hardcastle, R. P. Kraft, D. A. Evans and M. J. Jarvis, "The link between accretion mode and environment in radio-loud active galaxies", *Monthly Notices of the Royal Astronomical Society*, Vol. 453, p. 2682, 2015.

111. Lakhchaura, K. and Singh, K. P. and Saikia, D. J. and Hunstead, R. W., "Intra-cluster Medium of the Merging Cluster A3395", *Astrophysical Journal*, Vol. 743, p. 78, 2011.

112. Bîrzan, L., D. A. Rafferty, P. E. J. Nulsen, B. R. McNamara, H. J. A. Röttgering, M. W. Wise and R. Mittal, "The duty cycle of radio-mode feedback in complete samples of clusters", *Monthly Notices of the Royal Astronomical Society*, Vol. 427, pp. 3468–3488, 2012.

113. Lovisari, L. and T. Reiprich, "The Non-Uniformity of Galaxy Cluster Metallicity Profiles", *MRNAS*, Vol. 483, pp. 540–557, 2019.

114. Pimbblet, K. A., S. J. Penny and R. L. Davies, "How typical is the Coma cluster?", *Monthly Notices of the Royal Astronomical Society*, Vol. 438, pp. 3049–3057, 2014.

115. Lin, Y.-T. and J. J. Mohr, "K-band Properties of Galaxy Clusters and Groups: Brightest Cluster Galaxies and Intracluster Light", *Astrophysical Journal*, Vol. 617, pp. 879–895, 12 2004.

116. Schellenberger, G. and T. H. Reiprich, "HICOSMO - Cosmology with a complete sample of galaxy clusters: I. Data analysis, sample selection and luminosity-mass scaling-relation", *Monthly Notices of the Royal Astronomical Society*, Vol. 471, p. 1370, 2017.

117. Bharadwaj, V., T. H. Reiprich, G. Schellenberger, H. J. Eckmiller, R. Mittal and H. Israel, "Intracluster medium cooling, AGN feedback, and brightest cluster galaxy properties of galaxy groups. Five properties where groups differ from clusters", *AA*, Vol. 572, p. A46, 2014.

118. Tombesi, F., R. F. Mushotzky, C. S. Reynolds, T. Kallman, J. N. Reeves, V. Braito, Y. Ueda, M. A. Leutenegger, B. J. Williams, L. Stawarz and M. Cappi, "Feeding and feedback in the powerful radio galaxy 3C 120", *Astrophysical Journal*, Vol. 838, p. 16, 3 2017.

119. Gaspari, M., M. Ruszkowski and P. Sharma, "Cause and Effect of Feedback: Multiphase Gas in Cluster Cores Heated by AGN Jets", *ApJ*, Vol. 746, p. 94, 2012.

120. Hogan, M. T., A. C. Edge, J. Hlavacek-Larrondo, K. J. B. Grainge, S. L. Hamer, E. K. Mahony, H. R. Russell, A. C. Fabian, B. R. McNamara and R. J. Wilman, "A Comprehensive Study of the Radio Properties of Brightest Cluster Galaxies", *Monthly Notices of the Royal Astronomical Society*, Vol. 453, p. 1201, 2015.

121. Persic, M. and Y. Rephaeli, "X-Ray Spectral Components of Starburst Galaxies", *Astronomy and Astrophysics*, Vol. 382, p. 843, 2002.

122. Mineo, S., M. Gilfanov, B. D. Lehmer, G. E. Morrison and R. Sunyaev, "X-ray emission from star-forming galaxies - III. Calibration of the Lx-SFR relation up to redshift z = 1.3", *Monthly Notices of the Royal Astronomical Society*, Vol. 437, pp. 1698–1707, 2014.

123. Westhues, C., M. Haas, P. Barthel, B. J. Wilkes, S. P. Willner, J. Kuraszkiewicz, P. Podigachoski, C. Leipski, K. Meisenheimer, R. Siebenmorgen and R. Chini, "Star formation in 3CR radio galaxies and quasars at z 1", *Astronomical Journal*, Vol. 151, p. 120, 2016.

124. Tombesi, F., J. N. Reeves, T. Kallman, C. S. Reynolds, R. F. Mushotzky,

V. Braito, E. Behar, M. A. Leutenegger and M. Cappi, "The complex circumnuclear environment of the broad-line radio galaxy 3C 390.3 revealed by Chandra HETG", *Astrophysical Journal*, Vol. 830, p. 98, 10 2016.

125. Wagner, A. Y., G. V. Bicknell and M. Umemura, "Driving Outflows with Relativistic Jets and the Dependence of AGN Feedback Efficiency on ISM Inhomogeneity", *Astrophysical Journal*, Vol. 757, p. 136, 2012.

126. Wagner, A. Y., M. Umemura and G. V. Bicknell, "Ultra Fast Outflows: Galaxy-Scale Active Galactic Nucleus Feedback", *Astrophysical Journal Letters*, Vol. 763, p. L18, 2013.

127. Zubovas, K. and S. Nayakshin, "Energy- and momentum-conserving AGN feedback outflows", *Monthly Notices of the Royal Astronomical Society*, Vol. 440, pp. 2625–2635, 2014.

128. Bourne, M. A. and S. Nayakshin, "Inverse Compton X-ray signature of AGN feedback", *Monthly Notices of the Royal Astronomical Society*, Vol. 436, pp. 2346–2351, 2013.

129. Nims, J., E. Quataert and C.-A. Faucher-Giguere, "Observational Signatures of Galactic Winds Powered by Active Galactic Nuclei", *Monthly Notices of the Royal Astronomical Society*, Vol. 447, p. 3612, 2015.

130. Tashiro, M., H. Maejima, K. Toda, R. Kelley, L. Reichenthal, J. Lobell, R. Petre, M. Guainazzi, E. Costantini and M. Edison, "Concept of the X-ray Astronomy Recovery Mission", *Space Telescopes and Instrumentation 2018: Ultraviolet to Gamma Ray*, Vol. 10699 of *Society of Photo-Optical Instrumentation Engineers (SPIE) Conference Series*, p. 1069922, Jul 2018.

131. Gaskin, J. A., A. Dominguez, K. Gelmis, J. . Mulqueen, D. Swartz, K. McCarley, F. Özel, A. Vikhlinin, D. Schwartz, H. Tananbaum, G. Blackwood, J. Arenberg, W. Purcell and L. Allen, "The Lynx X-ray Observatory: concept study overview

and status", *Space Telescopes and Instrumentation 2018: Ultraviolet to Gamma Ray*, 2018.

132. Mushotzky, R., "AXIS: a probe class next generation high angular resolution x-ray imaging satellite", *Space Telescopes and Instrumentation 2018: Ultraviolet to Gamma Ray*, Vol. 10699 of *Society of Photo-Optical Instrumentation Engineers (SPIE) Conference Series*, p. 29, 12 2018.

133. Barcons, X., D. Barret, A. Decourchelle, J. W. den Herder, A. C. Fabian, H. Matsumoto, D. Lumb, K. Nandra, L. Piro and R. K. Smith, "Athena: ESA's X-ray observatory for the late 2020s", *Astronomische Nachrichten*, Vol. 338, No. 153, pp. 153–158, Mar 2017.

APPENDIX A: BACKGROUND MODELING

In this chapter, the fit results of the background models of the cluster sample are presented. The detailed treatment of the background is described in Section 4.2. The figure legends are labeled as follows; total photon of counts are shown with *black*, total background emission is shown with *red*, thermal emission of LHB is shown with *purple*, thermal emission of GTE is shown with *dark blue*, power-law emission from CXB is shown with *blue*, and hard particle background emission is shown with *cyan* curves. The residuals correspond to data and model ratios with 90% significance.

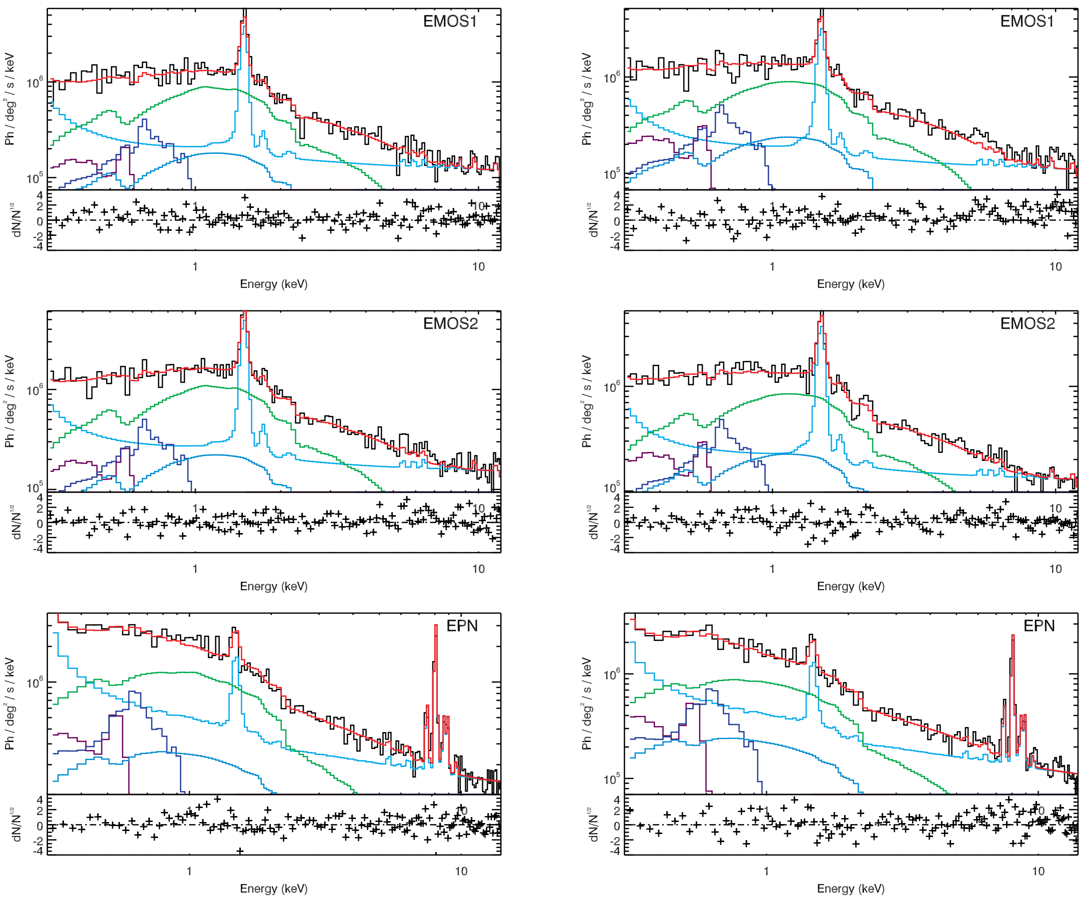

Figure A.1. Background model fitting of Abell 399 (*left*) and Abell 401 (*right*).

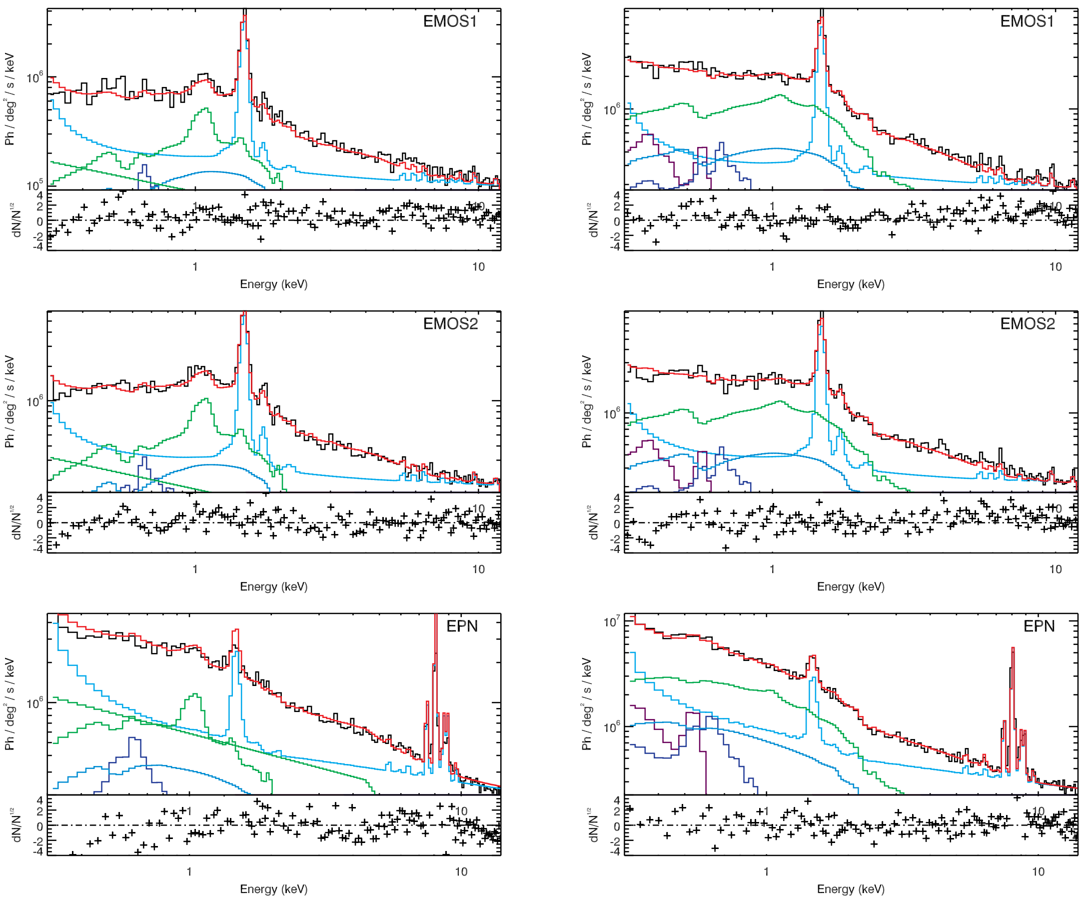

Figure A.2. Background model fitting of Abell 400 (*left*) and Abell 3158 (*right*).

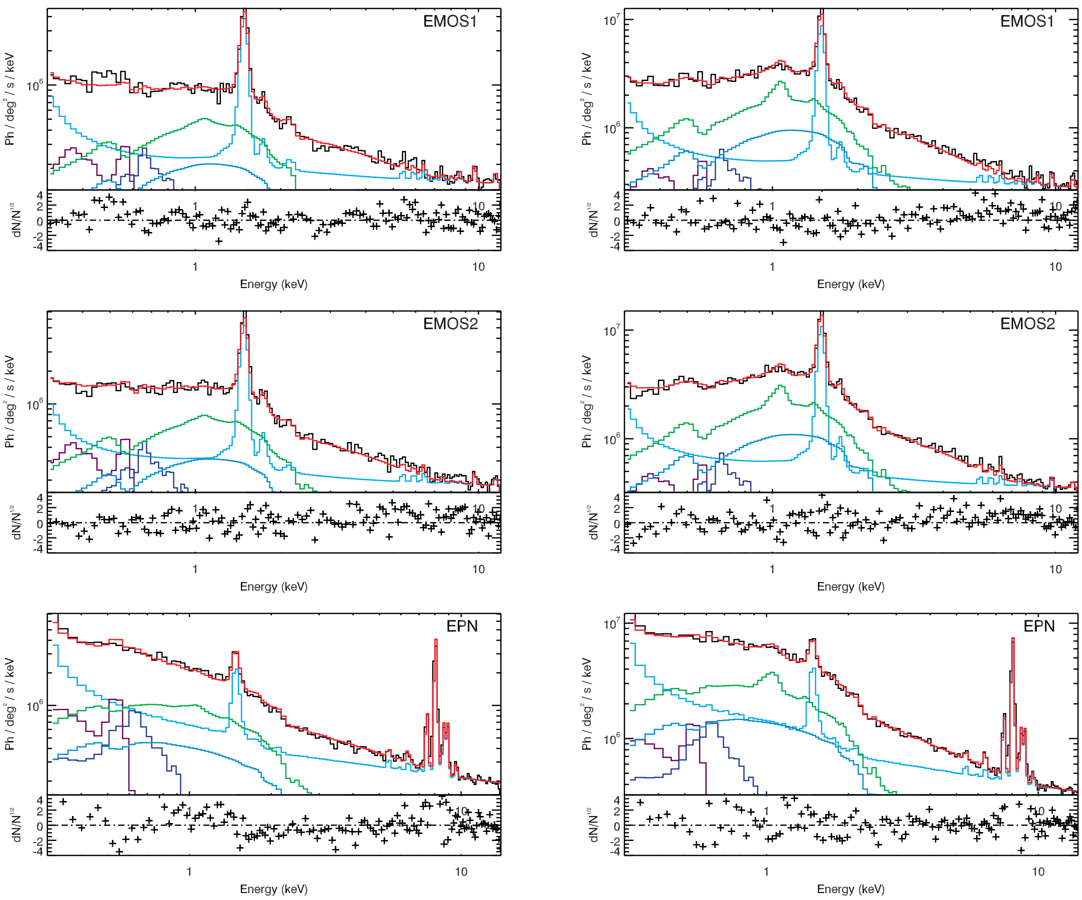

Figure A.3. Background model fitting of Abell 3391 (*left*) and Abell 3395 (*right*).

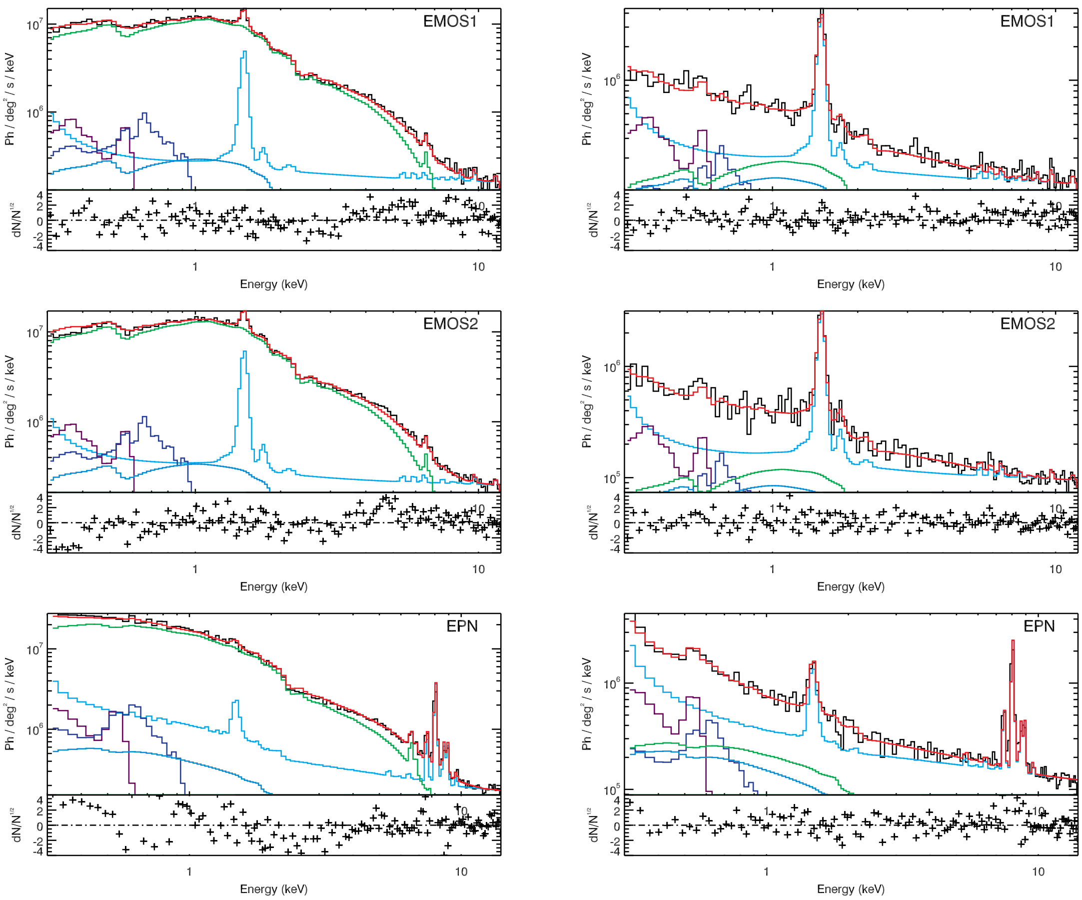

Figure A.4. Background model fitting of Abell 1656 (*left*) and ZwCl 1215 (*right*).

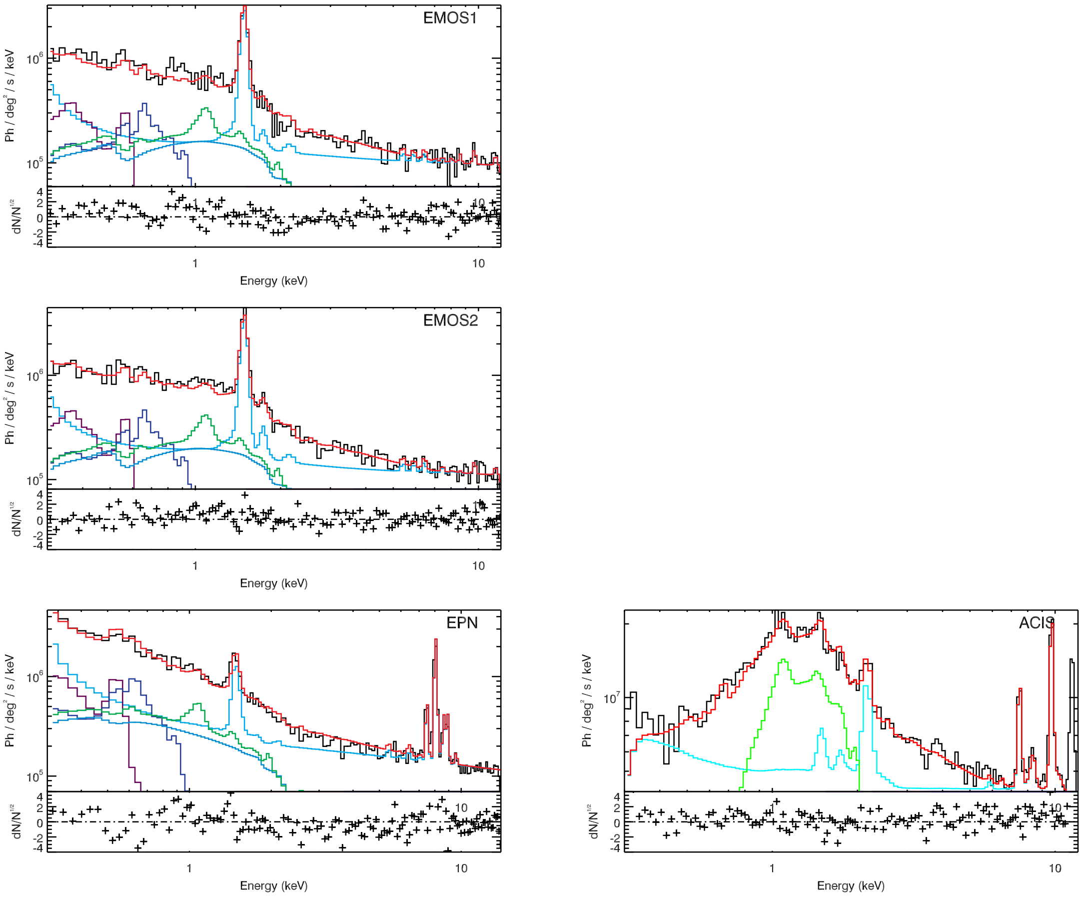

Figure A.5. Background model fitting of MKW 08 for *XMM-Newton* (*left*) and *Chandra* (*right*).